Doctoral Dissertation
博士論文

Diffuse Hydrogen Lyman Alpha Emission Around Star-Forming Galaxies at High Redshift Probed by Optical Imaging and Spectroscopy

(可視光撮像と分光で探る高赤方偏移の
星形成銀河周辺に存在する淡い水素ライマンアルファ輝線)

A Dissertation Submitted for the Degree of Doctor of Philosophy
July 2019
令和元年 7 月博士 (理学) 申請

Department of Physics, Graduate School of Science,
The University of Tokyo
東京大学理学系研究科
物理学専攻

Haibin Zhang
张 海滨

Ph.D. Thesis Committee:

Dr. Tadayuki Takahashi (Kavli Institute for The Physics and Mathematics of The Universe); Chair

–alphabetical order–

Dr. Katsuaki Asano (Institute for Cosmic Ray Research, The University of Tokyo)

Dr. Kentaro Nagamine (Department of Earth and Space Science, Graduate School of Science, Osaka University)

Dr. Toru Yamada (Institute of Space and Astronautical Science, Japan Aerospace eXploration Agency)

Dr. Satoshi Yamamoto (Department of Physics, Graduate School of Science, The University of Tokyo)

Thesis Adviser:

Dr. Masami Ouchi (Institute for Cosmic Ray Research, The University of Tokyo)

ACKNOWLEDGEMENTS

First, I would like to thank my academic advisor, Masami Ouchi, for his great help, encouragement, and education during my phd course in the last three years. He has taught me a lot, including but not limited to how to do research, how to write a observation proposal and paper, and how to give a good presentation. His contribution to my current achievement is undeniable.

Second, I want to thank my thesis committee members including Tadayuki Takahashi, Katsuaki Asano, Kentaro Nagamine, Toru Yamada, and Satoshi Yamamoto for their comments and suggestions on my thesis. I have learned a lot from the communications with them.

Third, I want to thank my parents for their support for my study. Although it is inevitable to feel lonely sometimes when staying in a foreign country as an international student, my parents helped me get over with many mental difficulties. I also thank their understanding of my absence at home for a long time, and their encouragement on my study.

Fourth, I want to thank all the colleagues and friends around me, including but not limited to Yoshiaki Ono, Takatoshi Shibuya, Suraphong Yuma, Jun Toshikawa, Ken Mawatari, Akira Konno, Masafumi Ishigaki, Yuichi Harikane, Seiji Fujimoto, Takashi Kojima, Yuma Sugahara, Shiro Mukae, Ryo Higuchi, Hilmi Miftahul, Ryohei Itoh, Shotaro Kikuchihara, Ryota Kakuma, Karin Shimodate, Yechi Zhang, Nao Sakai, Yuki Isobe, Dongsheng Sun, Fan Yu, and Chenhua Geng. I thank them for their help, support, and communications in the last 3 years.

Last but not least, I appreciate the MEXT of Japan for providing the MEXT scholarship. The financial support helped me a lot as an international student.

The Hyper Suprime-Cam (HSC) collaboration includes the astronomical communities of Japan and Taiwan, and Princeton University. The HSC instrumentation and software were developed by the National Astronomical Observatory of Japan (NAOJ), the Kavli Institute for the Physics and Mathematics of the Universe (Kavli IPMU), the University of Tokyo, the High Energy Accelerator Research Organization (KEK), the Academia Sinica Institute for Astronomy and Astrophysics in Taiwan (ASIAA), and Princeton University. Funding was contributed by the FIRST program from Japanese Cabinet Office, the Ministry of Education, Culture, Sports, Science and Technology (MEXT), the Japan Society for the Promotion of Science (JSPS), Japan

Science and Technology Agency (JST), the Toray Science Foundation, NAOJ, Kavli IPMU, KEK, ASIAA, and Princeton University.

This thesis makes use of software developed for the Large Synoptic Survey Telescope. We thank the LSST Project for making their code available as free software at http://dm.lsst.org

The Pan-STARRS1 Surveys (PS1) have been made possible through contributions of the Institute for Astronomy, the University of Hawaii, the Pan-STARRS Project Office, the Max-Planck Society and its participating institutes, the Max Planck Institute for Astronomy, Heidelberg and the Max Planck Institute for Extraterrestrial Physics, Garching, The Johns Hopkins University, Durham University, the University of Edinburgh, Queen's University Belfast, the Harvard-Smithsonian Center for Astrophysics, the Las Cumbres Observatory Global Telescope Network Incorporated, the National Central University of Taiwan, the Space Telescope Science Institute, the National Aeronautics and Space Administration under Grant No. NNX08AR22G issued through the Planetary Science Division of the NASA Science Mission Directorate, the National Science Foundation under Grant No. AST-1238877, the University of Maryland, and Eotvos Lorand University (ELTE) and the Los Alamos National Laboratory.

Based in part on data collected at the Subaru Telescope and retrieved from the HSC data archive system, which is operated by Subaru Telescope and Astronomy Data Center at National Astronomical Observatory of Japan.

The NB718 and NB816 filters were supported by Ehime University (PI: Y. Taniguchi). The NB921 and NB973 filters were supported by KAKENHI (23244025) Grant-in-Aid for Scientific Research (A) through the Japan Society for the Promotion of Science (PI: M. Ouchi).

Some of the data presented herein were obtained at the W. M. Keck Observatory, which is operated as a scientific partnership among the California Institute of Technology, the University of California and the National Aeronautics and Space Administration. The Observatory was made possible by the generous financial support of the W. M. Keck Foundation.

We wish to recognize and acknowledge the very significant cultural role and reverence that the summit of Maunakea has always had within the indigenous Hawaiian community. We are most fortunate to have the opportunity to conduct observations from this mountain.

This thesis includes data gathered with the 6.5 meter Magellan Telescopes located at Las Campanas Observatory, Chile.

This thesis is supported by World Premier International Research Center Initiative (WPI Initiative), MEXT, Japan, and KAKENHI (15H02064, 17H01110, and 17H01114) Grant-in-Aid for Scientific Research (A) through Japan Society for the Promotion of Science.

ABSTRACT

We study the spatially extended hydrogen Lyα emission around Lyα blobs (LABs), which are star-forming galaxies with bright (Lyα luminosity $L_{\rm Ly\alpha} \gtrsim 10^{43.4}$ erg s^{-1}) and extended Lyα emission, at $z = 4.9 - 7.0$. With the Subaru Hyper Suprime-Cam (HSC), we have carried out a deep and wide-field imaging survey. Using the imaging data obtained from our survey, we have identified two new LABs dubbed z70-1 and z49-1 at $z = 6.965$ and $z = 4.888$, respectively. We present the photometric and spectroscopic properties of a total of seven LABs; the two new LABs and five previously known LABs at $z = 5.7 - 6.6$. The z70-1 LAB shows the extended Lyα emission with a scale length of 1.4 ± 0.2 kpc, about three times larger than the UV continuum emission, making z70-1 the most distant LAB identified to date. All of the 7 LABs, except z49-1, exhibit no AGN signatures such as X-ray emission, N$\textsc{v}\lambda$1240 emission, or Lyα line broadening, while z49-1 has a strong C$\textsc{iv}\lambda$1548 emission line possibly indicating an AGN on the basis of the UV-line ratio diagnostics. In the small scale of 5 kpc on the spectra, our LABs show Lyα velocity and line-width gradients that may be caused by dynamical systems (e.g. mergers) or a surrounding cloud of thick H$\textsc{i}$ gas with varying column densities. We investigate the large-scale structure around our LABs by calculating the LAE overdensity, and show that all of the 7 LABs are located in overdense regions. With SED fitting, we show that the LABs have a variety of specific SFRs suggesting the existence of star-burst and non-star-burst phases in LABs.

We carefully extract the Lyα profiles of our LABs after homogenizing the point-spread functions of the HSC images, and conduct two-component exponential profile fitting to the extended Lyα emission of the LABs. The Lyα scale lengths of the core (star-forming region) and the halo components are $r_{\rm c} = 0.6 - 1.2$ kpc and $r_{\rm h} = 2.0 - 13.8$ kpc, respectively. We show that the relations between the scale lengths and galaxy properties (Lyα luminosity $L_{\rm Ly\alpha}$, Lyα rest-frame equivalent width EW$_0$, and UV continuum magnitude $M_{\rm UV}$) of our LABs are similar to those of Lyα halos (LAHs) identified around star-forming galaxies found previously by VLT/MUSE at the similar redshifts. We find no strong evidence supporting that our LABs and previously known LAHs are distinct populations.

TABLE OF CONTENTS

CHAPTER 1
INTRODUCTION

1.1 Big Bang Cosmology

The formation and evolution of the universe are two of the biggest issues in astrophysics. A widely accepted theory to address these issues is the Big Bang cosmology (e.g. Peebles et al. 1991; Figure 1.1). The Big Bang cosmology suggests a universe starting from the Big Bang. Following the Big Bang, the universe expands rapidly during the inflationary epoch. Neutrons and protons are then formed in the process known as baryogenesis, and neclei such as deuterium and helium are produced during the Big Bang nucleosynthesis. As the universe cools down during the expansion, hydrogen atoms start to form stably by the recombination of protons and electrons when the age of the universe is about 380,000 years. The universe is then filled by neutral hydrogen atoms, and becomes transparent to photons that can be observed nowadays as the cosmic microwave background (CMB) radiation. After the recombination epoch, the universe proceeds to the period known as the Dark Age. At the beginning of the Dark Age, there are no stars and galaxies. The first stars are predicted to form at about 100 million years after the Big Bang, followed by the formation of galaxies when the age of the universe is about several hundred million years (Miralda-Escudé 2003; Oesch et al. 2016). Stars and galaxies radiate ionizing photons that cause photoionization of neutral hydrogen atoms, and the universe becomes less neutral as more ionizing photons are generated. This period is called cosmic reionization. After the reionization is completed (about 1 billion years after the Big Bang; $z \lesssim 6$; Zaroubi 2013), the universe is almost ionized, and such is the state of our current universe.

In detail, the Big Bang cosmology can be parameterized by the widely accepted Lambda Cold Dark Matter (ΛCDM) model. The ΛCDM model assumes that the universe contains major components of dark energy, cold dark matter, and baryonic matter. This model has successfully explained many observational results such as the accelerating expansion of the universe, the CMB, and the large scale structure of the universe. For example, the latest CMB data obtained with the *Planck* satellite are well fitted by the ΛCDM model (Planck Collaboration et al. 2018). The best-fit model suggests that we are living in an almost flat universe whose density consists of $\sim 70\%$ of dark energy and $\sim 30\%$ of dark and baryonic matter (Ostriker & Steinhardt

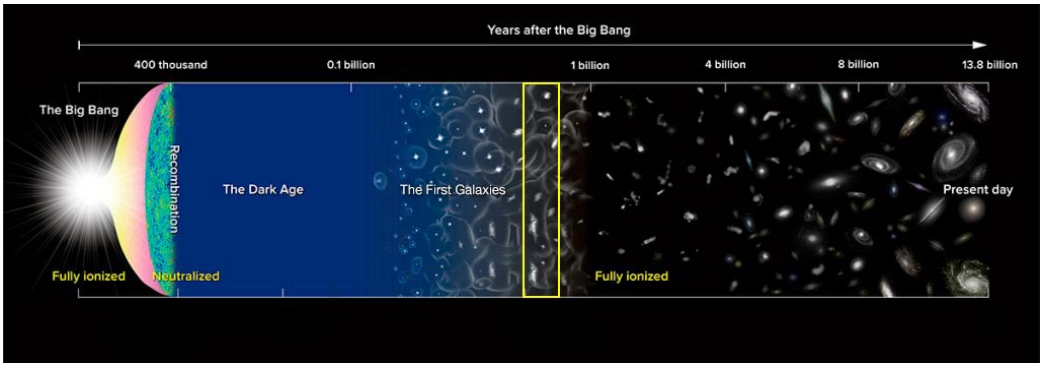

Figure 1.1 Cosmic history of the universe according to the Big Bang cosmology (courtesy: NAOJ/NOAO). The Big Bang, recombination, Dark Age, formation of the first galaxies, and cosmic reionization (yellow box) are indicated as a function of cosmic time.

1995; Bahcall et al. 1999; Freedman et al. 2001; Cole et al. 2005; Astier et al. 2006; Bennett et al. 2013; Planck Collaboration et al. 2018; Figure 1.2). Additionally, the matter power spectrum of the local large scale structure is well explained by the ΛCDM model derived from the CMB, which is another success of the ΛCDM model (e.g. Tegmark et al. 2004; Planck Collaboration et al. 2018).

1.2 Structure Formation

In the widely accepted Big Bang cosmology, although the universe is assumed to be almost homogeneous and isotropic right after the Big Bang, quantum fluctuations exist in the scalar field that causes the inflation. Driven by the exponential expansion of the universe in the inflationary epoch, the quantum fluctuations grow to density fluctuations with an amplitude of $\sim 10^{-5}$ (a.k.a. primordial fluctuations) at the recombination epoch. The primordial fluctuations generate underdensities and overdensities of matter, which cause gravitational instabilities that accelerate the accretion of matter into overdense regions. Following the formation of a self-gravitating system (virialized system) of dark matter, which is called a dark matter halo (Figure 1.3), baryonic matter in the dark matter halo cools down by radiation (radiative cooling) and forms stars and galaxies (Rees, & Ostriker 1977; see details in Section 2.1). It is widely believed that small galaxies form first, and grow to large galaxies via mergers (hierarchical structure formation).

In order to study the evolution of galaxies related to the hierarchical structure

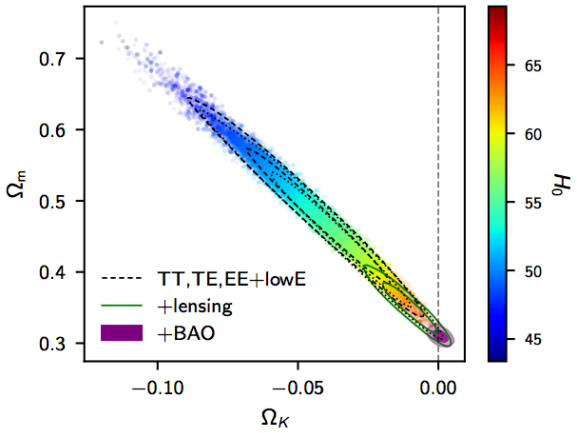

Figure 1.2 Best-fit cosmological parameters from a study of the cosmic microwave background. The Ω_K, $\Omega_{\rm m}$, and H_0 are the curvature density parameter, matter density parameter, and present-day Hubble parameter, respectively. The vertical dashed line indicates a universe that is spatially flat. The TT, TE, EE, and lowE stand for measurements using the temperature power spectrum, temperature-polarization cross-spectrum, polarization power spectrum, and low-multipole power spectrum, respectively. The contours correspond to 68% and 95% confidence levels of measurements from the CMB (black dashed line), CMB combined with lensing (green solid line), and CMB combined with lensing and baryon acoustic oscillations (BAO; purple region). Details of these measurements are presented in Planck Collaboration et al. (2018). The best-fit parameters (purple region) suggest that our universe is almost flat, and that the total density consists of $\sim 70\%$ of dark energy and $\sim 30\%$ of matter. This figure is taken from Planck Collaboration et al. (2018).

formation, a large sample of star-forming galaxies (SFGs) at high-z is needed. Previous studies have developed two main techniques to search for high-z SFGs. The first technique is to select objects with a break at 912 Å that is a typical feature of high-z galaxies, because neutral hydrogen gas in the interglactic medium (IGM) absorbs photons whose wavelength is shorter than the Lyman limit at 912 Å. This break is called a Lyman break, and galaxies with a Lyman break are named as Lyman break galaxies (LBGs; Steidel et al. 1996). The second technique is to select galaxies with Lyα emission. In this thesis, we will only use the second technique whose details are presented in the next section.

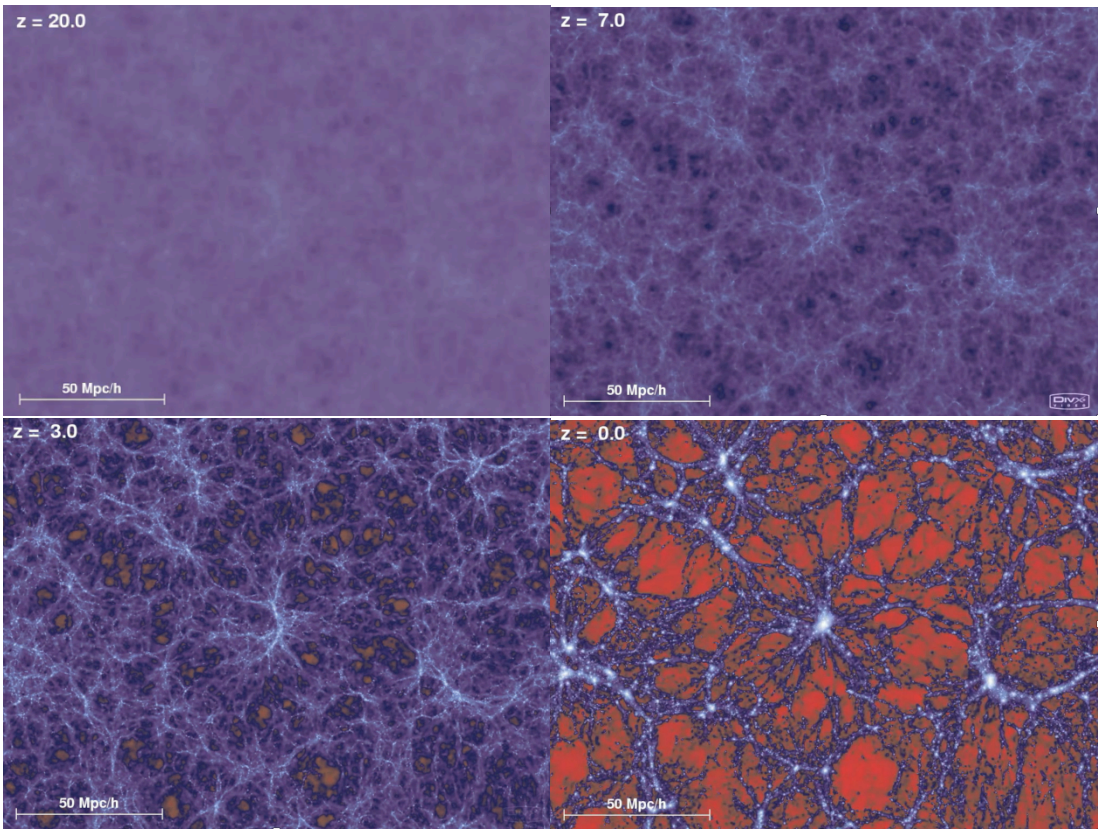

Figure 1.3 Density maps of dark matter at $z = 20$ (the Dark Age; top left), 7 (during reionization; top right), 3 (after reionization; bottom left), and 0 (current universe; bottom right). The dark matter is colored in purple. The brighter color corresponds to a higher density of dark matter. This figure is generated by a cosmological model in Springel (2005).

1.3 Lyα Emitters

As we introduced in the previous section, one probe to study high-z galaxies is the hydrogen Lyα emission whose wavelength is 1215.67 Å, because the redshifted Lyα emission of high-z galaxies enters the wavelength coverage of ground-based optical and near-infrared instruments. The Lyα emission from galaxies can be generated in physical processes including: 1) recombination of hydrogen gas that is ionized by young massive stars and/or active galactic nuclei (AGNs), 2) collisional excitation of hydrogen gas in the inflow and outflow, and 3) fluorescence of hydrogen gas photoionized by ultraviolet (UV) background radiation. Historically, galaxies with Lyα emission are predicted by Partridge & Peebles (1967). In the last two decades, thousands of galaxies with Lyα emission at high-z have been identified (e.g. Ouchi et al. 2003, 2008). These galaxies with Lyα emission are called Lyα emitters (LAEs).

The physical nature of LAEs has been investigated by many previous studies. Analysis of the stellar population of LAEs suggests that typical LAEs are young ($\sim$ 10 Myr) and low-stellar-mass ($\sim 10^{8-9} M_\odot$) SFGs whose star formation rate (SFR) is $\sim 1 - 10 M_\odot$ yr^{-1} (e.g. Ono et al. 2010; Nakajima et al. 2012; Hagen et al. 2014, 2016). Figure 1.4 shows the SFR as a function of stellar mass of LAEs and SFGs. Clearly, at the typical stellar mass ($\sim 10^{8-9} M_\odot$) LAEs have a larger SFR, which suggests a higher specific SFR (SFR per unit stellar mass), than the average value of SFGs. Additionally, the typical gas-phase metallicity of LAEs is $\sim 0.1 - 0.5 Z_\odot$. This value is similar to or slightly smaller than those of typical SFGs (e.g. LBGs) with the same UV luminosity (Nakajima et al. 2012; Steidel et al. 2014). The stellar age, stellar mass, SFR, and metallicity of LAEs suggest that LAEs are good targets to study the early phase of galaxy formation and evolution.

In addition to the previous analysis of stellar population related to the physical nature, morphological studies have revealed the size evolution of LAEs. It is shown that typical LAEs with a fixed UV luminosity grow larger at lower redshifts (e.g. Shibuya et al. 2019; Figure 1.5), which is expected in the picture of hierarchical structure formation. As most LAEs are small at high-z, massive LAEs are found to be very rare with a number density of $\sim 10^{-7} - 10^{-6}$ Mpc^{-3} at $z = 6 - 7$ (Shibuya et al. 2018; Figure 1.6). Because these rare and massive LAEs are possibly among the first galaxies according to the hierarchical structure formation, they are important objects to study the formation and evolution of young massive SFGs in the early

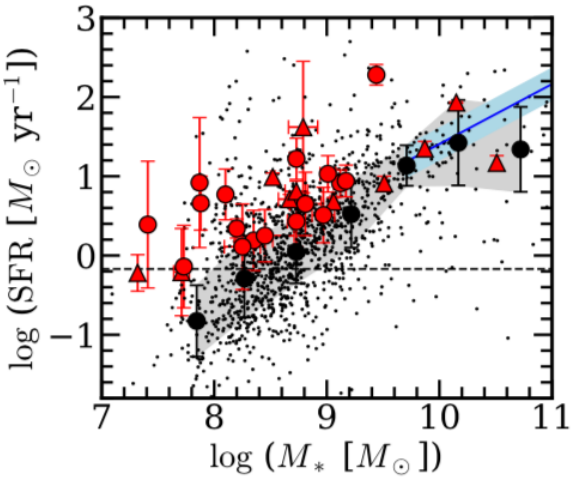

Figure 1.4 SFR as a function of stellar mass of LAEs (red filled triangles and circles) at $z \sim 2$ and SFGs (black dots) at similar redshifts. The red triangles and circles are LAEs identified with narrowband surveys and the Hobby-Eberly Telescope Dark Energy Experiment (HETDEX) Pilot Survey, respectively (Hagen et al. 2016). The SFGs are selected by Santini et al. (2017). The large black filled circles are the average values of SFGs with errors indicated as the grey shaded region. The blue solid line and blue shaded region correspond to average values and errors, respectively, of massive SFGs at similar redshifts from Speagle et al. (2014). This figure is taken from Ouchi et al. (2020, in preparation for the Annual Review of Astronomy and Astrophysics).

universe. We introduce details of these massive LAEs in the next section.

1.4 Lyα Blobs

In this section, we introduce previous studies and unresolved issues related to massive LAEs.

In order to study the formation and evolution of young massive SFGs in the early universe, previous observations have identified some high-z LAEs with very luminous Lyα emission ($\log(L_{\rm Ly\alpha}/[{\rm erg\ s^{-1}}]) \gtrsim 43.4$) and large sizes (e.g. isophotal area $A_{\rm iso} \gtrsim 150$ kpc^2 at $z = 6.6$) compared to those of typical LAEs (e.g. $\log(L_{\rm Ly\alpha}/[{\rm erg\ s^{-1}}]) \sim 42 - 43$ and $A_{\rm iso} \sim 15 - 60$ kpc^2 at $z = 6.6$; Ouchi et al. 2009). The sizes of the Lyα emission of these massive LAEs are larger than the UV continuum counterparts, and such Lyα emission is defined to be spatially extended in this thesis. These luminous and spatially extended LAEs are often referred to as Lyα blobs (LABs; e.g. Keel et al. 1999; Steidel et al. 2000; Francis et al. 2001; Matsuda et al. 2004; Ouchi et al.

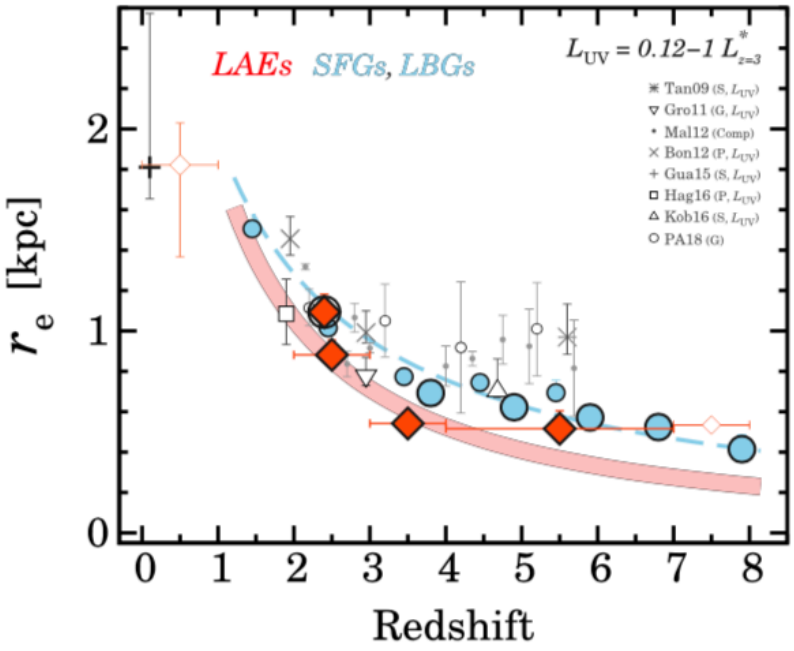

Figure 1.5 Galaxy size as a function of redshift of LAEs (red filled diamonds), LBGs (large cyan filled circles), and SFGs (small cyan filled circles) at $z \simeq 0-8$. The red open diamond at $z \simeq 0.5$ represents LAEs at $z \simeq 0-1$. The red open diamond at $z \simeq 7.5$ corresponds to LAEs at $z \simeq 7-8$ whose error bars are not reliable due to the small sample size. The red shaded region and blue dashed line are the best-fit power-law functions for LAEs and SFGs/LBGs, respectively. The gray symbols are measurements from previous studies (asterisks: Taniguchi et al. 2009; inverted triangles: Gronwall et al. 2011; crosses: Bond et al. 2012; dots: Malhotra et al. 2012; plus signs: Guaita et al. 2015; squares: Hagen et al. 2016; triangles: Kobayashi et al. 2016; circles: Paulino-Afonso et al. 2018). This figure is taken from Shibuya et al. (2019).

2009; Sobral et al. 2015; Shibuya et al. 2018). Most LABs are identified at $z \sim 2-3$ and $z \sim 6$. One well-known example of LABs is LAB1 (Steidel et al. 2000) at $z = 3.1$, while the most distant ones are Himiko (Ouchi et al. 2009) and CR7 (Sobral et al. 2015) at $z = 6.6$. Because no LAB has been found at $z \sim 4-5$ and $z \gtrsim 7$, new deep wide-field surveys targeting these redshifts are critical to identify new LABs and study the evolution of LABs continuously from $z \sim 2$ to 7 (unresolved issue 1).

As expected from the hierarchical structure formation, many LABs such as LAB1 are identified in overdense regions, and previous studies have suggested that LABs at $z \sim 2-4$ are associated with large-scale structures (Francis et al. 1996; Steidel et

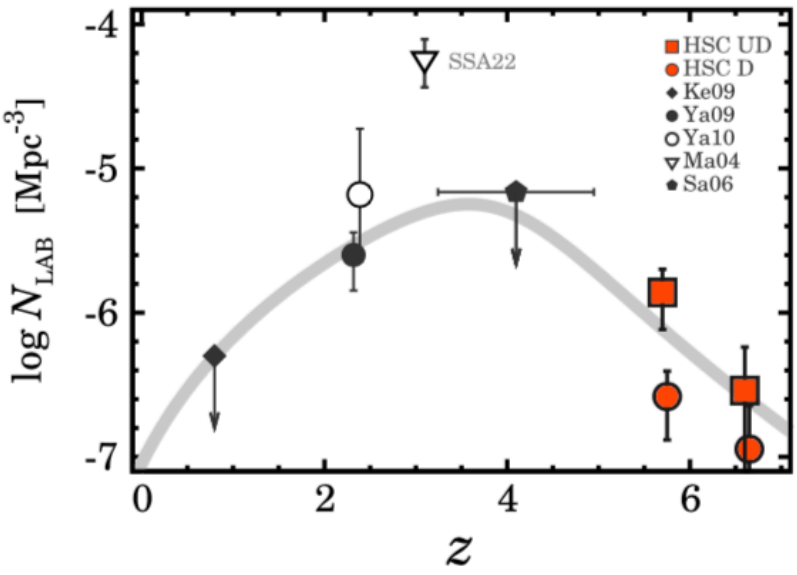

Figure 1.6 Number density as a function of redshift of massive LAEs (Lyα blobs; LABs). The red squares and circles are LABs selected in HSC ultra-deep and deep fields, respectively. The black diamond, filled circle, open circle, triangle, and pentagon present measurements from Keel et al. (2009), Yang et al. (2009), Yang et al. (2010), Matsuda et al. (2004), and Saito et al. (2006), respectively. This figure is taken from Shibuya et al. (2018).

al. 2000; Matsuda et al. 2004; Palunas et al. 2004; Saito et al. 2006; Prescott et al. 2008; Matsuda et al. 2009; Yang et al. 2009; Matsuda et al. 2011; Erb et al. 2011; Kikuta et al. 2019). For example, six LABs are found to be located in an overdense region of galaxies at $z = 2.3$ (Erb et al. 2011). Five of the six LABs are closely associated with the filamentary structure revealed by galaxies at the same redshift, suggesting a connection between LABs and the large scale structure. Similarly, 76 LABs at $z = 2.84$ also show a distribution basically along the large-scale structure traced by galaxy overdensities (Kikuta et al. 2019; Figure 1.7). Indeed, the connection between LABs and the environment is consistent with theoretical studies suggesting that extended Lyα emission traces the gas structure in the circumgalactic medium (CGM) around galaxies (e.g. Furlanetto et al. 2005; Goerdt et al. 2010; Zheng et al. 2011; Lake et al. 2015). Although the large-scale structures around LABs at $z \sim 2-4$ have been investigated statistically as we mentioned above, there is still no statistical study of the environment around LABs at $z > 4$, which is key for understanding the evolution of LABs and the environmental effects at high-z (unresolved issue 2).

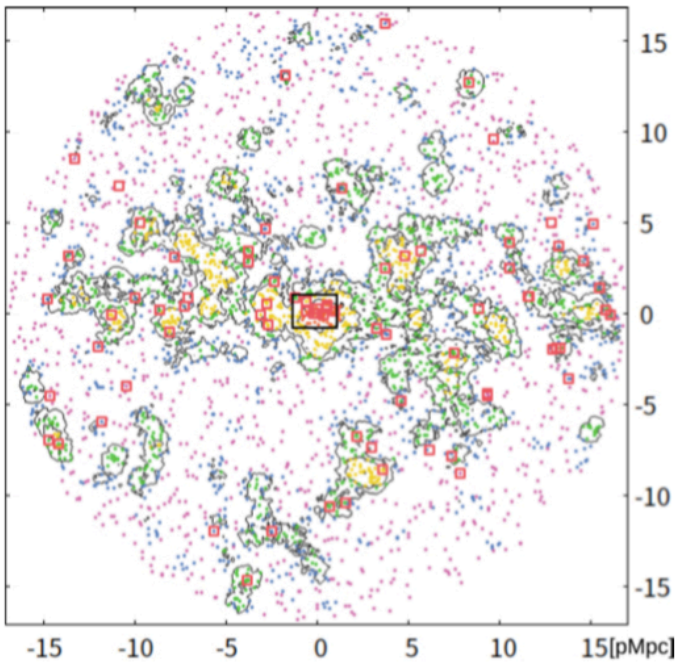

Figure 1.7 Spatial distribution of LABs (red squares) at $z = 2.84$. The dots are LAEs at the same redshift, while the colors indicate the local overdensities (from high to low: red, yellow, green, blue, and magenta; see details in Kikuta et al. 2019). The contours, which trace the large-scale structure, correspond to LAE overdensities of 0.3, 1, and 2.5. The definition of the overdensity is the same as the one in Section 6.2. This figure is taken from Kikuta et al. (2019).

The connection between LABs and large-scale structures suggests not only environmental effects on LABs, but also that LABs may affect their environment via feedback processes such as active galactic nuclei (AGNs). Indeed, LABs are possible hosts of AGNs. This is because most LABs exceed a Lyα luminosity limit of $\log(L_{\mathrm{Ly}\alpha}/[\mathrm{erg\ s^{-1}}]) \gtrsim 43.4$, and AGNs are found to exist in galaxies brighter than this luminosity limit at $z \sim 2-3$ (Konno et al. 2016; Sobral et al. 2018). Previously, AGNs have been identified in some LABs (e.g. LAB2 in Steidel et al. 2000; Basu-Zych & Scharf 2004), while no evidence of AGNs is found in the other LABs (e.g. LAB1; Geach et al. 2007; Matsuda et al. 2007; Prescott et al. 2009). Statistically, Geach et al. (2009) investigate 29 LABs at $z = 3.09$ and find that $\sim 10-30\%$ of the LABs contain AGNs. To explain these observational results, there are two possibilities. One possibility is that all LABs intrinsically have AGNs, and that some AGNs are obscured or too faint to be identified. Another possibility is that there exist two

kinds of LABs with and without AGNs.

For both of AGN and non-AGN LABs, some of them show other emission in addition to the Lyα line. For example, AGN LABs are detected in X-ray and/or CIVλ1550 revealing the strong ionization power of AGNs (e.g. Basu-Zych & Scharf 2004; Yang et al. 2009; Figure 1.8). On the other hand, some LABs with no evidence of AGNs show [OIII], HeIIλ1640, and/or hydrogen Hα emission lines possibly caused by active star formation (e.g. Yang et al. 2011; McLinden et al. 2013; Sobral et al. 2015). These emission lines reveal multiple embedded galaxies in some LABs. The large velocity dispersion between these embedded galaxies supports that LABs may reside in massive dark matter halos that are progenitors of typical rich clusters in the present universe (Yang et al. 2011).

Although there are many observational studies on LABs as we discussed above, the physical origin of the extended Lyα emission of LABs is still unclear. Previous studies have suggested several possible origins for AGN and non-AGN LABs. For example, fluorescence powered by AGNs can possibly explain the luminous and extended Lyα emission of LABs containing AGNs (e.g. Geach et al. 2009). As for LABs with no evidence of AGNs, the Lyα emission may be caused by resonant scattering, gravitational cooling radiation, outflows, and/or satellite galaxies. Details of these scenarios are listed below.

1. Fluorescence. There exists some neutral hydrogen gas in the CGM around a galaxy that is heated by an AGN or star formation. The neutral hydrogen gas is photoionized by the ionizing photons from the galaxy center or UV background. Lyα photons are then emitted during the recombination process (e.g. Mas-Ribas & Dijkstra 2016).

2. Resonant scattering. Lyα photons escape to the CGM from a galaxy center, and are resonantly scattered by the neutral hydrogen in the CGM. Different from the fluorescence, during the resonant scattering the hydrogen gas is excited but not photoionized, and a source of strong ionizing radiation (e.g. an AGN) is not required in this scenario. This process causes the galaxy having Lyα emission more extended than the UV continuum (e.g. Lake et al. 2015; Mas-Ribas et al. 2017). The detailed mechanism of resonant scattering is presented in Section 2.2.

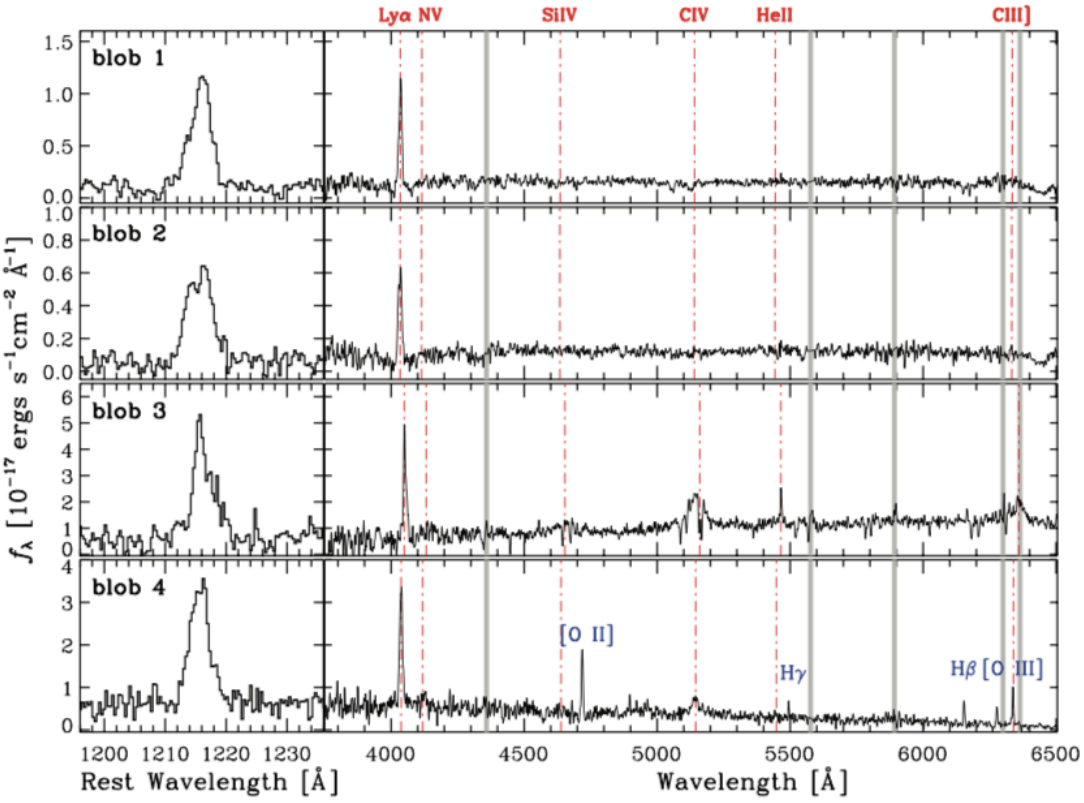

Figure 1.8 Spectra of four LABs at z =2.3. Two (blob 3 and blob 4) of the four LABs have strong CIV emission lines suggestive of AGNs, while the other two LABs (blob 1 and blob 2) do not show any evidences of AGNs. This figure is taken from Yang et al. (2009).

3. Gravitational cooling radiation. Some inflow streams exist around a galaxy, and accrete onto the galaxy center. Lyα photons are emitted by collisional excitation of neutral hydrogen in the streams. In this radiation process, the streams release their gravitational potential energy (e.g. Loeb, & Rybicki 1999; Haiman et al. 2000; Fardal et al. 2001; Dekel et al. 2009; Rosdahl, & Blaizot 2012).

4. Outflows. Multiple supernova explosions in a galaxy produce hot gas outflows. The outflows drive shocked cooling shells that emit Lyα photons (e.g. Taniguchi & Shioya 2000; Taniguchi et al. 2001; Ohyama et al. 2003; Mori et al. 2004; Orsi et al. 2012; Sadoun et al. 2019; Smith et al. 2019). In this scenario, a dusty sub-millimeter source is expected to be located at the galaxy center (Cen, & Zheng 2013).

5. Satellite galaxies. A central galaxy is surrounded by multiple satellite galaxies that emit Lyα photons during star formation. In this scenario, a galaxy may exhibit both extended Lyα emission and extended UV continuum (e.g. Mas-Ribas et al. 2017).

Because the different possible scenarios are expected to cause different shapes of Lyα surface brightness profiles (e.g. Lake et al. 2015; Mas-Ribas & Dijkstra 2016; Mas-Ribas et al. 2017), comparing Lyα surface brightness profiles from observations with those from models may be critical for pinpointing the physical origin. However, no previous study has performed detailed analysis on Lyα surface brightness profiles of LABs at $z > 4$ (unresolved issue 3). For example, although Ouchi et al. (2009) have identified a LAB at $z = 6.6$ and measured the Lyα surface brightness profile, no quantitative profile analysis including profile fitting has been carried out for this LAB (Figure 1.9).

1.5 Lyα Halos

Following the identification of LABs, diffuse Lyα nebulae called Lyα halos (LAHs) are found ubiquitously around typical LAEs with $\log(L_{\mathrm{Ly}\alpha}/[\mathrm{erg\ s^{-1}}]) \sim 42 - 43$ at $z \sim 3 - 6$, and have been identified individually (e.g. Erb et al. 2018; Rauch et al. 2008; Wisotzki et al. 2016; Leclercq et al. 2017; Figure 1.10) or statistically by

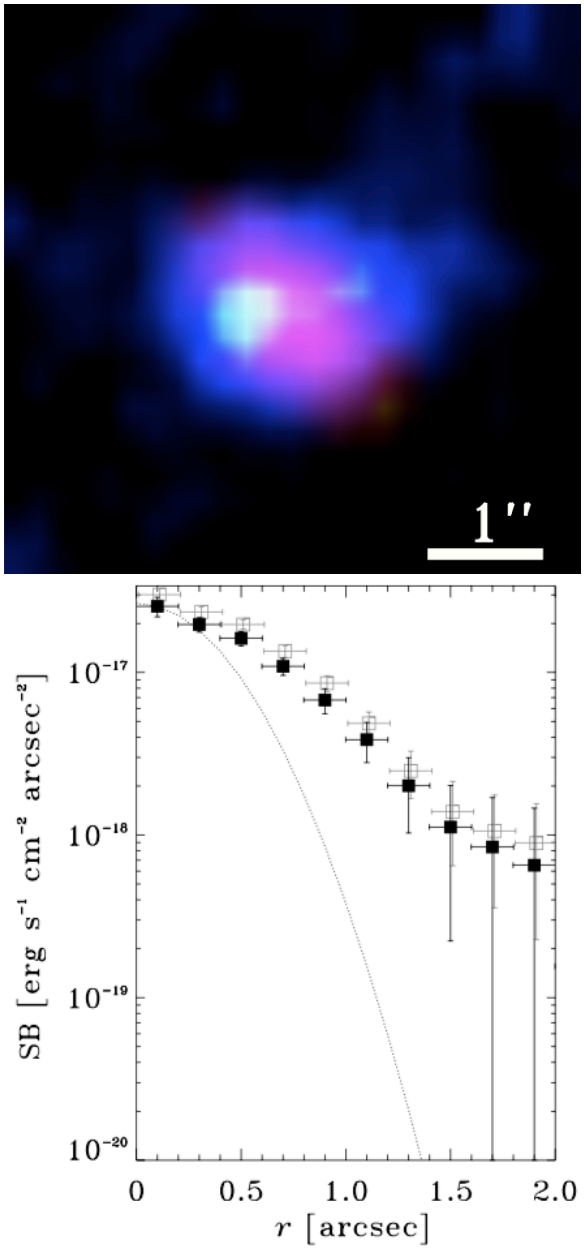

Figure 1.9 Top: Composite pseudocolor image of a LAB at $z = 6.6$ (Himiko; Ouchi et al. 2009). The blue, green, and red colors correspond to the Lyα, UV continuum, and infrared continuum, respectively. Bottom: Lyα surface brightness profile of Himiko. The open squares show the narrowband profile, while the filled squares are the Lyα (continuum subtracted) profile. Although Ouchi et al. (2009) show that the Lyα profile is more extended than point sources (dotted line), no quantitative profile analysis including profile fitting has been carried out for this object. This figure is taken from Ouchi et al. (2009).

stacking analysis (e.g. Hayashino et al. 2004; Steidel et al. 2011; Matsuda et al. 2012; Feldmeier et al. 2013; Momose et al. 2014, 2016; Wisotzki et al. 2018; Figure 1.11). Because both of LAHs and LABs show spatially extended Lyα emission, it is not clear if LAHs and LABs are distinct populations. Additionally, there are no widely adopted criteria used to distinguish LAHs from LABs clearly. It should be noted that the different names of LAHs and LABs are motivated by their observational properties but not physical properties. Historically, LAHs are fainter than LABs, and the typical isophotal area of LAHs is smaller than that of LABs at the similar redshift (cf. Leclercq et al. 2017 and Matsuda et al. 2004 at $z \sim 3$). However, the isophotal area measurement can be largely affected by both of the detection limits and the surface brightness of LAHs and LABs. At the same detection limit, faint LAHs show smaller isophotal areas than bright LABs if the radial profile shapes are the same, since the Lyα luminosities of LAHs are fainter than those of LABs by an order of magnitude. It is not fair to directly compare the isophotal areas of LAHs to those of LABs. One fair comparison is to quantitatively measure the shape of the Lyα surface brightness profile by profile fitting, because in the fitting the difference of surface brightness between LAHs and LABs can be eliminated by a normalization factor. Indeed, with profile fitting it is shown that the shape of the Lyα profile of LAHs is similar to that of LABs at the similar redshift of $z \sim 3$ (Steidel et al. 2011). It is possible that LAHs and LABs have the same physical origin of the extended Lyα emission. However, Lyα surface brightness profiles of LABs at $z > 4$ have not been investigated as we mentioned in the previous section, and the connection between LAHs and LABs at $z > 4$ is still unknown (unresolved issue 4).

1.6 Plan of This Thesis

In the previous sections, we have introduced two motivations of this thesis: 1) studying the formation and evolution of young massive SFGs in the early universe with LABs, and 2) investigating statistically the connection between LABs and LAHs in terms of the similarity of extended Lyα emission. We have pointed out 4 unresolved issues related to our motivations:

1. No LAB has been identified at $z \sim 4 - 5$ and $z \gtrsim 7$ (motivations 1 and 2).

2. No statistical study of the environment around LABs is available at $z > 4$

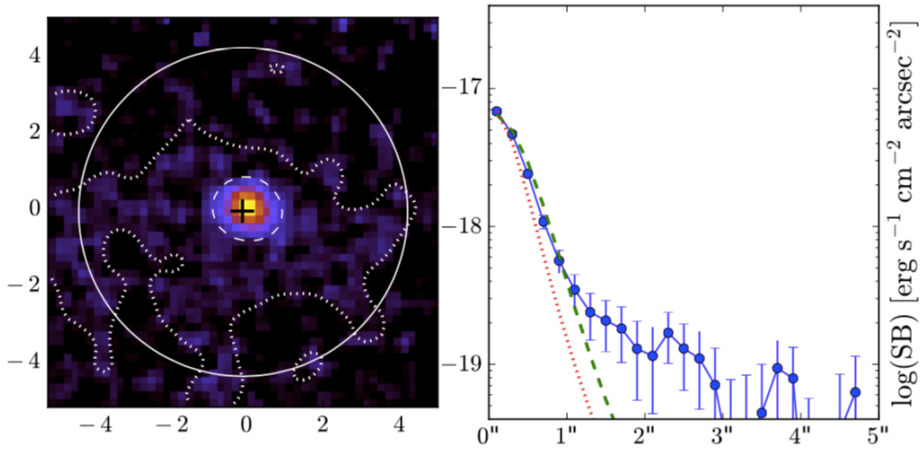

Figure 1.10 Left: Lyα image of a LAH at $z = 5.98$ (MUSE#547). The dashed and dotted white lines correspond to surface brightnesses of 10^{-18} and 10^{-19} erg s^{-1} cm^{-2} arcsec^{-2}, respectively. Right: Surface brightness profiles of the Lyα (blue) emission, UV continuum (green), and point spread function (red). This figure is taken from Leclercq et al. (2017).

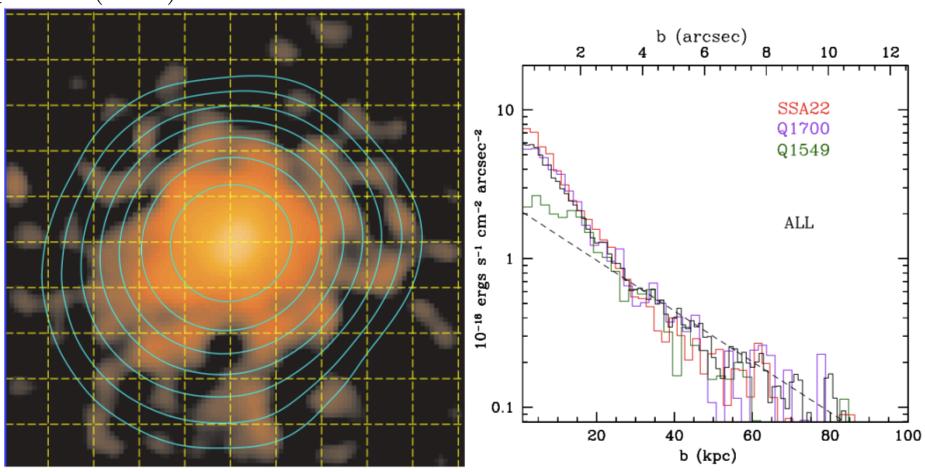

Figure 1.11 Left: Stacked Lyα image of LAEs at $z = 2.65$. The lowest contour corresponds to a surface brightness of $\sim 2.5 \times 10^{-19}$ erg s^{-1} cm^{-2} arcsec^{-2}. Right: Surface brightness profile of the Lyα emission (black). The red, blue, and green lines are stacked Lyα profiles in separate fields of SSA22, Q1700, and Q1549, respectively. This figure is taken from Steidel et al. (2011).

(motivation 1).

3. No previous study has quantitatively analyzed the Lyα surface brightness profiles of LABs at $z > 4$ to understand physical origins of LABs (motivation 1).

4. The connection between LABs and LAHs at $z > 4$ is unknown (motivation 2).

This thesis aims at resolving the 4 issues following the 4 approaches listed below.

1. Identifying new LABs at $z \sim 4 - 5$ and $z \gtrsim 7$ with new deep and wide-field imaging data. We will perform follow-up spectroscopic observations to confirm the redshifts of our LABs.

2. Studying statistically the relation between LABs and their surrounding large-scale structures at $z > 4$ including our new LABs and previously known LABs in the literature.

3. Quantitatively analyzing the Lyα surface brightness profiles of LABs at $z > 4$ with profile fitting, and comparing our observational results with theoretical models.

4. Comparing the Lyα profile fitting results of LABs with those of LAHs in the literature, and investigating the connection between LABs and LAHs statistically.

This thesis is organized as follows. The theoretical background is presented in Chapter 2. We introduce the imaging instruments, observations, and data reductions in Chapter 3. Based on the imaging data, we have selected 2 LAB candidates as shown in Chapter 4. The follow-up spectroscopic observations and data reductions of LABs are given in Chapter 5. We perform detailed analysis and show the results in Chapter 6. Discussions based on the results are presented in Chapter 7. Finally, we summarize our results and conclude this thesis in Chapter 8. Supplementary tables and figures are shown in Chapter 9, the Appendix.

Throughout this thesis, we use AB magnitudes (Oke & Gunn 1983) and physical distances unless we indicate otherwise. A ΛCDM cosmology with $\Omega_m = 0.3$, $\Omega_\Lambda = 0.7$, and $h = 70$ is adopted. Details of the cosmological quantities are shown in Section 2.5.

CHAPTER 2
THEORETICAL BACKGROUNDS

2.1 Galaxy Formation

In this section, we introduce the gravitational collapse and cooling radiation of gas that are key for understanding galaxy formation. The cooling radiation of hydrogen gas possibly contributes to the extended Lyα emission of LABs as we introduced in Section 1.4.

2.1.1 Gravitational Collapse

As we briefly described in Section 1.2, primordial fluctuations cause underdensities and overdensites of matter, and grow by gravitational instabilities. Because many galaxies and galaxy clusters in the local universe have high densities that cannot be explained by a linear growth of density fluctuations, models of nonlinear growth are needed. One simple nonlinear model is the spherical collapse model that describes the gravitational collapse of matter in a spherically symmetric sphere. The following solution is given by Gunn & Gott (1972) and Peacock (1999). Let us assume a matter-dominated universe (the Einstein–de Sitter universe) for simplicity. The radius $r(t)$ of the sphere at a time t is given by

$$\frac{d^2r}{dt^2} = -\frac{GM}{r^2}, \tag{2.1}$$

where G is the gravitational constant and M is the mass within the sphere.

The solution is

$$r = A(1 - \cos\theta) \tag{2.2}$$

$$t = B(\theta - \sin\theta), \tag{2.3}$$

where A and B are 2 constants that follow $A^3 = GMB^2$, and θ is a variable. If we expand this solution up to the order of θ^5, the $r(t)$ for small t becomes

$$r \simeq \frac{A}{2}\left(\frac{6t}{B}\right)^{2/3}\left[1 - \frac{1}{20}\left(\frac{6t}{B}\right)^{2/3}\right]. \tag{2.4}$$

Let us define the density fluctuation δ as

$$\delta = \frac{\rho}{\bar{\rho}} - 1, \tag{2.5}$$

where the local density ρ and cosmic mean density $\bar{\rho}$ are given by

$$\rho = \frac{3M}{4\pi r^3} \tag{2.6}$$

and

$$\bar{\rho} = \frac{1}{6\pi G t^2}, \tag{2.7}$$

respectively. The δ within the sphere is then

$$\delta \simeq \frac{3}{20}\left(\frac{6t}{B}\right)^{2/3}. \tag{2.8}$$

In this model, the sphere expands and the density fluctuation grows as a function of $t^{2/3}$ at a small t. The sphere then reaches the maximum radius $r_{\rm ta} = 2A$ at $t_{\rm ta} = \pi B$ ($\theta_{\rm ta} = \pi$), turns around, and begins to contract. At this point, the density fluctuation $\delta_{\rm ta}$ within the sphere is $9\pi^2/16 - 1 = 4.55$. By comparison, if the growth of the density fluctuation is always linear as a function of $t^{2/3}$, the $\delta_{\rm lin}$ is $(3/20)(6\pi)^{2/3} \simeq 1.06$ at $t_{\rm ta} = \pi B$. The difference between $\delta_{\rm ta}$ and $\delta_{\rm lin}$ shows that the growth of the density fluctuation in this model is nonlinear when t is not small.

The sphere will fully collapse at $t_{\rm col} = 2\pi B$ ($\theta_{\rm col} = 2\pi$). The $\delta_{\rm lin}$ at this time is $(3/20)(12\pi)^{2/3} \simeq 1.69$. The free fall time $t_{\rm ff}$ is defined as

$$t_{\rm ff} = t_{\rm col} - t_{\rm ta} = \pi B = \sqrt{\frac{3\pi}{32 G \rho_{\rm ta}}}, \tag{2.9}$$

where $\rho_{\rm ta} = \frac{3M}{4\pi r_{\rm ta}^3}$ is the local density at $t_{\rm ta} = \pi B$.

However, in reality the sphere will not fully collapse to a singularity. Instead the sphere will contract to a virialized system, which is a system in virial equilibrium. According to the virial theorem, the potential energy $V_{\rm vir}$ and kinetic energy $K_{\rm vir}$ of a virialized system follow the relation $V_{\rm vir} = -2K_{\rm vir}$. The radius of a virialized system

is called the virial radius $R_{\rm vir}$ following

$$V_{\rm vir} = -\frac{3}{5}\frac{GM^2}{R_{\rm vir}}. \tag{2.10}$$

In the spherical collapse model, the total energy E at $t_{\rm ta} = \pi B$ when $K_{\rm ta} = 0$ is equal to the potential energy,

$$E = V_{\rm ta} + K_{\rm ta} = V_{\rm ta} = -\frac{3}{5}\frac{GM^2}{r_{\rm ta}}. \tag{2.11}$$

With Equations 2.10, 2.11, and $E = V_{\rm vir}/2$ derived from the virial theorem, we get $R_{\rm vir} = r_{\rm ta}/2$. If we assume that the sphere becomes virialized at $t_{\rm col} = 2\pi B$, the density fluctuation $\delta_{\rm vir}$ is given by

$$\delta_{\rm vir} = \frac{\rho(R_{\rm vir})}{\bar{\rho}(t_{\rm col})} - 1 = \frac{9}{2}\frac{MGt_{\rm col}^2}{R_{\rm vir}^3} - 1 = 18\pi^2 - 1 \simeq 177. \tag{2.12}$$

In practice, a value of $\delta = 200$ is often used to define the virial radius of a dark matter halo.

2.1.2 Radiative Cooling

In the spherical collapse model, we see how a virialized system of matter is formed. Following the formation of a virialized system of dark matter, a dark matter halo, the baryonic gas in the dark matter halo may continue the contraction. However, if the contraction of the baryonic gas is adiabatic, the temperature will increase and the contraction will stop due to the thermal pressure. To produce the cold baryonic gas needed for star formation, the gas can be cooled down by losing kinetic energy via collisional excitation and radiation, which is a process called radiative cooling. The cooling rate $\dot{E}_{\rm cool}$, the loss of energy per unit volume per unit time, is defined by

$$\dot{E}_{\rm cool} = n^2\Lambda(T), \tag{2.13}$$

where n is the number density of gas particles, $\Lambda(T)$ is the cooling function, and T is the gas temperature. The $\Lambda(T)$ has been calculated based on quantum mechanics and shown in Figure 2.1 (Sutherland, & Dopita 1993). For a higher metallicity, $\Lambda(T)$ becomes larger at a given T, because the various electron transitions of heavy

elements increase the efficiency of radiative cooling. In gas with zero metallicity, hydrogen and helium atoms are the major contributors to the peaks at $T \sim 10^4$ and 10^5 K, respectively. Hydrogen Lyα photons, which are of our interest in this thesis, are emitted by the radiative cooling of hydrogen gas at $T \sim 10^4$ K. The incline at $T \sim 10^6 - 10^8$ K is caused by Bremsstrahlung radiation and Compton scattering.

Before cooling, the kinetic energy K of the gas is

$$K = \frac{3}{2} n k_{\rm B} T, \tag{2.14}$$

where $k_{\rm B}$ is the Boltzmann constant. The cooling time $t_{\rm cool}$ is then given by

$$t_{\rm cool} = \frac{K}{|\dot{K}|} = \frac{3}{2} \frac{k_{\rm B} T}{n \Lambda(T)}, \tag{2.15}$$

where $\dot{K}$ is the time-derivative of K and equals to $\dot{E}_{\rm cool}$.

The radiative cooling is efficient when $t_{\rm cool} < t_{\rm ff}$ as indicated in Figure 2.1. Figure 2.1 also shows that galaxies with a gas mass larger than $10^{11} M_\odot$ ($10^{12} M_\odot$) cannot cool efficiently when the gas has zero (solar) metallicity.

2.2 Lyα Resonant Scattering

In this section, we introduce the mechanism of Lyα resonant scattering that is a possible physical origin of extended Lyα emission of LABs.

Lyα photons with a wavelength $\lambda = 1215.67$ Å can be resonantly scattered by hydrogen atoms at the ground state (neutral hydrogen; HI). The physical process of Lyα resonant scattering is explained below.

The energy of a Lyα photon equals to the difference between the $n = 1$ and $n = 2$ energy levels of a hydrogen atom, where n is the principal quantum number. When a hydrogen atom at the ground state ($n = 1$) absorbs a Lyα photon, the atom is excited to the $n = 2$ state. When the excited hydrogen atom transits back to the ground state, a Lyα photon is emitted. This process of absorption and re-emission looks like that the Lyα photon is "scattered" by the hydrogen atom. This process is thus called Lyα resonant scattering.

The following solution is given by Verhamme et al. (2006). In a static medium,

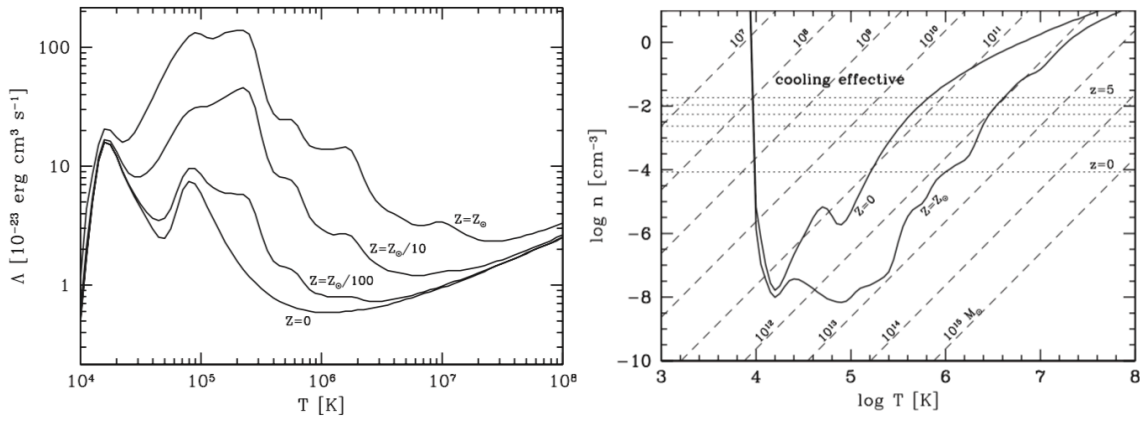

Figure 2.1 **Left:** Cooling functions $\Lambda(T)$ with different gas metallicity Z. The $Z_\odot$ represents the solar metallicity. This figure is based on data in Sutherland, & Dopita (1993) and taken from Mo et al. (2010). **Right:** Number density n as a function of temperature T. The upper and lower solid curves correspond to gas following $t_{\rm cool} = t_{\rm ff}$ with zero and solar metallicity, respectively. Gas with $t_{\rm cool} < t_{\rm ff}$ in the region above these curves can cool effectively. The dashed lines represent different gas masses in a unit of solar mass $M_\odot$. The dotted lines show densities of gas in dark matter halos ($\delta = 200$) at different redshifts. This figure is taken from Mo et al. (2010).

the scattering cross-section in the rest frame of a hydrogen atom is given by

$$\sigma_\nu(\nu) = f_{12}\frac{\pi e^2}{m_{\rm e}c}\frac{\Gamma/4\pi^2}{(\nu-\nu_0)^2+(\Gamma/4\pi)^2}, \tag{2.16}$$

where ν is the frequency of a photon, $f_{12} = 0.4162$ is the oscillator strength, $m_{\rm e}$ is the mass of an electron, e is the electron charge, c is the speed of light, $\nu_0 = 2.466 \times 10^{15}$ Hz is the Lyα frequency, and $\Gamma = A_{12}$ is the damping constant that is related to the natural line width. $A_{12} = 6.265 \times 10^8$ s^{-1} is the Einstein coefficient of Lyα emission.

The optical depth τ_ν of a Lyα photon with a frequency ν passing through the static medium of a length s is then given by

$$\tau_\nu(s) = \int_0^s \int_{-\infty}^{\infty} n(V_z)\sigma_\nu {\rm d}V_z {\rm d}l, \tag{2.17}$$

where n is the number density of hydrogen atoms and V_z is the velocity along the photon's direction.

In Lyα resonant scattering, because the hydrogen atom re-emits a Lyα photon in

the rest frame of the atom, the frequency of the Lyα photon in the observer frame will change if the velocity of the hydrogen atom is not zero. Assuming the atoms in hydrogen gas follow the Maxwell−Boltzmann distribution, the frequency shift x of the re-emission is then given by

$$x = \frac{\nu - \nu_0}{\delta\nu_D}, \tag{2.18}$$

where $\delta\nu_D = V_{\rm th}\nu_0/c$ is the Doppler frequency width and $V_{\rm th} = 12.85T_4^{1/2}$ km s^{-1} is the velocity dispersion. T_4 is the gas temperature in a unit of 10^4 K.

Introducing the Voigt parameter $a = \Gamma/(4\pi\delta\nu_D) = 4.7\times10^{-4}T_4^{-1/2}$, from Equation 2.17 we derive the optical depth $\tau_x(s)$ at a frequency shift x,

$$\tau_x(s) = 1.041 \times 10^{-13}T_4^{-1/2}N_{\rm H}\frac{H(x,a)}{\sqrt{\pi}}, \tag{2.19}$$

where $N_{\rm H}$ is the HI column density. The $H(x,a)$ is the function that describes the Voigt profile,

$$H(x,a) = \frac{a}{\pi}\int_{-\infty}^{\infty}\frac{e^{-y^2}dy}{(y-x)^2+a^2} \approx \begin{cases} e^{-x^2} & \text{if } |x| < x_c \\ \frac{a}{\sqrt{\pi}x^2} & \text{if } |x| > x_c \end{cases}, \tag{2.20}$$

where x_c is a boundary frequency that separates the core and wing regions in the Voigt profile. An approximation of x_c is given by the solution of $e^{-x^2} = \frac{a}{\sqrt{\pi}x^2}$.

The optical depth $\tau_0(s)$ at the Lyα line center is given by

$$\tau_0(s) = 1.041 \times 10^{-13}T_4^{-1/2}N_{\rm H}\frac{H(0,a)}{\sqrt{\pi}} \approx 5.87 \times 10^{-14}T_4^{-1/2}N_{\rm H}. \tag{2.21}$$

For hydrogen gas with $T \sim 2 \times 10^4$ K and $N_H \sim 2 \times 10^{18}$ cm^{-2}, τ_0 is equal to 8.3×10^4 indicating that the hydrogen gas is optically thick for Lyα photons with $x = 0$. Clearly, as the hydrogen gas becomes colder and/or denser, τ_0 becomes larger. Because a typical value of $N_H \sim 10^{19} - 10^{21}$ cm^{-2} has been observed in galaxies (e.g. Kanekar & Chengalur 2003; Chung et al. 2009), Lyα resonant scattering is expected to frequently happen in galaxies. In hydrogen gas with a large τ_0, photons with a large x can escape from the hydrogen gas more easily than those with a small x. As we will see in the next section, this is supported by the broadened and shifted emergent Lyα line.

2.3 Modeling Lyα Emission Line Shapes

Based on the theory of Lyα resonant scattering, many models have been developed to investigate how Lyα resonant scattering affects the Lyα emission line shape. In this section, we introduce the models of expanding spheres and shells calculated by Verhamme et al. (2006) with the Monte Carlo method. These two models will be discussed in Sections 5.2 and 7.2.

2.3.1 Expanding Sphere

In this scenario, we assume an expanding sphere filled by hydrogen gas with a column density $N_{\rm HI}$ measured from the center to the edge. The velocity field is a Hubble-type flow $V(r) = V_{\rm max} r/R_{\rm max}$, where $V_{\rm max}$ is the velocity at the edge $r = R_{\rm max}$. The Lyα photons are generated by a central point source, and are then resonantly scattered by the hydrogen gas in the sphere. The physical mechanism of Lyα resonant scattering is the same as the one we introduced in the previous section, and the detailed algorithm of the simulation is presented in Verhamme et al. (2006). The emergent spectra for varying $N_{\rm HI}$ and $V_{\rm max}$ are shown in Figure 2.2. The values of $N_{\rm HI}$ and $V_{\rm max}$ are adopted to compare with previous studies. Clearly, as $N_{\rm HI}$ increases, the Lyα line width increases, and the line peak is shifted away from the line center. This is because the optical depth at the line center increases, and the Lyα photons are required to move to the wing to escape. As $V_{\rm max}$ increases, the Lyα line peak first moves away from the line center, and then moves back. This is because the optical depth at the line center first increases with the increasing $V_{\rm max}$, but when $V_{\rm max} \gg V_{\rm th}$ the optical depth at the line center becomes small. In Section 5.2, we will use this model to explain the varying line center and line width of our observed Lyα emission.

2.3.2 Expanding Shell

Different from the assumed geometry of a sphere in the previous section, in this scenario let us consider an expanding shell surrounding a central Lyα source. The shell is filled by HI gas with a column density $N_{\rm HI}$ in the radii between $R_{\rm min}$ and $R_{\rm max}$, and expands with a constant velocity $V_{\rm exp}$. The example shown in Verhamme et al. (2006) has the following parameters: $V_{\rm exp} = 300$ km s^{-1}, $N_{\rm HI} = 2 \times 10^{20}$ cm^{-2}, $R_{\rm min} = 0.9 R_{\rm max}$, and $R_{\rm max} = 1.17 \times 10^{19}$ cm, which are commonly used in the

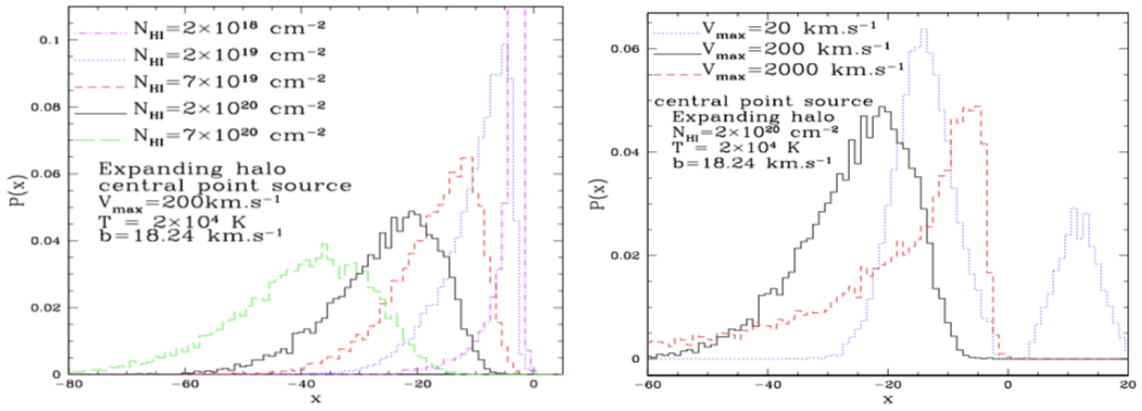

Figure 2.2 Emergent spectra of an expanding sphere of HI gas with varying $N_{\rm HI}$ (left) or $V_{\rm max}$ (right) around a central source. This figure is taken from Verhamme et al. (2006).

literature. The emergent spectrum is shown in the left panel of Figure 2.3. There are 5 features in the emergent spectrum including features 1a, 1b, 1c, 2, and 3. As illustrated in the right panel of Figure 2.3, features 1a and 2 are caused by Lyα photons with no backscattering. Features 1b and 1c correspond to Lyα photons that are scattered back into the shell once and more times, respectively, while the feature 3 can be explained by directly escaped Lyα photons.

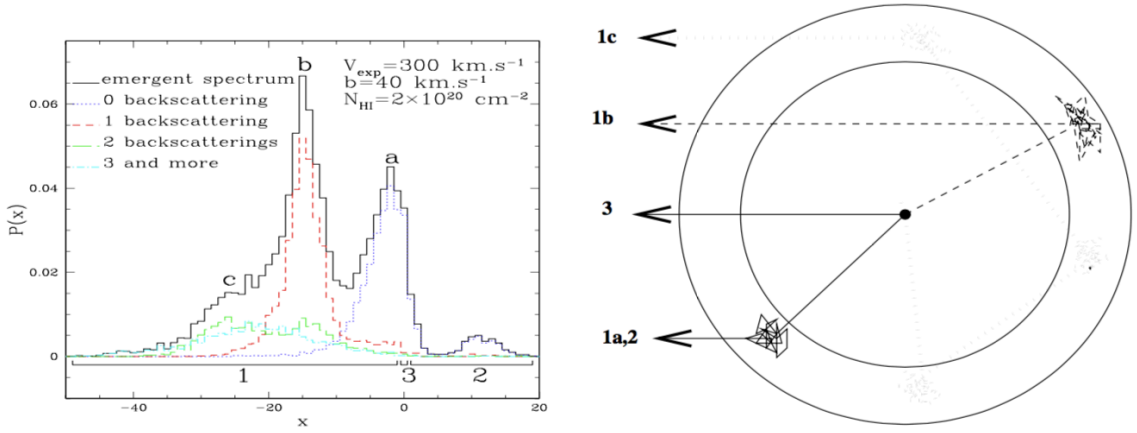

Figure 2.3 Emergent spectrum (left) of an expanding shell of HI gas, and the geometry (right). This figure is taken from Verhamme et al. (2006).

The expanding shell model has been used to fit observed Lyα emission lines by previous studies. For example, various Lyα emission lines from 11 galaxies at z =

$2.8-5.0$ are well fitted by the expanding shell model, showing a success of this model (Verhamme et al. 2008; Figure 2.4). We will discuss this model in Section 7.2 to explain the multiple peaks of our observed Lyα emission.

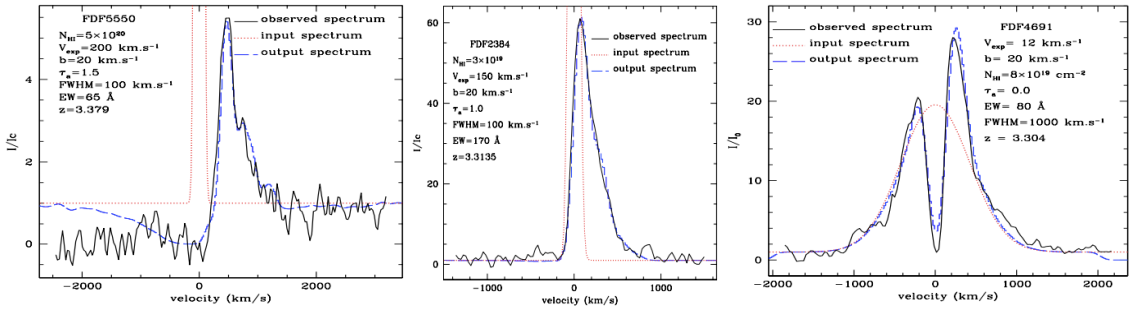

Figure 2.4 Spectra showing Lyα emission lines from 3 LAEs at $z = 3.379$ (left), 3.314 (middle), and 3.304 (right). The black solid line, red dotted line, and blue dashed line are the observed, input, and output spectra, respectively. The output spectrum is calculated by the expanding shell model assuming the input spectrum. The equivalent width (EW) and full width at half maximum (FWHM) of the input spectrum are indicated in each panel. This figure is taken from Verhamme et al. (2008).

2.4 Modeling Lyα Surface Brightness Profiles

Besides the models developed to explain the Lyα line shapes, some other studies have modeled the spatial distribution of Lyα emission, which is the Lyα surface brightness profile. In this section, we introduce a toy model and a cosmological hydrodynamic and radiative transfer model that will be discussed in Sections 7.4 and 7.2, respectively.

2.4.1 A Toy Model for Lyα Resonant Scattering

A toy model for Lyα resonant scattering has been suggested by Steidel et al. (2011; hereafter S11) to explain the observed Lyα surface brightness profile of LAEs at $z \sim 3$. In this model, an expanding sphere with a radius of $R_{\rm eff}$ is filled by isotropic HI clouds with a constant outflow velocity $V_{\rm out}$. The geometry of this model is the same as the one in Section 2.3.1 except for the velocity field. Figure 2.5 shows the geometry of this model. Assuming an HI covering fraction $f_{\rm c}(r)$ that is affected by the HI gas

distribution and velocity field, the probability of a scattering event at a radius r is then given by $\propto f_c(r)/4\pi r^2$, and the probability of a Lyα photon being redirected to the observer's line of sight after scattering is roughly $\propto [1 - f_c(r)]$. The Lyα surface brightness $S_{\mathrm{Ly}\alpha}(b)$ at an impact parameter b is given by the integral along the line of sight:

$$S_{\mathrm{Ly}\alpha}(b) \propto S_0 \int_{-l_{\mathrm{max}}}^{+l_{\mathrm{max}}} \frac{f_{\mathrm{c}}(r)[1 - f_{\mathrm{c}}(r)]}{4\pi r^2} dl, \tag{2.22}$$

where l is the coordinate distance along the line of sight, $l_{\mathrm{max}} = (R_{\mathrm{eff}}^2 - b^2)^{1/2}$, and S_0 is a normalization factor.

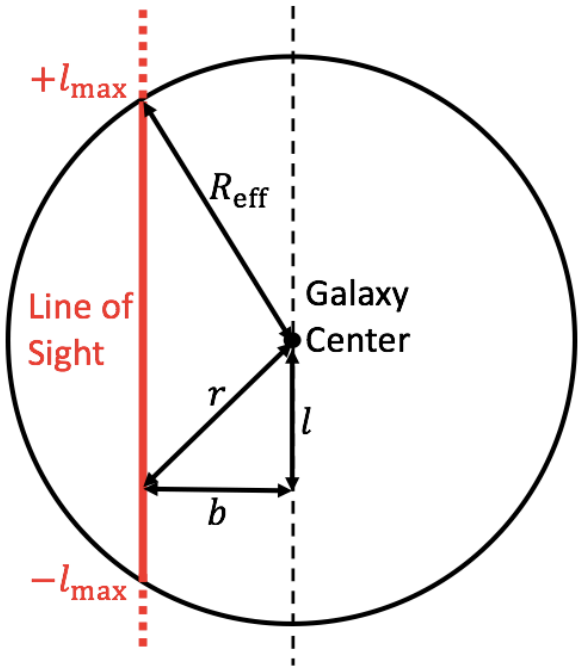

Figure 2.5 Geometry of the toy model for Lyα resonant scattering suggested by S11.

The covering fraction of $f_{\mathrm{c}}(r) \propto (r/r_0)^{-\gamma}$ is found to be a good approximation of SFGs at $z \sim 3$ (S11). The validity of this toy model has been discussed in Steidel et al. (2010; hereafter S10) and S11. S10 investigate multiple absorption lines in SFGs at $z = 2 - 3$, and measure the absorption line strength W_0 using galaxy pairs (pairs of foreground and background galaxies with a small angular separation), as shown in Figure 2.6. The covering fraction $f_{\mathrm{c}} \propto r^{-\gamma}$ can explain the observed W_0-b relations of multiple absorption lines, with γ values ranging from 0.2 to 0.6. Additionally, this

model can well explain the stacked Lyα surface brightness profile observed from SFGs at $z \sim$3, with a best-fit γ value of 0.6 (S11).

Although the assumed geometry in this toy model is simple, the short computational time allows us to fit this model to our observational data for a comparison with S11. We will present the comparison in Section 7.4.

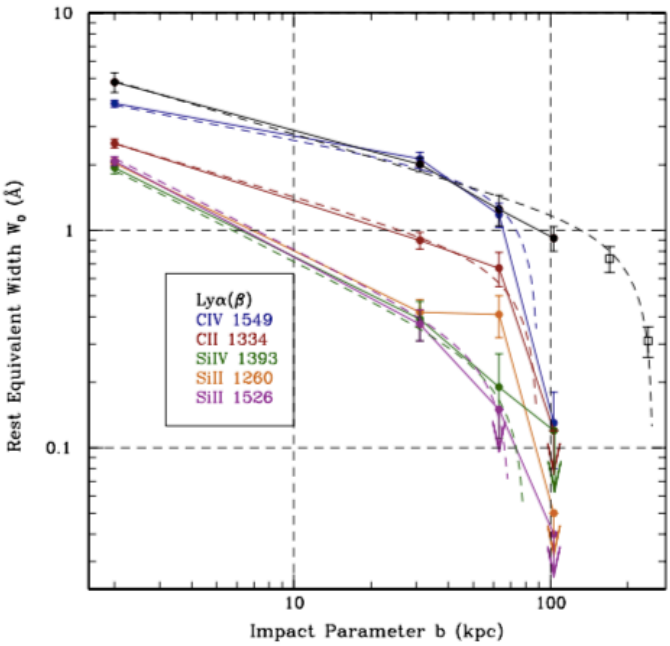

Figure 2.6 Absorption strengths W_0 of multiple absorption lines (solid lines and data points) as a function of impact parameter b. The dashed lines represent the best-fit models. This figure is taken from S10.

2.4.2 A Cosmological Hydrodynamic and Radiative Transfer Model

The models introduced in the previous sections assume simple geometries of HI distribution. With cosmological hydrodynamic simulations, a realistic HI distribution can be modeled. We introduce below the simulations conducted by Yajima et al. (2017; hereafter Y17) and Arata et al. (2018).

With a modified version of the smoothed particle hydrodynamics (SPH) code GADGET-3 (Springel 2005), a cosmological hydrodynamic N-body simulation is performed to trace the dark matter and gas from $z \sim 100$ to ~ 6. Three halos at $z = 6$ are

identified and chosen by the friends-of-friends method, with $M_{\rm h} = 2.4 \times 10^{10} h^{-1} M_{\odot}$ (Halo-10), $1.6 \times 10^{11} h^{-1} M_{\odot}$ (Halo-11), and $7.5 \times 10^{11} h^{-1} M_{\odot}$ (Halo-12) that are typical halo masses of high-z LAEs. Zoom-in simulations are then performed, including the effects of star formation assuming the Chabrier initial mass function (Chabrier 2003), UV background radiation, and supernova feedback. A comparison between the model galaxies and observational data suggests that the models of Halo-11 and Halo-12 well reproduce the star formation rates and stellar masses of the observed LAEs at $z \sim 7 - 8$ (Y17; Figure 2.7).

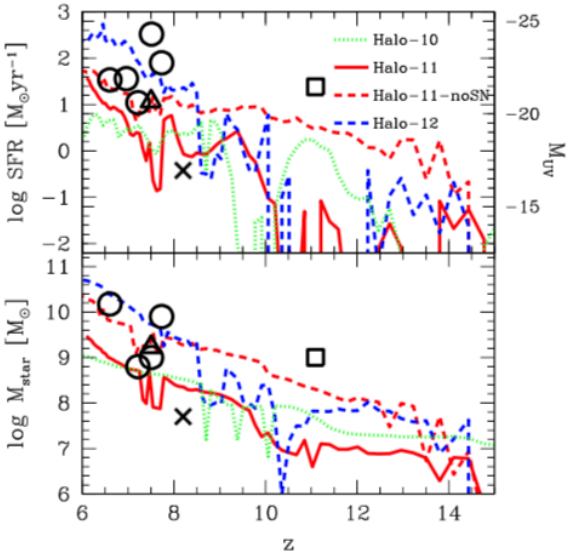

Figure 2.7 SFR (top) and stellar mass (bottom) as a function of redshift for Halo-10 (green dotted line), Halo-11 (red solid line), Halo-11 with no supernova feedback (red dashed line), and Halo-12 (blue dashed line). The black open circles represent LAEs measured from previous observations at $z = 6.6$ (Ouchi et al. 2009), 6.96 (Iye et al. 2006), 7.213 (Ono et al. 2012), 7.3 (Shibuya et al. 2012), 7.51 (Finkelstein et al. 2013), 7.73 (Oesch et al. 2015), and 8.68 (Zitrin et al. 2015). The black open square, open triangle, and cross are a LBG at $z = 11.09$ (Oesch et al. 2016), a submillimeter galaxy at $z = 7.5$ (Watson et al. 2015), and a host galaxy of a gamma-ray burst at $z = 8.2$ (Tanvir et al. 2012) from previous studies, respectively. This figure is taken from Y17.

Based on the 3 model galaxies of Halo-10, Halo-11, and Halo-12, radiative transfer simulations including Lyα resonant scattering and dust absorption are carried out using the Monte Carlo method. The Lyα resonant scattering process is similar to the one we discussed in Section 2.2. Because we cannot use the cosmological hydrody-

namic and radiative transfer simulation to fit our observational data due to the long computational time, we instead compare the 3 model galaxies of Halo-10, Halo-11, and Halo-12 to our result in Section 7.2.

2.5 Cosmological Quantities Used in This Thesis

In this section, we introduce the cosmological quantities that are used in this thesis. The following solutions are given by Hogg (1999).

The Hubble distance $D_{\rm H}$ is given by

$$D_{\rm H} = \frac{c}{H_0}, \tag{2.23}$$

where c is the speed of light, $H_0 = 100h$ km s^{-1} Mpc^{-1} is the present-day Hubble constant, and h is a dimensionless parameter that is set to $h = 70$ in this thesis.

In a flat universe, the comoving distance $D_{\rm C}$ at redshift z on the line of sight is defined by

$$D_{\rm C} = D_{\rm H} \int_0^z \frac{dz'}{\sqrt{\Omega_{\rm M}(1+z')^3 + \Omega_\Lambda}}, \tag{2.24}$$

where $\Omega_{\rm M} = 0.3$ and $\Omega_\Lambda = 0.7$ are the density parameters of matter and dark energy used in this thesis, respectively.

The angular diameter distance $D_{\rm A}$ is then

$$D_{\rm A} = \frac{x}{\theta} = \frac{D_{\rm C}}{1+z}, \tag{2.25}$$

where x is the physical size of an object and θ is the angular size of the object as viewed by an observer.

The luminosity distance $D_{\rm L}$ is related to $D_{\rm A}$ by

$$D_{\rm L} = (1+z)^2 D_{\rm A}. \tag{2.26}$$

We can then use $D_{\rm L}$ to calculate the luminosity L of an object,

$$L = 4\pi F D_{\rm L}^2, \tag{2.27}$$

where F is the flux of the object.

In practice, we calculate the cosmological quantities above using the Ned Wright's Cosmology Calculator (Wright 2006).

CHAPTER 3
IMAGING DATASETS

In order to identify new LABs at $z \sim 4-5$ and $z \gtrsim 7$, we need new imaging data. In this chapter, we introduce the imaging observations and data reduction.

3.1 Imaging Observations

We carried out narrowband imaging observations with Subaru/Hyper Suprime-Cam (HSC; Figure 3.1; Miyazaki et al. 2018; Komiyama et al. 2018; Kawanomoto et al. 2018; Furusawa et al. 2018) in the course of project Cosmic HydrOgen Reionization Unveiled with Subaru (CHORUS; PI: A. K. Inoue). We used two narrowbands of NB718 (λ_c = 7170 Å, FWHM=110 Å) and NB973 (λ_c = 9715 Å, FWHM=100 Å). The central wavelengths of NB718 and NB973 filters were chosen to detect redshifted Lyα emission at $z = 4.9$ and 7.0, respectively. The NB718 data were taken on February 25, March 23, and March 25, 2017, while the NB973 observations were conducted on January 26 and 28, 2017. The NB718 observations covered the COSMOS field, and the NB973 observations were carried out in the SXDS and COSMOS fields. The exposure time for NB718 was $\sim$ 6 hours in the COSMOS field, while the exposure times for NB973 were $\sim$ 15 hours in the COSMOS field and $\sim$ 5 hours in the SXDS field. The effective survey areas were 1.64 and 1.50 deg^2 in the COSMOS and SXDS fields, respectively. The typical seeing sizes during observations were $0\farcs6 - 0\farcs9$.

3.2 Imaging Data Reduction

We reduce the NB718 images with the HSC pipeline (Bosch et al. 2018) that uses codes from the Large Synoptic Survey Telescope (LSST) pipeline (Ivezić et al. 2008; Axelrod et al. 2010; Jurić et al. 2015). We reduce the NB718 data with procedures including bias subtraction, dark subtraction, flat-field calibration, stacking, calibrations of astrometry and photometry, source detection and measurement, and multi-band catalog generation with forced photometry. We calibrate the astrometry and photometry with the imaging data from the Panoramic Survey Telescope and Rapid Response System 1 (Pan-STARRS1; Schlafly et al. 2012; Tonry et al. 2012; Magnier et al. 2013) survey. Details of the source detection and forced photometry are described

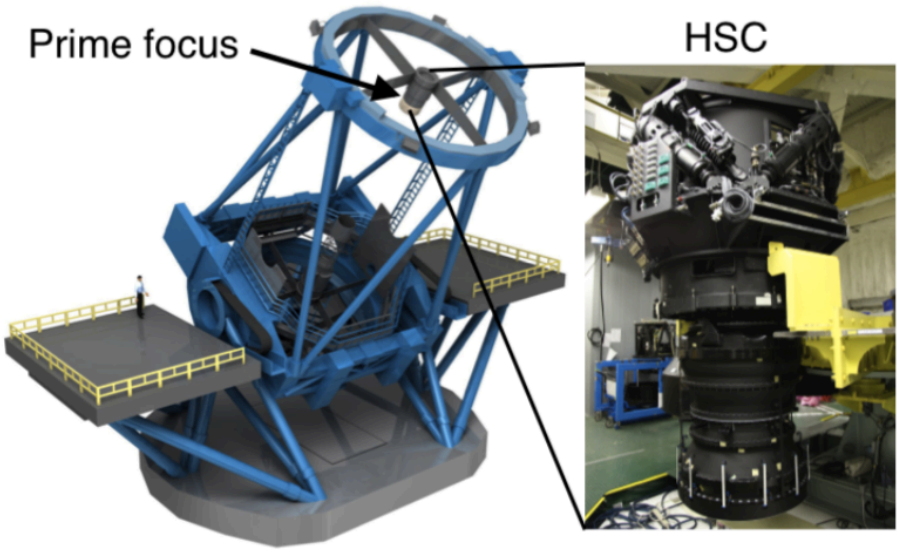

Figure 3.1 The Subaru Telescope (left) and HSC (right). This figure is taken from the Subaru official website.

in Bosch et al. (2018). We do not use exposures with seeing sizes larger than 0.″9 during the reduction because these exposures were taken under bad weather conditions. Itoh et al. (2018) carry out the reduction of NB973 images in a manner similar to ours. The total integration times of the reduced images are 6.3 hours for NB718, 14.7 hours for NB973 in COSMOS field, and 4.7 hours for NB973 in SXDS field. The 5σ limiting magnitudes of NB718 data are 25.6 mag at the center and 24.8 mag at the edge of the field. For NB973 data in COSMOS field, the 5σ limiting magnitude ranges from 23.8 mag at the edge to 24.5 mag at the center. The 5σ limiting magnitudes of the NB973 data in SXDS field are 24.1 mag at the center and 23.2 mag at the edge. The seeing size (in FWHM) of the NB718 data is $\sim 0.7''$, while for NB973 data the seeing sizes are $\sim 0.6''$ in COSMOS field and $\sim 0.8''$ in SXDS field. The seeing size in the field center is generally smaller than that at the edge of the field. We discuss the positional difference of the image quality in detail in Section 6.1. The maps of integration times, 5σ limiting magnitudes, and seeing sizes of NB718 and NB973 data are presented in Figures 3.2, 3.3, and 3.4. Because the inhomogeneities of integration times, limiting magnitudes, and seeing sizes at the field edge are larger than those at the field center, we do not use the images at the edge of the field.

During the reduction, in addition to the NB718 and NB973 images we also use the ultra-deep layer data of broadbands (g, r, i, z, and y) from the Subaru Strategic

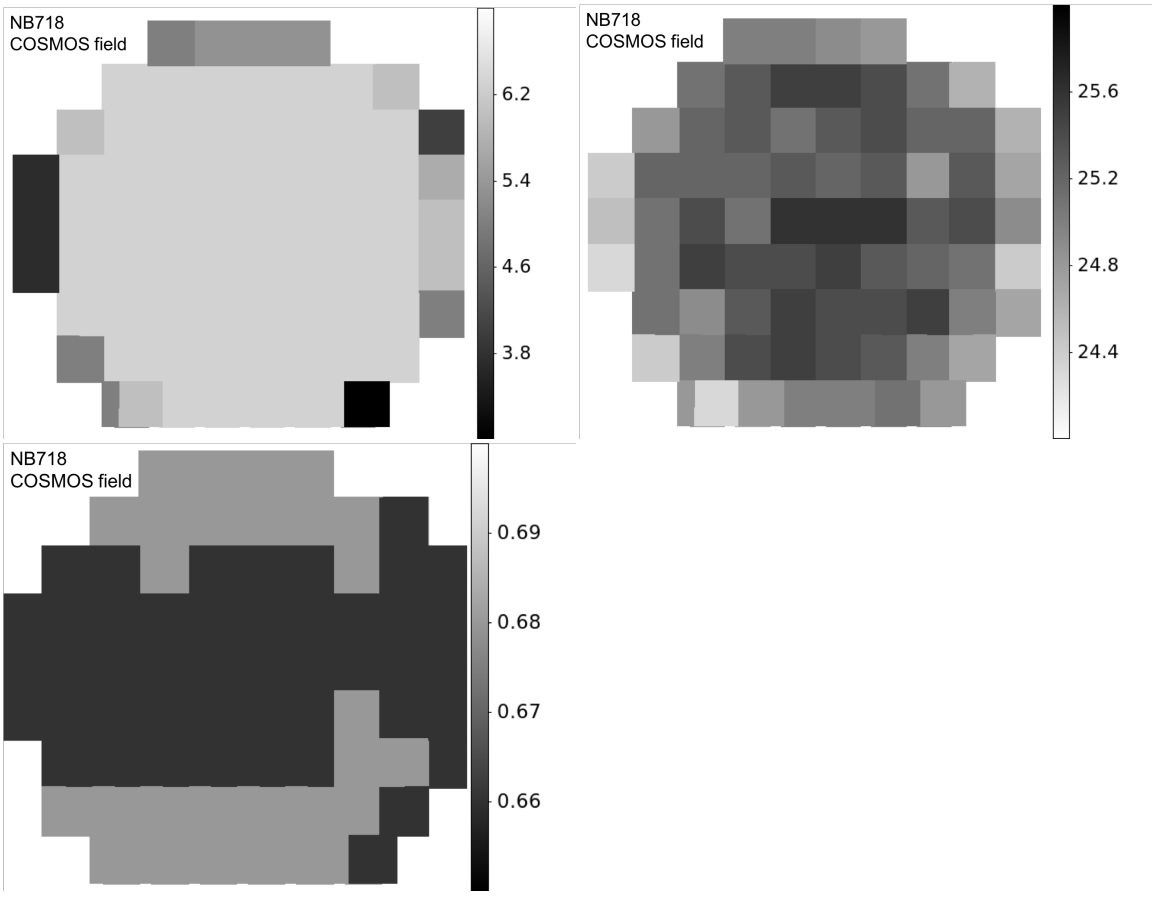

Figure 3.2 Maps of integration time (top left), 5σ limiting magnitude (top right), and seeing size (bottom) of NB718 data in COSMOS field. The image in each field is divided into many sub-areas, named "patches" (Aihara et al. 2018). The size of a patch is $\sim 12' \times 12'$. We measure the image qualities in each of the patches. The colorbars indicate the integration time in a unit of hour, the limiting magnitudes measured in a $2''.0$-diameter aperture, and the seeing size in a unit of arcsec. In the top left panel, a uniform gray color can be found in most of the patches. This is because the integration time in most of the patches is homogeneous. On the other hand, the limiting magnitude has a larger variation than the integration time, which is possibly caused by different filter transmission or sky conditions in different patches.

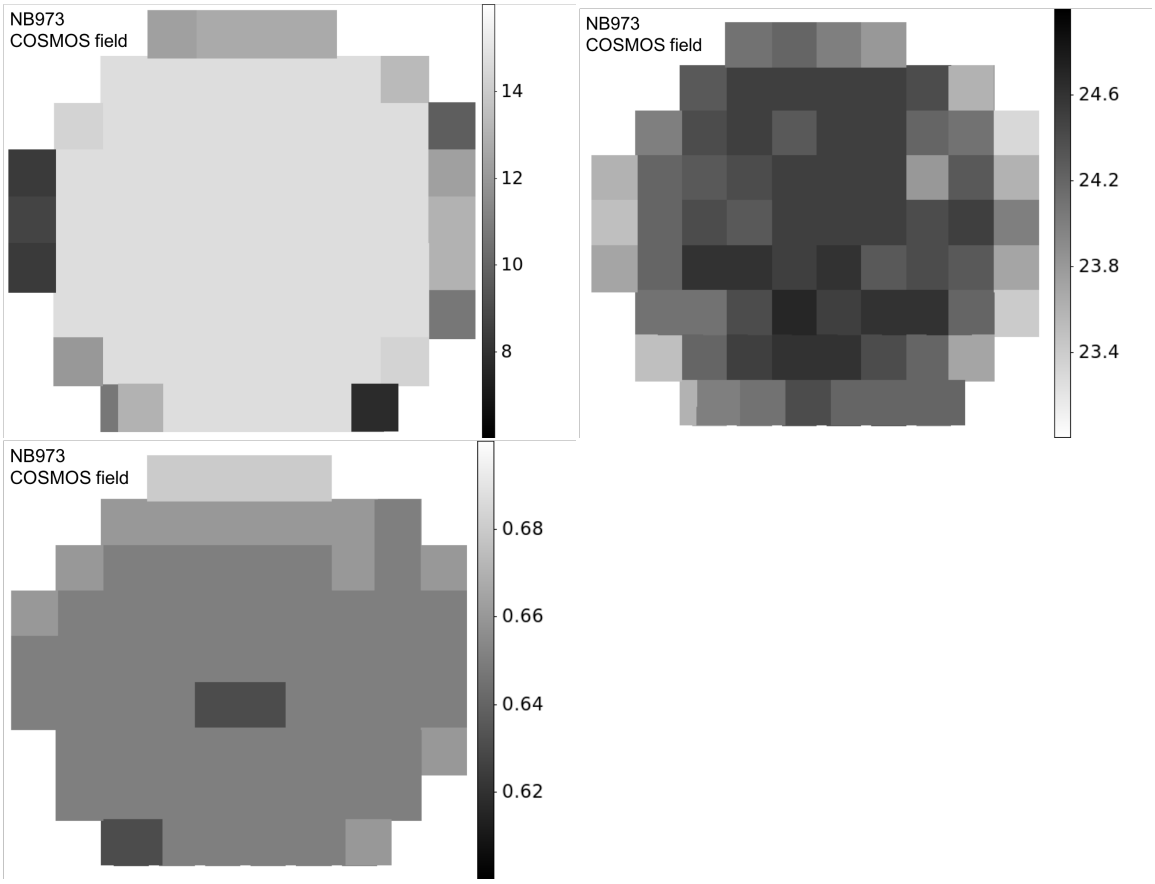

Figure 3.3 Same as Figure 3.2, but for NB973 data in the COSMOS field.

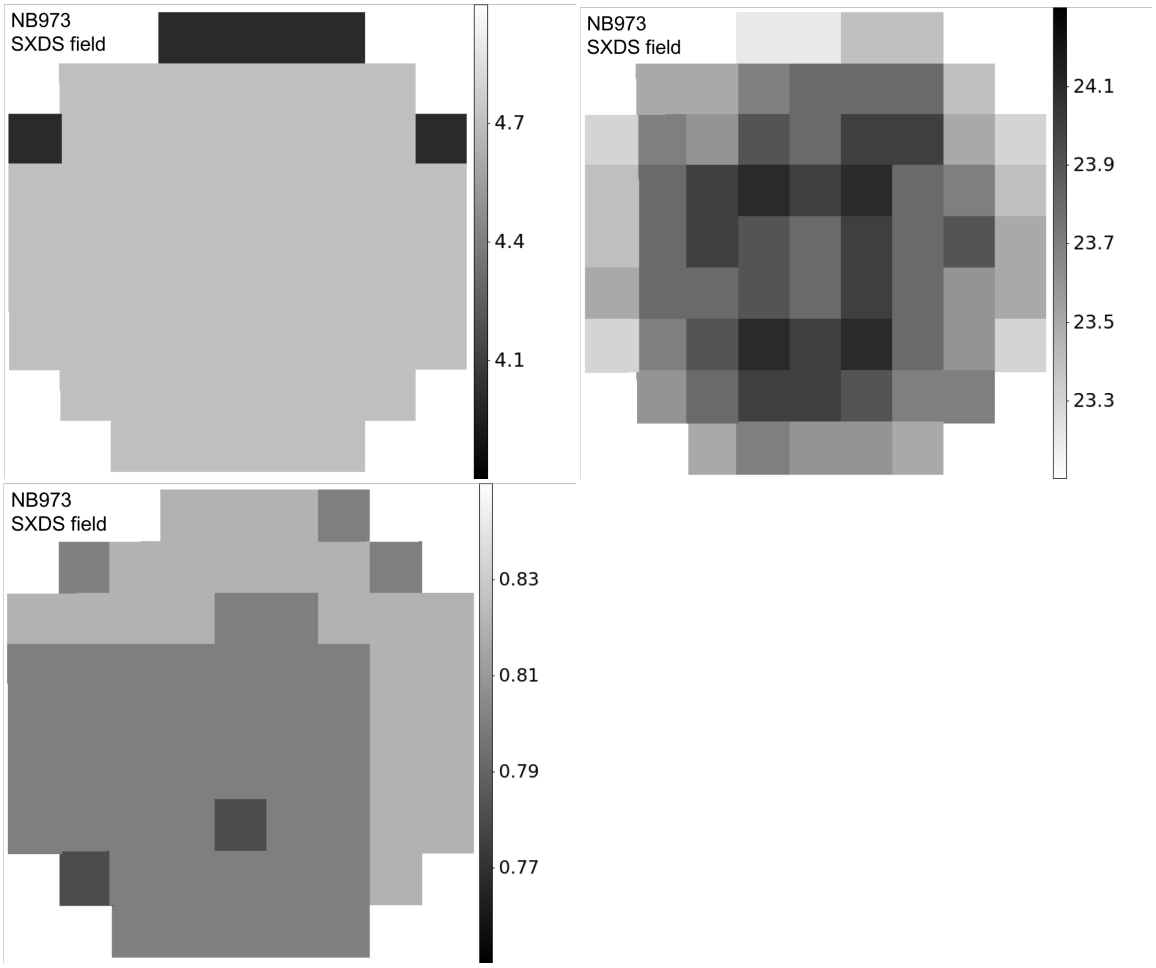

Figure 3.4 Same as Figure 3.2, but for NB973 data in the SXDS field.

Program (SSP) survey (PI: S. Miyazaki; Aihara et al. 2018) for source detection and forced photometry. The SSP survey is a deep and wide-field survey that has been awarded 300 nights over 5-6 years, starting from March 2014. The observational footprints of the SSP survey are shown in Figure 3.5. The details of image qualities are summarized in Table 3.1. The response curves of the filters we use in the SSP and CHORUS surveys are shown in Figure 3.6. We do not use areas contaminated either by halos of bright stars (Coupon et al. 2018) or low signal-to-noise ratio pixels such as field edges. The catalogs produced in this procedure are referred to as source catalogs in the following sections.

Table 3.1 Qualities of Imaging Data

Filter	Exposure (min)	Seeing ($''$)	5σ Depth (mag)
$g^{\rm a}$	70	0.74	27.4
$r^{\rm a}$	70	0.62	27.3
$i^{\rm a}$	130	0.64	27.0
$z^{\rm a}$	130	0.59	26.4
$y^{\rm a}$	210	0.74	25.6
NB718	$\sim$360	~ 0.7	~ 25
NB816$^{\rm a}$	200	0.60	26.3
NB921$^{\rm a}$	270	0.76	25.8
NB973	$\sim$900	~ 0.6	~ 24

Notes.
[a] Measurements from Aihara et al. (2018)

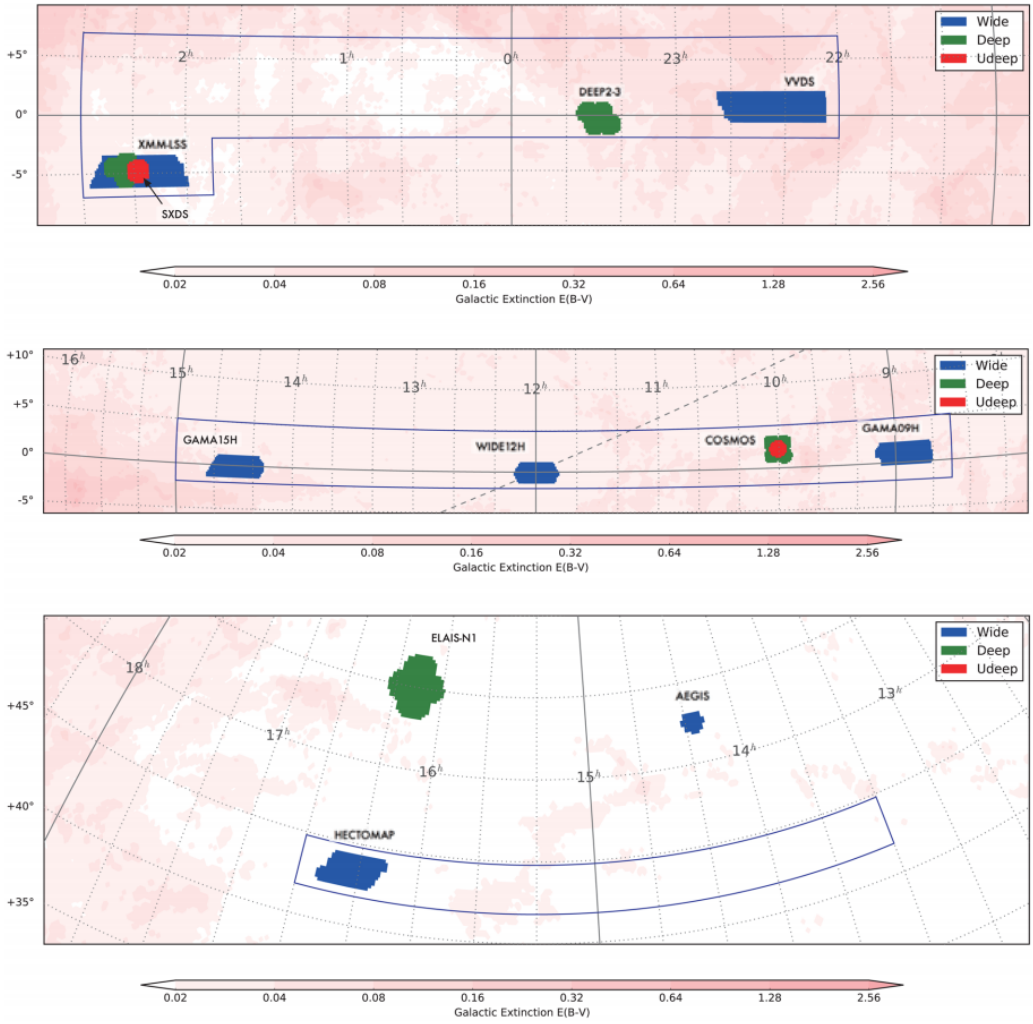

Figure 3.5 Survey map of the SSP survey. In this thesis, we use the ultra-deep (Udeep) layer data in the SXDS and COSMOS fields, and the Deep layer data in the ELAIS-N1 field. This figure is taken from Aihara et al. (2018).

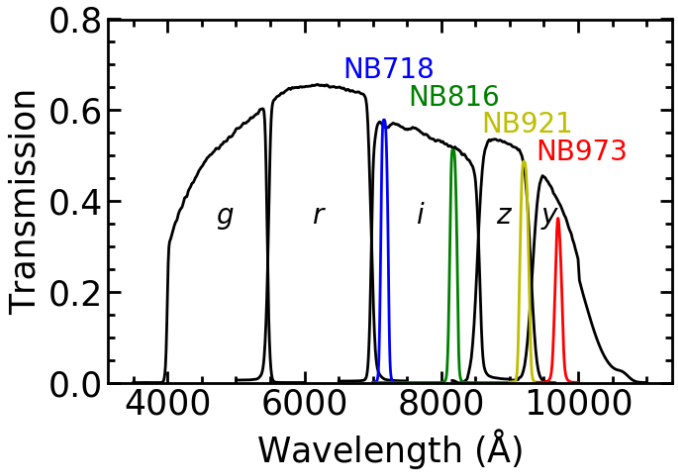

Figure 3.6 Transmission curves of the filters we use in the SSP (g, r, i, z, y, NB816, and NB921) and CHORUS (NB718 and NB973) surveys. The transmission data are taken from https://www.subarutelescope.org/Observing/Instruments/HSC/sensitivity.html.

CHAPTER 4
SAMPLES

4.1 Photometric Samples of LAEs at $z = 4.9$ and 7.0

The combination of narrowband and broadband imaging data can be used to select LAEs at a given redshift. For example, to select LAEs at $z = 4.9$, we use source catalogs of NB718, g, r, and i filters. This is because the NB718 filter has a high signal at the wavelength of the redshifted Lyα emission at $z = 4.9$ ($\lambda = 7174$ Å), while the signals in r and i are low at this wavelength. For LAEs that have bright Lyα emission and faint UV continuum at $z = 4.9$, the magnitude in NB718 would be brighter than those in r and i. Additionally, there would be no detection in g because of the strong IGM absorption at the shorter wavelengths than the Lyα limit ($\lambda = 912$ Å). Following this methodology, we apply the following color criteria,

$$\begin{aligned} ri - NB718 > 0.7 \text{ and } r - i > 0.8 \text{ and } ri - NB718 > (ri - NB718)_{3\sigma} \text{ and} \\ NB718^{\rm ap} < NB718^{\rm ap}_{5\sigma} \text{ and } g^{\rm ap} \geq g^{\rm ap}_{2\sigma}, \end{aligned} \tag{4.1}$$

where the superscription "ap" indicates the aperture magnitude in a $2\farcs0$ diameter, and no superscription corresponds to the total magnitude. The total magnitude is measured by the CModel photometry described in Bosch et al. (2018). The 2σ, 3σ, and 5σ subscriptions stand for 2 sigma, 3 sigma, and 5 sigma detection limits, respectively. In Equation 4.1, ri is calculated by the linear combination of the fluxes in r band $f_{\rm r}$ and i band $f_{\rm i}$, following $f_{\rm ri} = 0.3f_{\rm r} + 0.7f_{\rm i}$. The 3σ error of the $ri - NB718$ color is given by $(ri - NB718)_{3\sigma} = -2.5\log(1 \pm 3\sqrt{f^2_{\rm err,ri} + f^2_{\rm err,NB718}}/f_{\rm NB718})$, where $f_{\rm err,ri}$ and $f_{\rm err,NB718}$ are the 1σ errors in ri and $NB718$, respectively. These criteria allow us to choose LAEs with rest-frame Lyα equivalent widths ($\rm EW_0$) greater than 10 Å.

In total, 727 objects meet the color criteria. We then visually inspect these objects and exclude 586 spurious sources such as satellite trails. Finally we obtain 141 LAE candidates at $z = 4.9$. Figure 4.1 shows the color-magnitude diagram of our LAE candidates at $z = 4.9$.

The selection of LAEs at $z = 7.0$ is presented in Itoh et al. (2018). Briefly, Itoh et al. (2018) select LAEs with NB973 and broadbands (g, r, i , z, and y) following

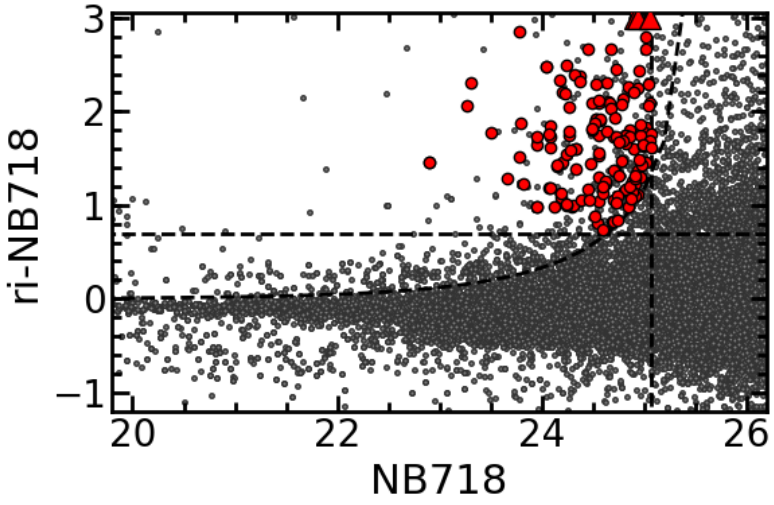

Figure 4.1 Color-magnitude diagram of our LAE candidates at $z = 4.9$. The red filled circles and triangles are the selected 141 LAE candidates. The triangles denote the LAEs whose ri-NB718 colors are greater than 3. The black filled circles are the other objects (including spurious sources) in our source catalog. The dashed lines present the color criteria in Equation 4.1.

the criteria:

$$\begin{gathered}[(y^{\rm ap} < y^{\rm ap}_{3\sigma} \text{ and } y - NB973 > 1) \text{ or } y^{\rm ap} > y^{\rm ap}_{3\sigma}] \text{ and} \\ [(z^{\rm ap} < z^{\rm ap}_{3\sigma} \text{ and } z - y > 2) \text{ or } z^{\rm ap} > z^{\rm ap}_{3\sigma}] \text{ and} \\ NB973^{\rm ap} < NB973^{\rm ap}_{5\sigma} \text{ and } g^{\rm ap} \geq g^{\rm ap}_{2\sigma} \text{ and } r^{\rm ap} \geq r^{\rm ap}_{2\sigma} \text{ and } i^{\rm ap} \geq i^{\rm ap}_{2\sigma},\end{gathered} \tag{4.2}$$

where the meanings of superscriptions and subscriptions are the same as Equation 4.1.

Finally, there are 34 LAE candidates at $z = 7.0$ after we conduct the color selection and visual inspection.

4.2 Identification of Two LABs

Figure 4.2 shows isophotal areas as a function of total narrowband magnitude for our LAE candidates at $z = 4.9$ and 7.0. The isophotal area is defined as the area with a surface brightness above the 2σ detection limits. The 2σ detection limits are

$\sim 4 \times 10^{-18}$ and $\sim 5 \times 10^{-18}$ ergs s^{-1} cm^{-2} arcsec^{-2} at $z = 4.9$ and 7.0, respectively. It should be noted that the detection limits of our data are comparable to some previous studies (e.g. Yang et al. 2009, 2010; Shibuya et al. 2018). We estimate the isophotal area-magnitude relations of point sources using the point spread functions (PSFs) in NB718 and NB973 images. We select LAB candidates based on isophotal areas and narrowband magnitudes similar to those in Shibuya et al. (2018). The isophotal areas of LAB candidates are larger than the 2.5σ confidence levels of point sources. The narrowband magnitudes of LAB candidates are brighter than 23.9 mag for NB718 and 24.1 mag for NB973. These two narrowband magnitudes correspond to a Lyα luminosity of $\sim 1.6 \times 10^{43}$ erg s^{-1} if we assume the UV continuum is negligible compared to the Lyα emission. Our criteria of narrowband magnitudes correspond to 24.0 mag at $z \sim 6$ that is used in Shibuya et al. (2018). We consider the changes of the luminosity distances and filter response curves in the calculation.

By the criteria of isophotal areas and narrowband magnitudes, 9 and 1 LAB candidates are selected at $z = 4.9$ and 7.0, respectively, as shown in Figure 4.2. For the first step of our statistical study and follow-up spectroscopy, we select the brightest LAB candidates at $z = 4.9$ and 7.0 that are named as z49-1 (R.A.= $10^{\rm h}01^{\rm m}45.977$, decl.= $+2°02'44.28''$ [J2000]) and z70-1 (R.A.= $10^{\rm h}02^{\rm m}15.521$, decl.= $+2°40'33.23''$ [J2000]), respectively. The objects of z49-1 and z70-1 show largest isophotal areas (157.5 and 42.2 physical kpc^2) and brightest Lyα luminosities (3.5×10^{43} and 2.6×10^{43} erg s^{-1}) that are distinguished from the other LAE candidates at each redshift. The Lyα luminosities of z49-1 and z70-1 are comparable to those of previously known LABs at the other redshifts. Snapshots of z49-1 and z70-1 are presented in Figures 4.3 and 4.4. The images of z49-1 and z70-1 from UltraVista (Y, J, H, and K bands) and Spitzer/IRAC (3.6 μm and 4.5 μm bands) are shown in Figure 4.5, and will be used in Section 6.4.

From previous studies we use 5 LABs including z57-1 and z57-2 (HSC J161927+551144 and HSC J161403+535701 in Shibuya et al. 2018) at $z = 5.7$, z66-1 (Himiko in Ouchi et al. 2009), z66-2 (CR7 in Sobral et al. 2015), and z66-3 (HSC J100334+024546 in Shibuya et al. 2018) at $z = 6.6$. The imaging data are available from the SSP survey. The spectra of z66-1, z66-2, and z66-3 are taken by Ouchi et al. (2009), Sobral et al. (2015), and Shibuya et al. (2018), respectively.

Our final LAB samples include z49-1, z57-1, z57-2, z66-1, z66-2, z66-3 and z70-1 that are referred to as the 7 LABs in the following sections. From the snapshots of

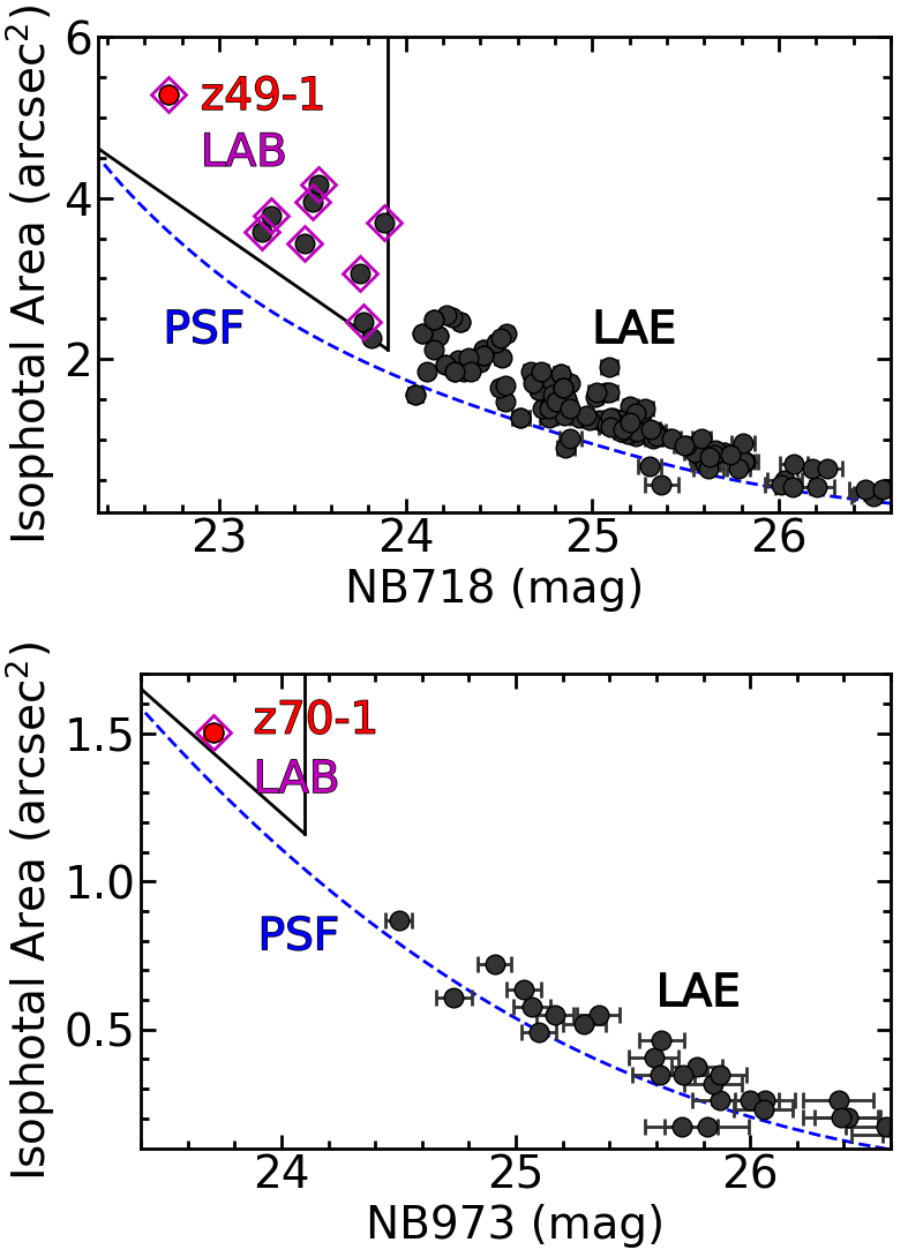

Figure 4.2 Isophotal area as a function of NB718 (top) and NB973 (bottom) magnitudes for LAEs (black filled circles) at $z = 4.9$ and 7.0, respectively. The dashed lines show the size-magnitude relations of point sources. The solid lines represent the selection criteria of LABs. The vertical solid lines correspond to magnitudes of 23.9 mag for NB718 and 24.1 mag for NB973. The diagonal solid lines show the 2.5σ confidence levels of isophotal areas of point sources. The magenta diamond boxes indicate LAB candidates selected with these criteria. The objects of z49-1 and z70-1 are shown as red filled circles. It should be noted that the non-LAB LAEs may also have spatially extended Lyα emission (LAHs). However, we cannot identify individual LAHs as the detection limit of our data is not deep enough. With a deeper detection limit, some non-LAB LAEs may show isophotal areas much larger than the current values.

the 7 LABs in Figures 4.3 and 4.4, we can see that apparently all of the 7 LABs are more extended in the narrowband images (NB718, NB816, NB921, and NB973) than the corresponding offband images (i, z, y, and y). Photometric properties of the 7 LABs are summarized in Table 4.1.

Table 4.1 Photometric Properties of the 7 LABs

ID	Object name	Redshift	$NB_{\rm tot}$ (1)	$BB_{\rm tot}$ (2)	log $L_{{\rm Ly}\alpha}$ (3)	EW$_0$ (Å)	δ (4)
z49-1	-	4.9	22.66	23.89	43.54	47.5	$4.6^{+3.7}_{-2.4}$
z57-1	HSC J161927+551144[a]	5.7	22.88	24.86	43.6	71.4	$1.6^{+5.9}_{-2.2}$
z57-2	HSC J161403+535701[a]	5.7	23.53	25.32	43.2	20.6	$4.1^{+6.8}_{-3.3}$
z66-1	Himiko[b]	6.6	23.55	25.00	43.40	78	$2.1^{+7.1}_{-2.6}$
z66-2	CR7[c]	6.6	23.24	24.92	43.93	211	$0.6^{+3.8}_{-1.3}$
z66-3	HSC J100334+024546[a]	6.6	23.61	24.97	43.50	61.1	$4.3^{+5.1}_{-2.9}$
z70-1	-	7.0	23.40	25.09	43.41	73	$3.7^{+10.7}_{-3.9}$

Notes.
Column 1: total narrowband magnitude in unit of mag.
Column 2: total broadband magnitude in unit of mag.
Column 3: photometric Lyα luminosity in unit of erg s^{-1}.
Column 4: LAE overdensity described in Section 6.2.
[a] Shibuya et al. (2018)
[b] Ouchi et al. (2009)
[c] Sobral et al. (2015)

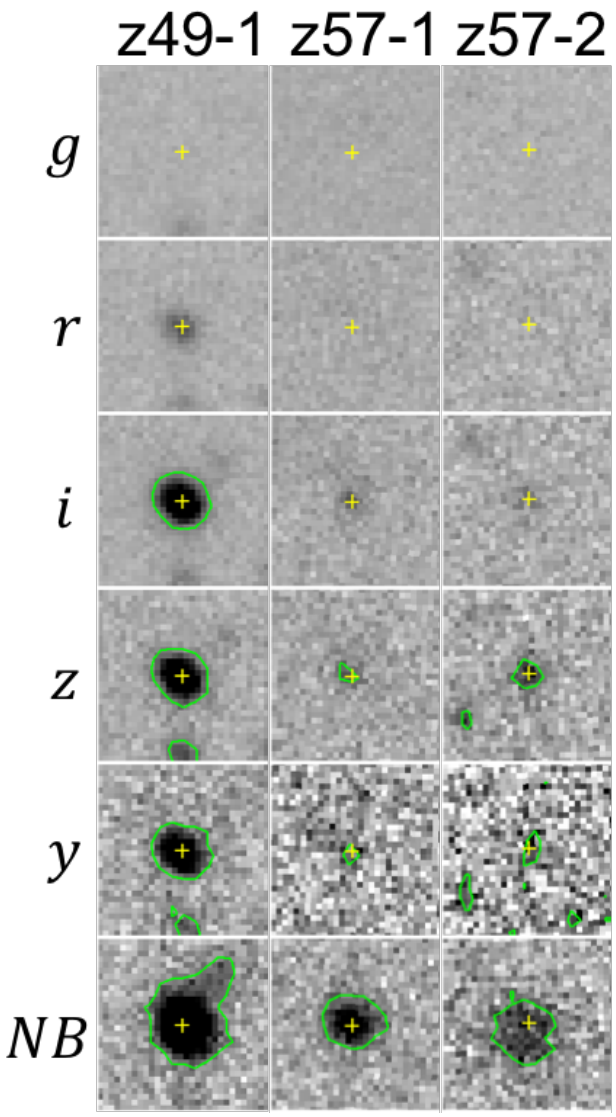

Figure 4.3 Snapshots of z49-1, z57-1, and z57-2. The size of each image is $5'' \times 5''$. The green contours correspond to the 2σ detection limits, and are shown for broadbands redder than the Lyα emission. The Lyα emission is included in the narrowbands. The yellow plus signs indicate the galaxy centers.

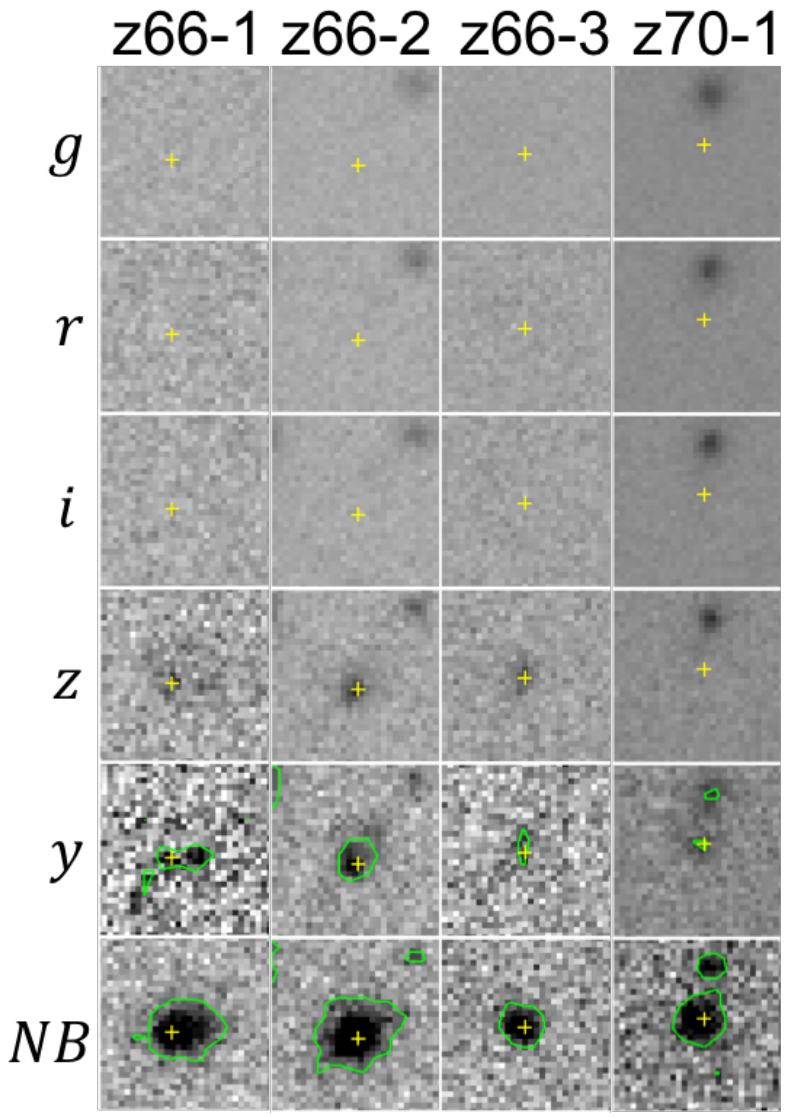

Figure 4.4 Same as Figure 4.3, but for z66-1, z66-2, z66-3, and z70-1. In the panel of z70-1, the object in the center is z70-1, while the other nearby object is a foreground source.

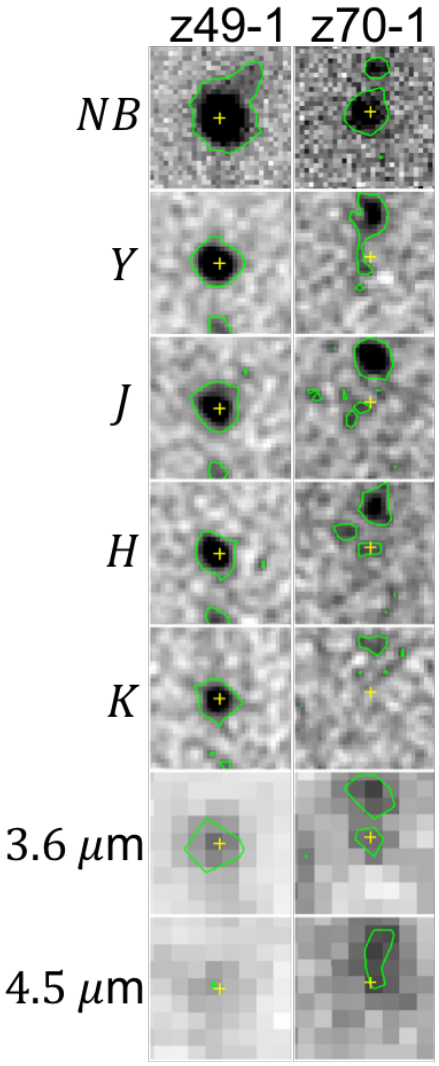

Figure 4.5 Snapshots of z49-1 and z70-1 in narrowband, Y, J, H, K, 3.6 μm, and 4.5μm bands. The Lyα emission is included in the narrowbands. The size of each image is $5'' \times 5''$.

CHAPTER 5
SPECTROSCOPIC DATASETS

5.1 Spectroscopic Observations

Because spectroscopic data are only available for z66-1, z66-2, and z66-3 in the literature, we carry out spectroscopic observations for the other 4 LABs of z49-1, z57-1, z57-2, and z70-1. Details of our spectroscopic observations are presented below.

We carried out spectroscopic observations for z49-1 with Magellan/LDSS3 (Figure 5.1) on May 28, 2017. The object of z49-1 was observed with an on-source exposure time of 1800s. The observations were conducted in the long-slit mode with a slit width of $2\farcs0$. We used the OG590 filter with the VPH-Red grism ($R \simeq 680$) to cover the expected Lyα emission line at $z = 4.9$.

Spectroscopic observations for z70-1 were performed with Keck/DEIMOS (Faber et al. 2003; Figure 5.1) on Jan 6, 2019. The total on-source exposure time was 3.7 hours. However, we only used the data in the last 1.7 hours because the data in the first 2 hours were taken under bad weather conditions. The slit width was $1\farcs0$ during the observations in the multi-object spectroscopy (MOS) mode. The OG550 filter and the 830G grating ($R \simeq 2900$ at 9700 Å) were chosen to cover the wavelength where the Lyα emission line at $z = 7.0$ was expected.

We carried out spectroscopic follow-up observations for z57-1 and z57-2 with Subaru/FOCAS (Figure 5.1) on July 17, 2018. We chose a slit width of $0\farcs8$ in the MOS mode. The O58 filter and VPH900 grism ($R \simeq 1500$) were used to cover the expected Lyα emission line at $z = 5.7$. Finally, we obtained data with an on-source exposure time of 1200s for each target.

Details of spectroscopic observations of the 7 LABs are summarized in Table 5.1.

5.2 Spectroscopic Analysis

The spectrum of z70-1 is shown in Figure 5.2. Because the emission line at 9686 Å is partly overlapped by nearby sky lines, the line shape may be affected by the sky residual after sky subtraction. This emission line cannot be explained by an OII doublet, because the two peaks of an OII doublet at this wavelength would have a separation of ~ 8 Å that is broader than the line observed. We find no other emission

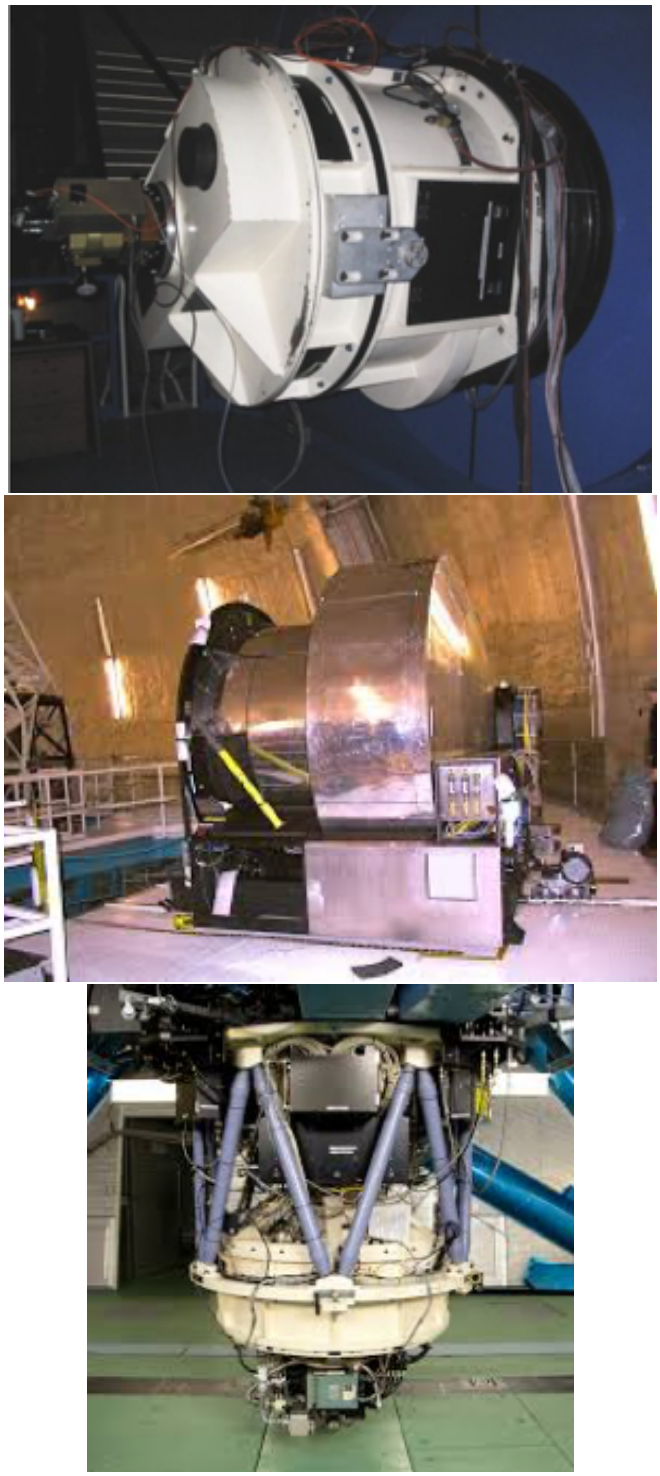

Figure 5.1 Spectroscopy instruments of Magellan/LDSS3 (top; courtesy: the Magellan Telescopes), Keck/DEIMOS (middle; courtesy: the W. M. Keck Observatory), and Subaru/FOCAS (bottom; courtesy: the Subaru Telescope).

Table 5.1 Summary of Spectroscopy

ID	Instrument	Filter	Grism/grating	Exp. time (s)	Slit width (″)	$z_{\rm spec}$
z49-1	Magellan/LDSS3	OG590	VPH-Red	1,800	2.0	4.888
z57-1	Subaru/FOCAS	O58	VPH900	1,200	0.8	5.709
z57-2	Subaru/FOCAS	O58	VPH900	1,200	0.8	5.733
z66-1[a]	Keck/DEIMOS	GG495	830G	10,800	1.0	6.595
z66-2[b]	VLT/X-SHOOTER	-	-	8,100	0.9	6.604
z66-3[c]	Subaru/FOCAS	O58	VPH900	6,000	0.8	6.575
z70-1	Keck/DEIMOS	OG550	830G	6,000	1.0	6.965

Notes.
[a] Ouchi et al. (2009)
[b] Sobral et al. (2015)
[c] Shibuya et al. (2018)

lines between $\sim$ 6000 and 10000 Å that indicate a foreground source. We conclude that z70-1 is not likely a low-z object but a LAB at $z = 6.965$.

Figure 5.3 presents the spectra of z49-1, z57-1, z57-2, z66-1, z66-2, and z66-3. The spectrum of z49-1 shows an emission line whose line center is at 7160 Å. The line center is measured by fitting a Gaussian function to the emission line. Additionally, on the spectrum we find another emission line whose line-center is at 9131 Å, as presented in Figure 5.4. These two emission lines can only be explained by an object emitting Lyα and CIV lines simultaneously at $z = 4.888$. The emission line at 7160 Å is asymmetric and has a red wing that is a typical feature of a high-z Lyα emission line. The object of z49-1 is confirmed as a LAB at $z = 4.888$. The Lyα and CIV fluxes of z49-1 measured from the spectrum are $1.52 \pm 0.048 \times 10^{-16}$ and $1.61 \pm 0.29 \times 10^{-17}$ erg s^{-1} cm^{-2}, respectively.

Figure 5.5 shows the line-center offset $\Delta\lambda_{\rm c}$ and FWHM of the Lyα emission line as a function of positional offset Δd. The Δd is the distance between the position of a measurement and a Lyα source center. By definition, the Lyα-source center is located at $\Delta d = 0$. The positive direction of Δd is from the blueshifted side to the redshifted side. The $\Delta\lambda_{\rm c}$ is calculated following $\Delta\lambda_{\rm c} = \lambda_{\rm c}(\Delta d) - \lambda_{\rm c}(0)$. Because the Ly$\alpha$ emission line of z70-1 is affected by nearby sky lines as we discussed earlier, we do not include z70-1 in this analysis. In Figure 5.5, the $\Delta\lambda_{\rm c}$ has a positive correlation with Δd although the correlation for z66-2 is weak. The correlation between $\Delta\lambda_{\rm c}$

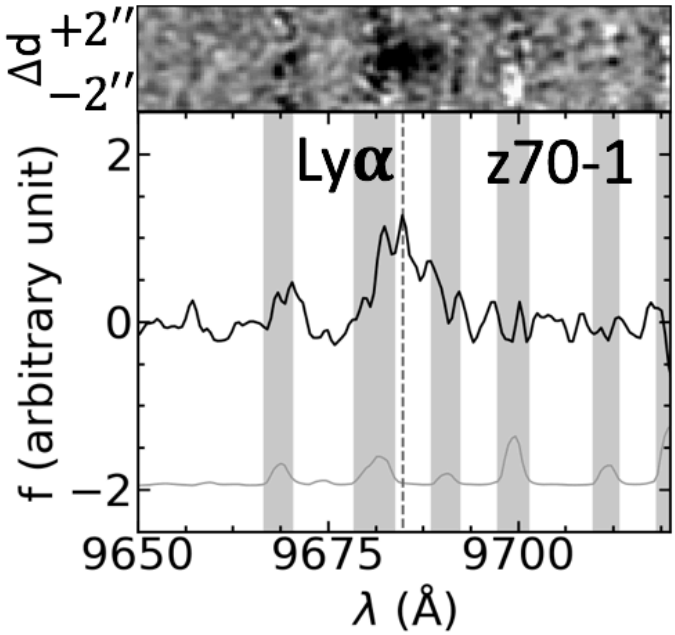

Figure 5.2 Two-dimensional (top) and one-dimensional (bottom) spectra that show the Lyα emission (black solid line) of z70-1. The vertical dashed line indicates the Lyα line center. The gray solid line presents the sky emission lines. The gray shades represent the wavelength ranges with strong sky emission.

and Δd indicates velocity gradients in the the Lyα emission lines of our LABs. We notice that the FWHM also positively correlates with Δd. Clearly z49-1 and z57-2 have larger velocity gradients and FWHMs than the other LABs. Because different HI column densities may cause different line-center offsets and FWHMs as we show in Section 2.3, the velocity and line-width gradients in the small scale of 5 kpc may be explained by dynamical systems (e.g. mergers) or a surrounding cloud of thick HI gas with varying column densities.

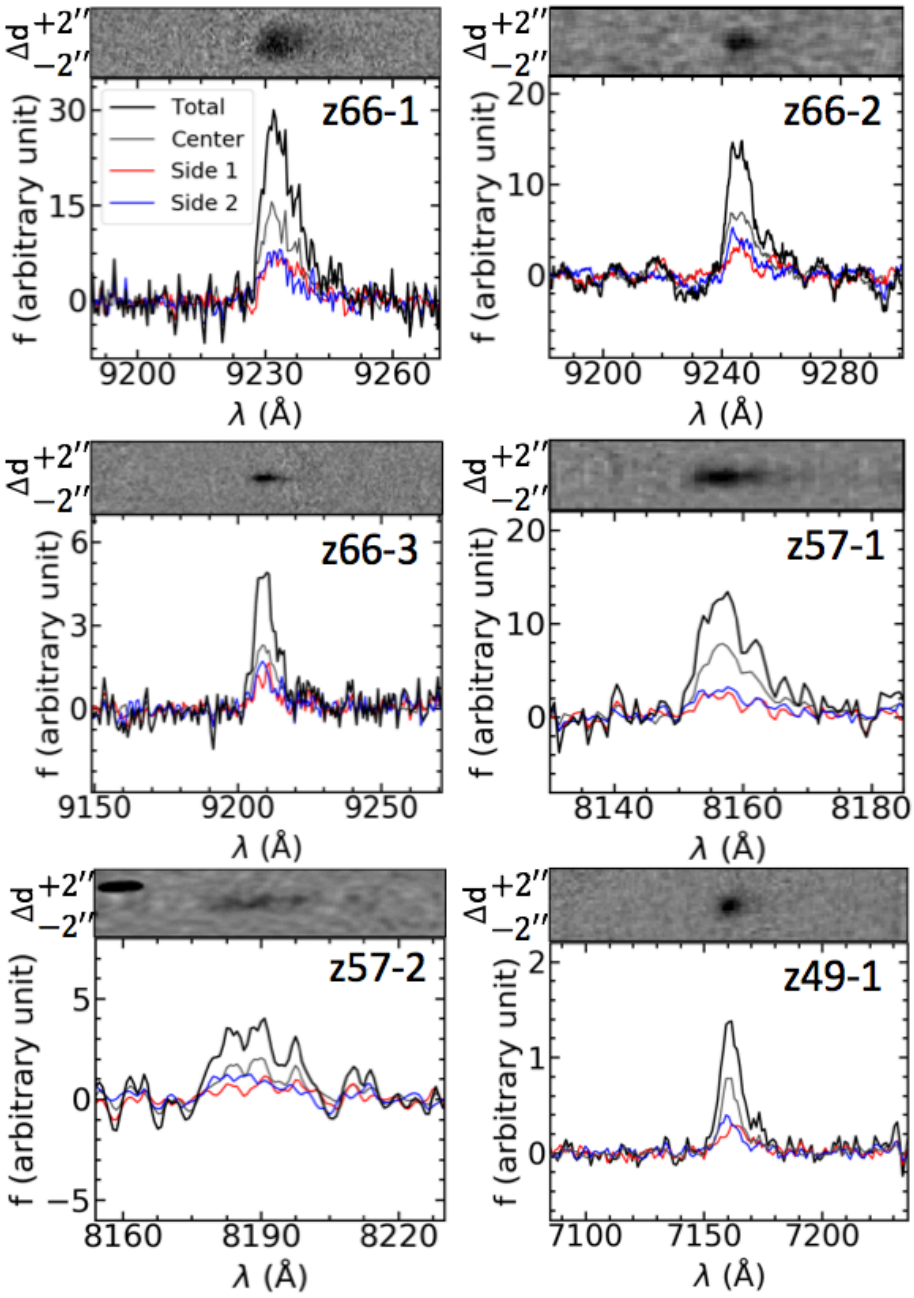

Figure 5.3 Spectra of z49-1, z57-1, z57-2, z66-2, z66-1, and z66-3 that show the Lyα emission lines (black solid lines). In each panel, the two-dimensional spectrum is shown in the top and the one-dimensional spectrum is presented in the bottom. The center (gray), side 1 (red), and side 2 (blue) components are measured at positions with $\Delta d < 0$, $\Delta d = 0$, and $\Delta d > 0$, respectively. The widths of the extraction slits are chosen arbitrarily to let the center, side 1, and side 2 components contain 50±5%, 25±5%, and 25±5% of the total flux, respectively.

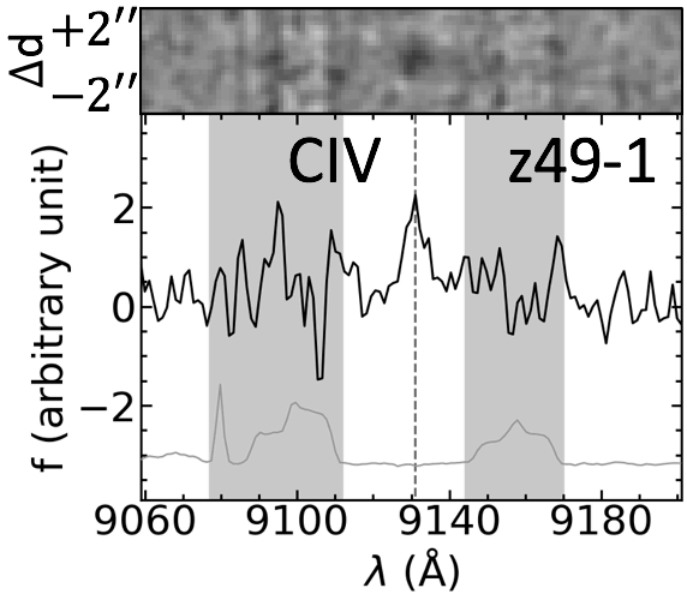

Figure 5.4 Same as Figure 5.2, but for the CIV emission of z49-1.

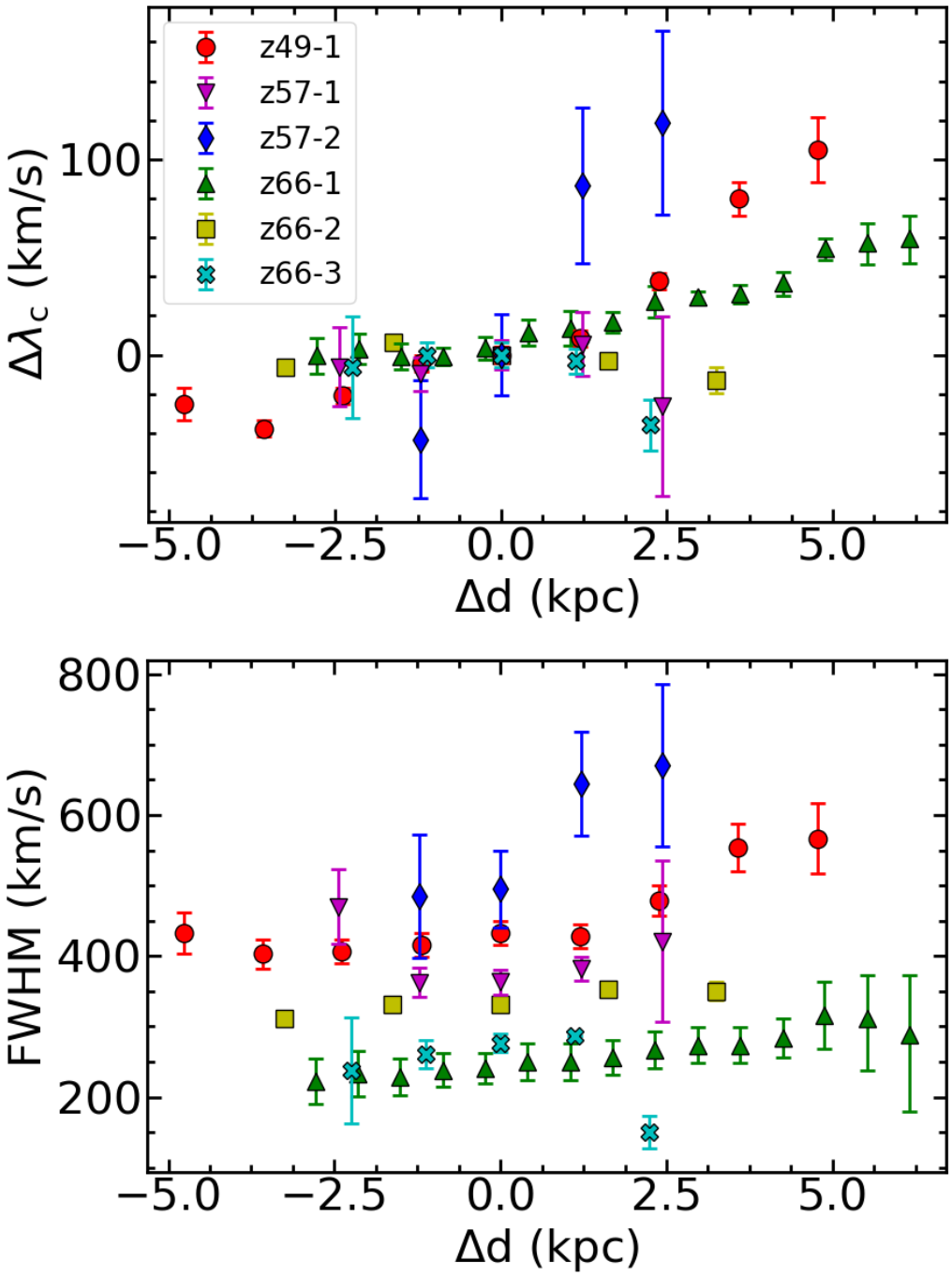

Figure 5.5 Line-center offset $\Delta\lambda_c$ (top) and FWHM (bottom) of the Lyα emission line as a function of positional offset Δd. The data of z66-1 are taken from Ouchi et al. (2009).

CHAPTER 6
DATA ANALYSIS AND RESULTS

6.1 Lyα Surface Brightness Profiles

To make a Lyα image, one would subtract the offband image from the corresponding narrowband image, because the offband image detects the UV continuum while the narrowband image detects both of the UV continuum and Lyα emission. However, if the PSFs of offband and narrowband images are different, the Lyα image obtained by the simple subtraction will not be accurate. For this reason, we homogenize the different PSFs with the following method.

First, we extract the PSFs of narrowband and offband images of our LABs by stacking bright and unsaturated ($19 < m_{\rm AB} < 22$) point sources. Because the PSFs at different locations are different even for the same filter as we indicated in Section 3.2, we only stack point sources selected in a $500'' \times 500''$ region around each LAB. We estimate the uncertainty of the PSFs by stacking the same number of sky images (images with no detected objects) as the point sources. We repeat this process for 100 times. At each radius, we make a histogram of the sky values. We find that the distribution of the sky nearly follows a Gaussian distribution. We fit a Gaussian function to the sky distribution at each radius, and use the best-fit sigma value as the uncertainty of the PSF at this radius. We present the PSF of NB973 with uncertainties in Figure 9.8 in the Appendix. The uncertainty of the NB973 PSF is $< 1\%$ in the center, and increases to $\sim 10\%$ at a radius of $5''$. The NB973 image has the shallowest detection limit among the images we use, and the PSF of the NB973 image shows the largest uncertainty. This suggests that the uncertainties of the PSFs we use are smaller than 10% within a radius of $5''$ (from ~ 32 to $\sim$26 kpc at $z = 4.9 - 7.0$).

After extracting the PSFs (hereafter initial PSFs) of narrowband and offband images of each LAB, we homogenize the PSFs with a method similar to the one discussed in Aniano et al. (2011). The PSF matching procedure is briefly described below.

We choose the PSF with the largest FWHM among initial PSFs as the target PSF. Then we calculate convolution kernels that are used to convolve the initial PSFs

to the target PSF by

$$K = \mathrm{FT}^{-1}\left(\mathrm{FT}(\mathrm{PSF_t}) \times \frac{1}{\mathrm{FT}(\mathrm{PSF_i})}\right), \tag{6.1}$$

where K, FT, FT^{-1}, $\mathrm{PSF_i}$, and $\mathrm{PSF_t}$ stand for the convolution kernel, Fourier transform, inverse Fourier transform, initial PSF, and target PSF, respectively. Finally we convolve the narrowband and offband images of the 7 LABs with the corresponding kernels to obtain PSF-matched images. The PSFs before and after matching are shown in Figure 6.1.

It should be noted that the shapes of our LABs are not exactly circular. We measure the ratio of long axis to short axis (b/a) by fitting a two-dimensional Sérsic profile to the Lyα image. The b/a of our LABs is $\sim 0.8 - 0.9$. We extract the elliptical radial profiles of our LABs with elliptical annuli of the same b/a but varying a. The circularized radius r_{ell} of the elliptical radial profile is defined by $r_{\mathrm{ell}} = a\sqrt{b/a}$. Figure 6.2 shows the elliptical profile of z66-1 compared with the circular profile. Even for z66-1 that has the smallest b/a among our LABs, we see that the elliptical profile is consistent with the circular profile within the 1σ errors. Quantitatively, the circularized half-light radii of our LABs are nearly equal to the half-light radii, with a difference smaller than 12%. This indicates that the radial profiles of our LABs can be estimated by circular ones. For simplicity, we use circular profiles for our analysis.

Figures 6.3 and 6.4 show Lyα surface brightness profiles $S_{\mathrm{Ly}\alpha}$ of the 7 LABs. To account for the filament of z49-1 suggested by the narrowband image, we measure the profile along the direction of the filament. We estimate the uncertainties of the profiles at different radii by measuring sky noises with sky images. We place 100 extraction annuli with a given radius randomly on the sky images, and plot the histograms of sky noises measured in the annuli. We find that the sky noises nearly follow a Gaussian distribution. We fit a Gaussian function to the sky noises, and use the best-fit σ as the uncertainty of the profile. The uncertainties of the Lyα profiles of our LABs are shown in Figures 9.1 to 9.7 in the Appendix.

We define the local sky background around each LAB by the median value in an annulus with inner and outer radii of $5''$ ($\sim$ 30 kpc at $z \sim 6$) and $10''$ ($\sim$ 60 kpc at $z \sim 6$), respectively. Because the effective radii of our LABs (< 10 kpc) are much smaller than 30 kpc, the measurement of the local sky background is not affected by the LABs. For our analysis we use the surface brightness profile with the subtraction

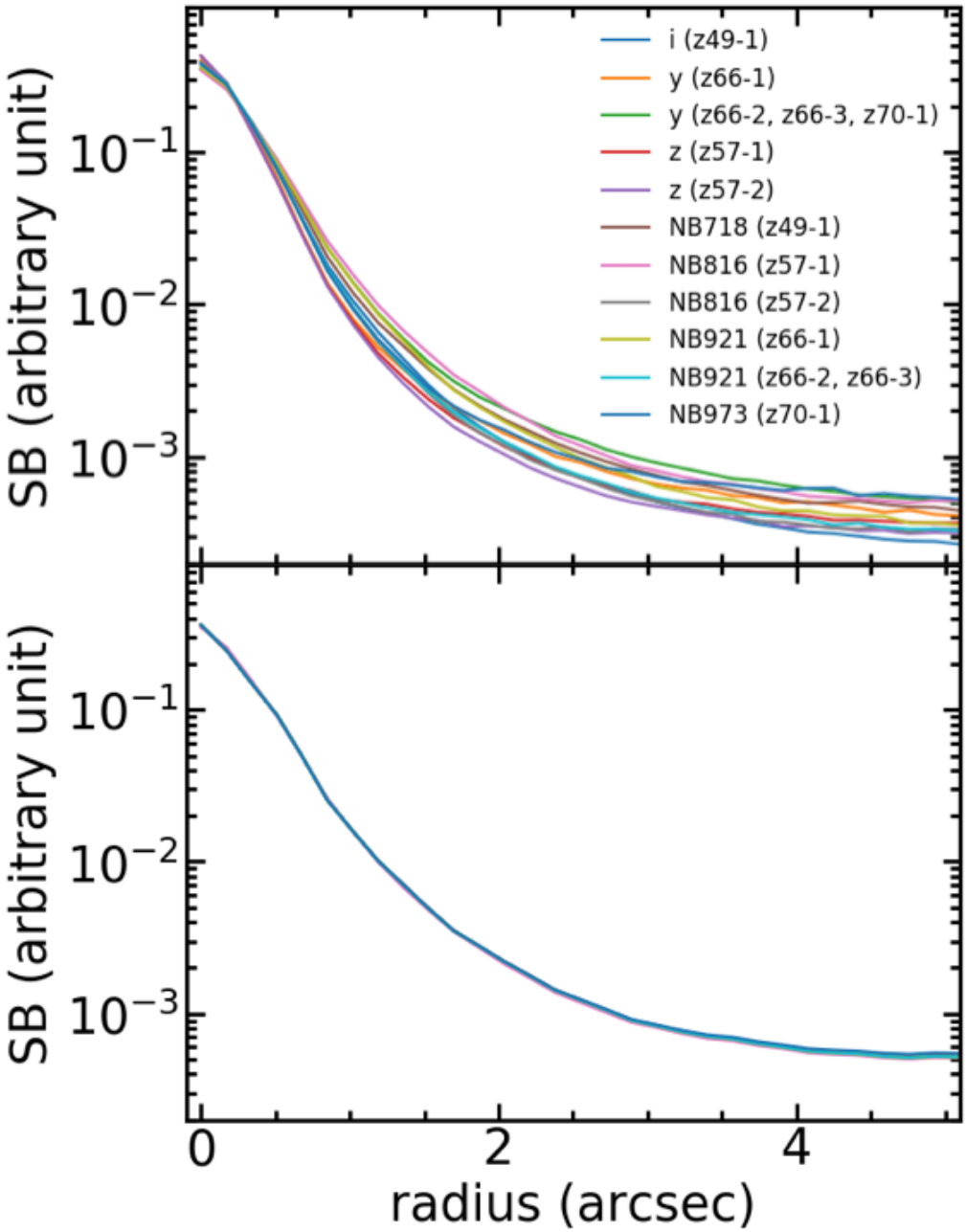

Figure 6.1 PSFs before (top) and after (bottom) matching. The solid lines with different colors represent different PSFs. Each PSF is extracted from a 500×500 arcsec^2 region around each LAB in each filter. The names of filters and LABs are indicated in the legend. Because z66-2, z66-3, and z70-1 reside in the same field (COSMOS), we use the same y-band PSF for z66-2, z66-3, and z70-1. The same NB921 PSF is used for z66-2 and z66-3.

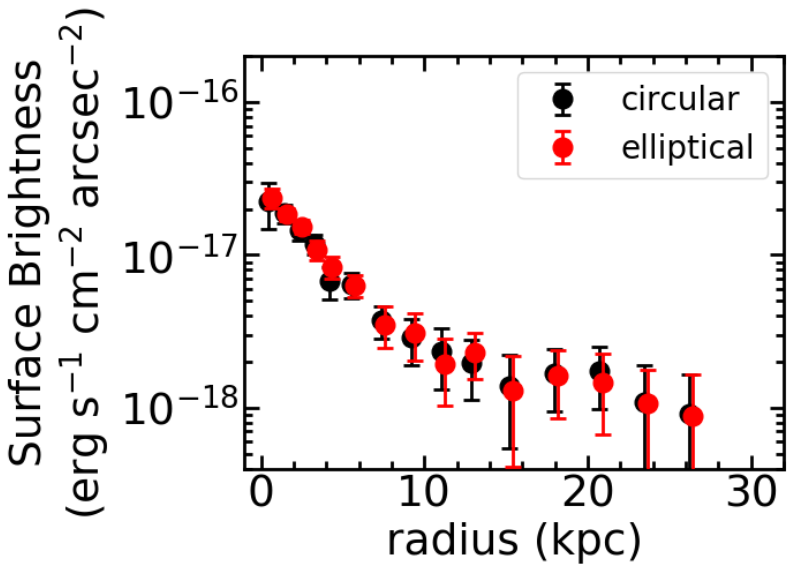

Figure 6.2 Elliptical (red) and circular (black) radial profiles of z66-1. The horizontal axis for the elliptical profile is the circularized radius $r_{\rm ell} = a\sqrt{b/a}$. The elliptical profile is shifted along the horizontal axis by +0.2 kpc.

of the local sky background.

To measure the scale lengths of the 7 LABs, we perform a two-component (core and halo) fitting that is similar to the one adopted by Leclercq et al. (2017) using the least-squares method with the Trust Region Reflective minimization algorithm. Specifically, we decompose the surface brightness profiles into core and halo components, following:

$$\begin{aligned} S_{\rm cont}(r) &= {\rm PSF} * A_1 \exp(-r/r_{\rm c}) \text{ and} \\ S_{{\rm Ly}\alpha}(r) &= {\rm PSF} * [A_2 \exp(-r/r_{\rm c}) + A_3 \exp(-r/r_{\rm h})], \end{aligned} \tag{6.2}$$

where $r_{\rm c}$ and $r_{\rm h}$ are the scale lengths of core and halo components, respectively. The "$*$" sign stands for convolution. The A_1, A_2, and A_3 are free parameters. The continuum profile $S_{\rm cont}$ is extracted from the offband images, while the Lyα profile $S_{{\rm Ly}\alpha}$ is measured in the Lyα images. We first fit $S_{\rm cont}$ with two free parameters A_1 and $r_{\rm c}$ to measure $r_{\rm c}$. Then we fix this $r_{\rm c}$ value to fit $S_{{\rm Ly}\alpha}$ with three free parameters A_2, A_3, and $r_{\rm h}$ to measure $r_{\rm h}$. If we fit the $S_{{\rm Ly}\alpha}$ without fixing $r_{\rm c}$, the core component will dominate the total profile causing a large $r_{\rm c}$ and a small $r_{\rm h}$. The errors of $S_{\rm cont}$ and $S_{{\rm Ly}\alpha}$ are considered in the fitting. Figures 6.3 and 6.4 show the best-fit Lyα

surface brightness profiles of our LABs.

Because there is an offset between the positions of the Lyα and continuum centers of z57-2, we cannot perform the two-component fitting that requires the Lyα and continuum centers to be the same. Instead we use a one-component exponential function to fit the Lyα profile of z57-2 in the halo region ($r \gtrsim 5$ kpc), following

$$S_{\mathrm{Ly}\alpha}(r) = \mathrm{PSF} * [A \exp(-r/r_{\mathrm{s}})], \tag{6.3}$$

where the meanings of the $S_{\mathrm{Ly}\alpha}$, PSF, and "$*$" sign are the same as Equation 6.2. The A is a free parameter. The fitting result of z57-2 is shown in Figure 6.3.

We do not homogenize the different detection limits for our LABs in the fitting, because using the deepest data available for each LAB allows us to estimate the best-fit parameters with the smallest uncertainties. The effect of the different detection limits is included in the parameter uncertainty estimation described below.

We estimate the uncertainties of the best-fit parameters with the Monte Carlo method. At each radius, we randomly add sky noise to the continuum and Lyα profiles assuming a Gaussian distribution. After adding the sky noise, we fit the two-component exponential function the the new profiles. We repeat this process (adding sky noise and profile fitting) for 100 times. We plot the histograms of the best-fit parameters, and calculate the central 68.3% confidence intervals. We use these confidence intervals as the 1σ uncertainties of the best-fit parameters.

The effect of positional variance of PSF shown in Section 3.2 is estimated as follows. We carry out the profile fitting with the target PSFs at the field center (small FWHM) and edge (large FWHM), and find that the best-fit r_{c} of z49-1 varies by ~ 0.1 kpc, much smaller than the uncertainty caused by the sky noise. On the other hand, the best-fit r_{h} changes by ~ 2 kpc, comparable to the uncertainty from the sky noise. This indicates that the effect of positional PSF variance affect r_{h} and r_{c} less than or comparably to the statistical errors.

In Figure 6.2, we show that the elliptical radial profiles of our LABs are consistent with the circular radial profiles. To support this quantitatively, we perform the two-component fitting to the elliptical radial profile of z66-1 that is the least circular among our LABs. The best-fit r_{c} does not change while the best-fit r_{h} changes by $+0.1$ kpc compared to those of the circular profile. This result suggests that the circular profiles are good approximations of the radial profiles of our LABs.

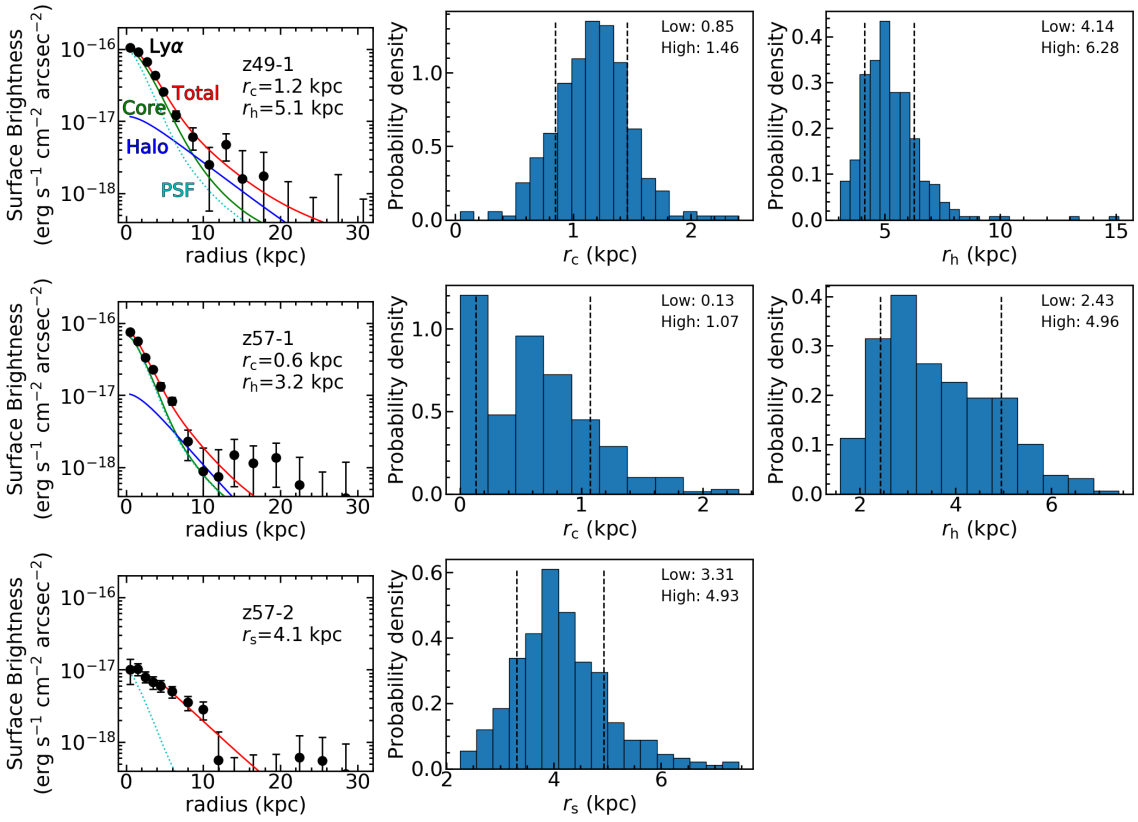

Figure 6.3 Lyα surface brightness profiles (first column), and uncertainties of the best-fit r_c (second column) and r_h (third column) of z49-1 (top), z57-1 (middle), and z57-2 (bottom). In the first column, the black filled circles show the Lyα profile. The red, green, and blue solid curves are the total, core, and halo best-fit models, respectively. The PSF is presented as a cyan dotted line. For z57-2, the red solid line represents the best-fit one-component exponential function. In the second and third columns, the dashed lines indicate the ranges of the central 68.3% confidence levels.

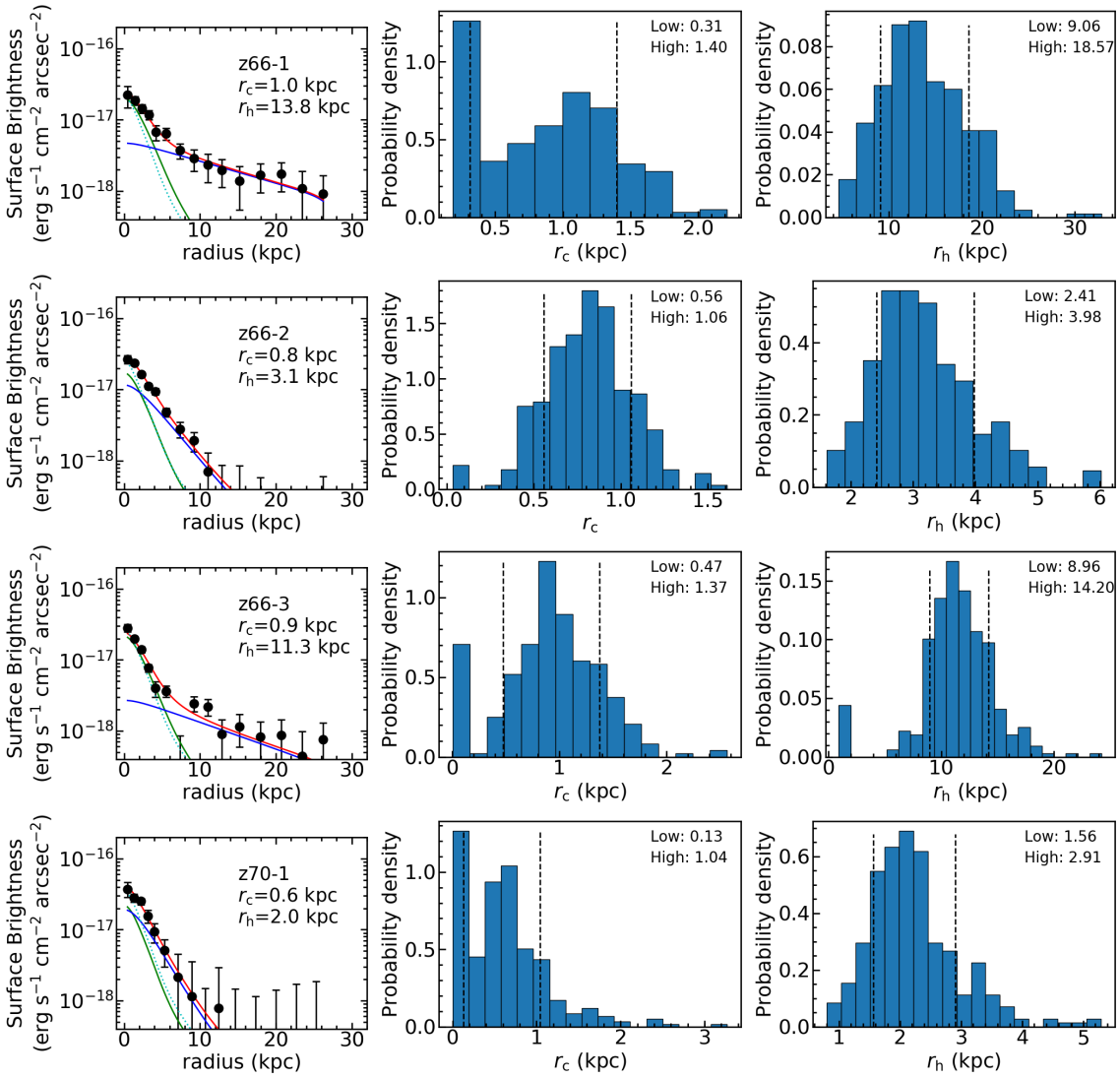

Figure 6.4 Same as Figure 6.3, but for z66-1 (first row), z66-2 (second row), z66-3 (third row), and z70-1 (last row).

We compare the best-fit $r_{\rm h}$ values as a function of Lyα luminosities $L_{\rm Ly\alpha}$, Lyα rest-frame equivalent widths EW$_0$, UV continuum magnitudes $M_{\rm UV}$, and redshifts z of the 7 LABs with those of LAEs from Leclercq et al. (2017), as shown in Figures 6.5, 6.6, and 6.7. When calculating the LAB average value, we do not use the best-fit $r_{\rm h}$ of z57-2 from the one-component exponential function fitting. In Figures 6.5 and 6.6, the relations between the scale lengths and galaxy properties including $L_{\rm Ly\alpha}$, EW$_0$, and $M_{\rm UV}$ of our LABs are similar to those of the MUSE LAHs. This suggests that our LABs and MUSE LAHs possibly have similar connections between the extended Lyα emission and host galaxies, although our LABs are more massive than typical MUSE LAHs. We do not find strong evidences supporting that our LABs and MUSE LAHs are distinct populations. We also find that our LABs are consistent with the positive correlation between the $r_{\rm c}$ as a function of $M_{\rm UV}$ of MUSE LAHs, which is expected from previous studies suggesting that galaxies with brighter $M_{\rm UV}$ have larger continuum sizes (Shibuya et al. 2015, 2019). The positive correlation between the $r_{\rm h}$ as a function of $M_{\rm UV}$ may be explained by the larger amount of cold gas in galaxies with brighter $M_{\rm UV}$ (Oyarzún et al. 2017).

Leclercq et al. (2017) find no significant evolution of the $r_{\rm h}$ of MUSE LAHs at $z = 3 - 6$. Consistently, we notice that in Figure 6.7 the $r_{\rm h}$ of our LABs does not evolve significantly between $z = 4.9$ and 7.0.

Figure 6.8 shows the $r_{\rm h}$ as a function of $r_{\rm c}$ of our LABs. Although generally the $r_{\rm h}$ increases as $r_{\rm c}$ increases, we do not find any clear correlations between the two quantities, which is similar to the result in Leclercq et al. (2017).

6.2 Large Scale Structure around LABs

To investigate the large scale structure around our LABs, we calculate the LAE overdensity δ at $z = 4.9$, 5.7, 6.6, and 7.0 in the same manner as Harikane et al. (2019). The δ is defined as

$$\delta = \frac{n - \bar{n}}{\bar{n}}, \tag{6.4}$$

where n and $\bar{n}$ are the number and average number of LAEs in a cylinder, respectively. The radius of the cylinder is $\sim$10 comoving Mpc (cMpc). We choose this radius because that a protocluster containing LABs at $z \sim 3$ is expected to have a halo mass

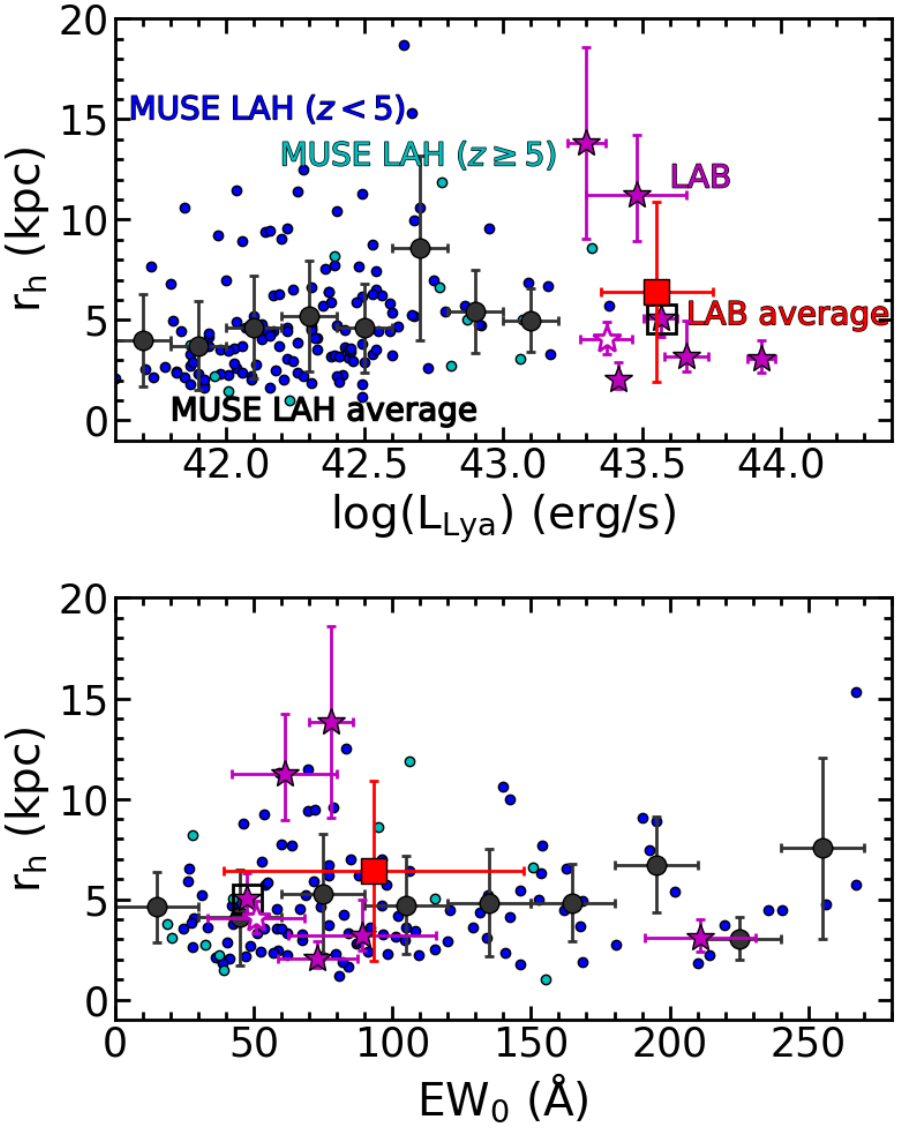

Figure 6.5 Halo scale length as a function of Lyα luminosity (top) and Lyα rest-frame equivalent width (bottom) of the 7 LABs (stars) and LAHs (filled circles) from Leclercq et al. (2017). The empty star represents z57-2 that does not have a two-component fitting result. The red filled square shows the average value of our LABs, with error bars indicating the root mean squares. The MUSE LAHs at $z < 5$ and $z \geq 5$ are blue and cyan filled circles, respectively. The average values of MUSE LAHs are shown as black filled circles. The black horizontal error bar indicates the bin size, while the black vertical error bar is the root mean square. In the top panel, we slightly shift z49-1 (boxed star) along the horizontal axis by +0.03 to avoid overlaps.

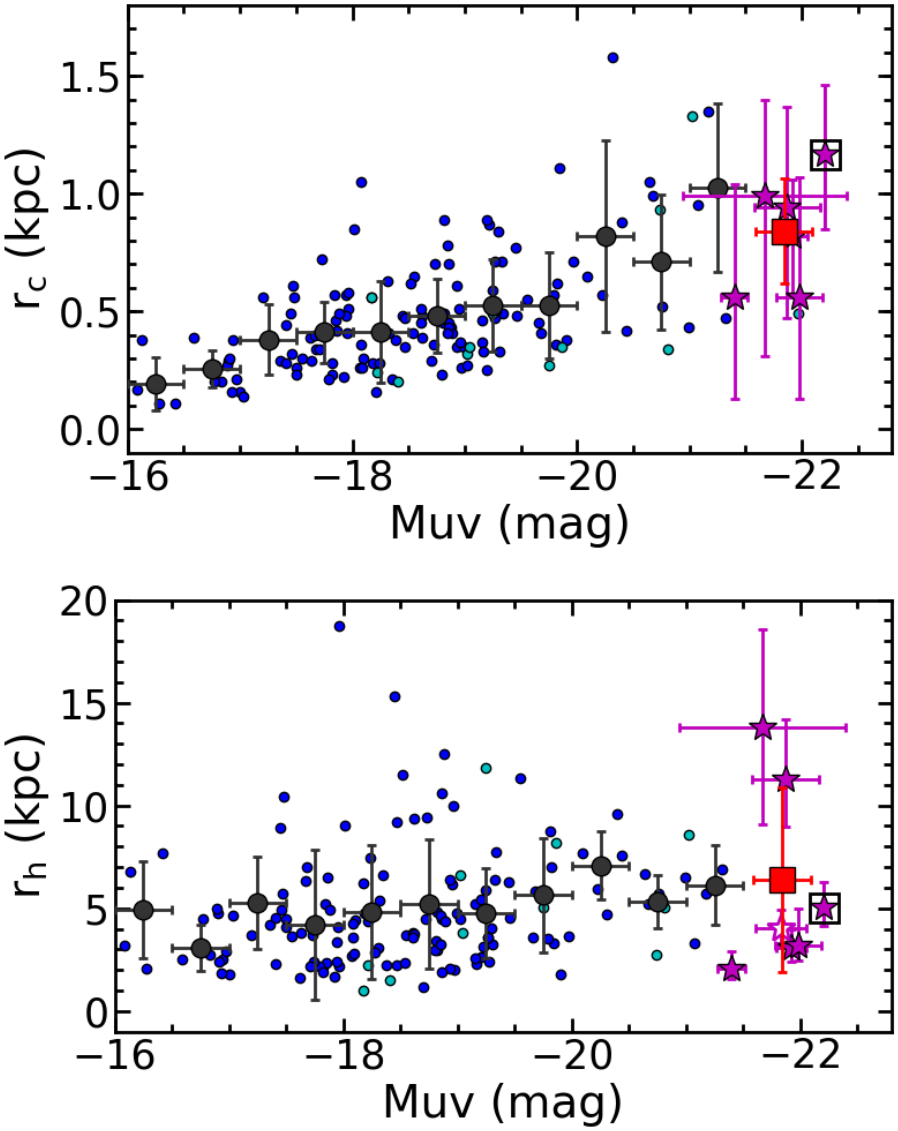

Figure 6.6 Same as Figure 6.5, but for the core scale length (top) and halo scale length (bottom) as a function of continuum magnitude.

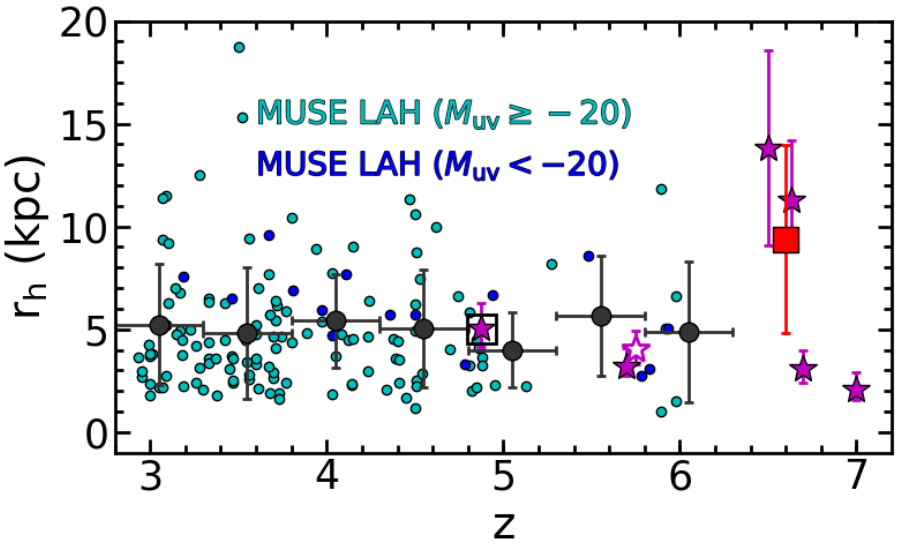

Figure 6.7 Halo scale length as a function of redshift. The MUSE LAHs with $M_{\rm UV} \geq -20$ and $M_{\rm UV} < -20$ are presented as cyan and blue filled circles, respectively. The meanings of stars and blacked filled circles are the same as Figure 6.5. We use z66-1, z66-2, and z66-3 to calculate the LAB average value at $z = 6.6$ (red filled square). The objects of z57-2, z66-1, z66-2, and z66-3 are slightly shifted along the horizontal axis by +0.05, -0.1, +0.1, and +0.03 to avoid overlaps, respectively.

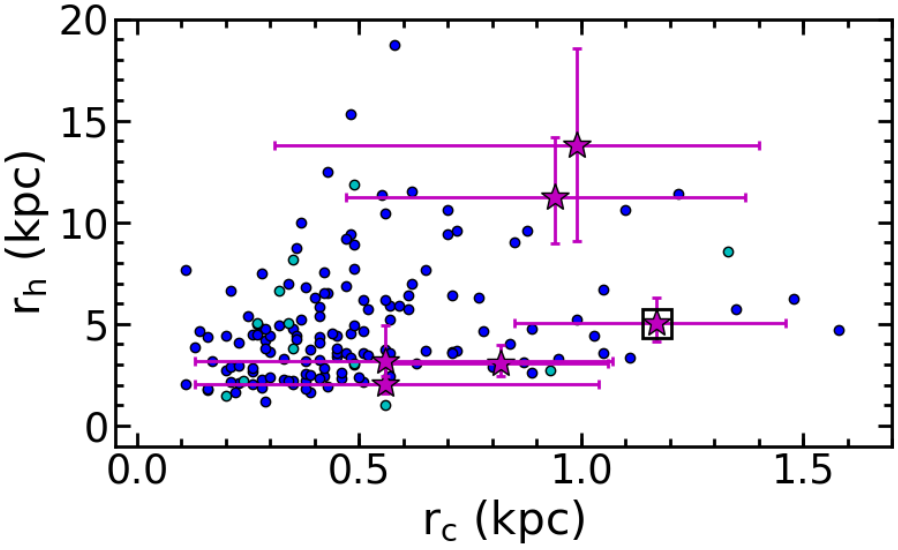

Figure 6.8 Same as Figure 6.5, but for the halo scale length as a function of core scale length.

of $\sim 10^{15}$ $M_{\odot}$ at $z = 0$ (Topping et al. 2018), and such a protocluster would have a typical size of $\sim$10 cMpc at $z \gtrsim 5$ (Chiang et al. 2013). The length of the cylinder is $\sim$ 40 cMpc, corresponds to the redshift range of LAEs selected by narrowbands.

We estimate the uncertainty of δ with the following method. We measure the uncertainty of n assuming a Poisson distribution (Gehrels 1986). Because $\bar{n}$ is an average of many measurements, the uncertainty of $\bar{n}$ is negligible. We then calculate the error propagation from n to δ.

Figure 6.9 presents the overdensity maps of LAEs at z = 4.9, 5.7, 6.6, and 7.0. The maps are made by smoothing the calculated overdensities with a Gaussian kernel whose standard deviation σ is $\sim$10 cMpc in the same manner as Harikane et al. (2019). The δ of each LAB is presented in Table 4.1. Clearly, all of the 7 LABs are located in overdense regions (δ>0), and 3 of the 7 LABs have large overdensities above the 1σ significance levels.

Figure 6.10 shows the $r_{\rm h}$ as a function of δ of our LABs. To test the correlation between the $r_{\rm h}$ and δ, we calculate the Spearman's rank correlation coefficient ρ to be 0.43 with a p-value of 0.34. We do not consider the errors of $r_{\rm h}$ and δ when calculating the ρ and p-value. Our correlation test suggests that there is no significant correlation between the $r_{\rm h}$ and δ of our LABs at $z = 4.9-7.0$. We also calculate the average values of $r_{\rm h}$ and δ in the bins of $\delta = 0-3$ and $3-6$, and do not find a significant correlation considering the error bar. On the other hand, Matsuda et al. (2012) find a positive correlation between the halo scale length and LAE overdensity of LAEs at $z = 3.1$, as shown as the blue triangles in Figure 6.10. The differece between our result and Matsuda et al. (2012) may be caused by the small size of our sample, the differences of redshifts and detection limits, and/or the different fields of our LABs. Additionally, it should be noted that Matsuda et al. (2012) use different measurement methods of halo scale length and overdensity from ours, and the different measurements may cause the different results.

6.3 AGN Activity

Because the bright Lyα luminosities ($> 10^{43.4}$ erg s^{-1}) of the 7 LABs make them possible hosts of AGNs, we investigate the AGN activities in LABs with X-ray and spectroscopic data. None of the 7 LABs have X-ray counterparts in images and catalogs of XMM/Newton and Chandra in the literature (Scoville et al. 2007; Hasinger

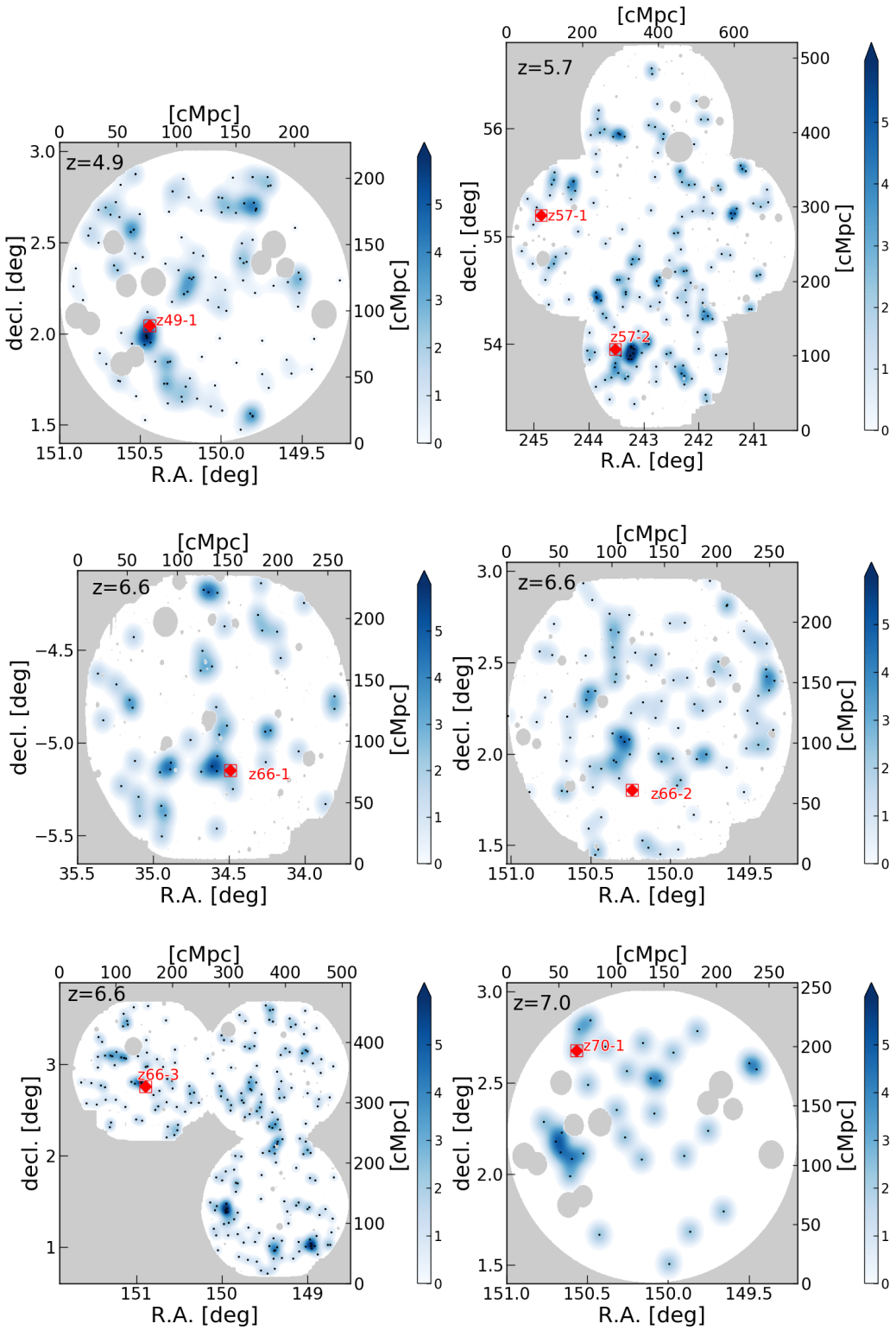

Figure 6.9 Overdensity maps of LAEs at $z = 4.9$, 5.7, 6.6, and 7.0. The red diamonds indicate our LABs, while the other LAEs are shown as black dots. The blue regions present the overdensities of LAEs. Dark blue regions have higher overdensities than light blue regions.

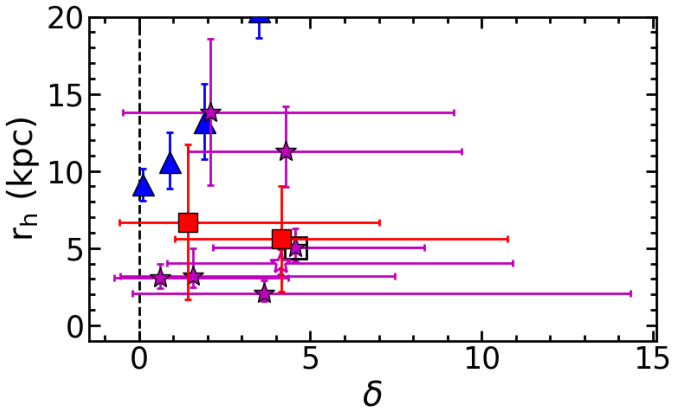

Figure 6.10 Halo scale length as a function of LAE overdensity of our LABs. The meanings of symbols are the same as those in Figure 6.5. The LAB average values are calculated in the bins of $\delta = 0 - 3$ and $3 - 6$. The horizontal error bar of the average value indicates the uncertainty calculated based on the Poisson distribution, while the vertical error bar is the root mean square. The result from Matsuda et al. (2012) is shown as blue triangles.

et al. 2007; Civano et al. 2016; Marchesi et al. 2016). The spectra of the 7 LABs do not show NV emission indicative of AGNs.

Shibuya et al. (2018) investigate 21 bright LAEs that are not broad-line AGNs at $z = 6 - 7$, and find that the LAEs have Lyα line widths of $\sim 200 - 400$ km s^{-1}. Consistently, z57-1, z66-1, z66-2, z66-3, and z70-1 also show Lyα line widths of $\sim 200 - 400$ km s^{-1} in Figure 5.5, suggesting that z57-1, z66-1, z66-2, z66-3, and z70-1 are not broad-line AGNs. On the other hand, the Lyα line widths of z49-1 and z57-2 are systematically larger than 400 km s^{-1}. Because z49-1 has a very clear continuum center that z57-2 does not show, it is possible that a hidden AGN is the origin of the relatively large Lyα line width of z49-1. The large Lyα line width of z57-2 is not likely caused by an AGN, but by mergers or dense neutral hydrogen gas in the HI region.

In Section 5.2, we show that z49-1 has a CIV emission line with a line width of 317 ± 132 km/s. The rest-frame equivalent width of the CIV emission is 8.3 ± 1.5 Å. The spectrum shows no HeII emission above the 2σ detection limit. We use the 2σ detection limit as an upper limit of the HeII flux, and find that the lower limit of the CIV to HeII ratio is ~ 1.2. We compare the CIV rest-frame equivalent width and CIV to HeII ratio with the AGN and SFG models in Nakajima et al. (2018), and find that

z49-1 can be explained by both the AGN and low-metallicity SFG models (Figure 6.11). This result indicates that z49-1 is a candidate of a high-z AGN, although the possibility of a young and low-metallicity SFG cannot be ruled out.

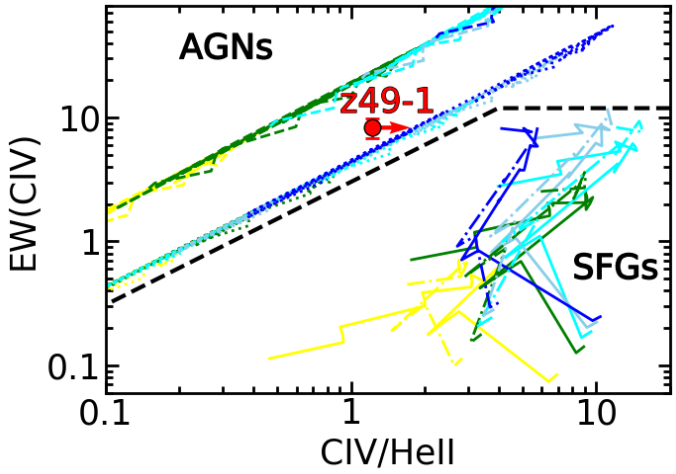

Figure 6.11 CIV equivalent width as a function of CIV/HeII ratio. The object z49-1 is represented as a red filled circle. We show two AGN models with power-law indices of $\alpha = -2.0$ (dotted line) and -1.2 (dashed line), and two SFG models of POPSTAR (solid line) and BPASS (dash-dotted line) from Nakajima et al. (2018). The ionization parameters $\log U$ of the AGN and SFG models are -2.5 (yellow), -2.0 (green), -1.5 (cyan), -1.0 (skyblue), and -0.5 (blue). The black dashed line represents the threshold that distinguishes between AGNs and SFGs.

As we discussed in Chapter 1, AGNs have been identified in all of the LAEs with bright Lyα luminosities ($\log\,(L_{\mathrm{Ly}\alpha}/[\mathrm{erg\ s^{-1}}]) \gtrsim 43.4$) at $z \sim 2-3$ in Konno et al. (2016) and Sobral et al. (2018). Similary, Overzier et al. (2013) show that at least 63% of LABs at $z \sim 2-3$ are associated with luminous AGNs. On the other hand, no AGN has been confirmed to exist in LABs at $z \gtrsim 5$ including our LABs. This may suggest that LABs at $z \gtrsim 5$ are less likely to be powered by luminous AGNs than LABs at $z \sim 2-3$.

6.4 Stellar Population

We perform SED fitting on z49-1 and z70-1 using total magnitudes measured in Subaru HSC (g, r, i, z, y, NB816, and NB921), UltraVista (Y, J, H, and K), and Spitzer/IRAC (3.6 μm and 4.5 μm bands) images. In our SED fitting, we consider

the contributions from both nebular and stellar populations. The nebular spectra (emission lines and continua) are calculated basically following Schaerer & de Barros (2009). We use the stellar population synthesis model GALAXEV (Bruzual & Charlot 2003) with Salpeter's initial mass function (Salpeter 1955) to obtain stellar SEDs. A constant star formation history is assumed. Details of our SED fitting method are discribed in Ono et al. (2010). Because the 3.6μm band is contaminated by Hα emission at $z = 4.9$, we do not use the photometry of the 3.6μm band in our SED fitting of z49-1. The best-fit SEDs of z49-1 and z70-1 are shown in Figure 6.12. The properties of the best-fit SEDs are summarized in Table 6.1.

Table 6.1 Properties of best-fit SEDs

ID	Z ($Z_\odot$)	$\log M_*$ ($M_\odot$)	$E(B-V)_*$ (mag)	log(Age) (yr)	log(SFR) ($M_\odot$ yr^{-1})
z49-1	0.004	$9.0^{+0.2}_{-0.1}$	0.05	$6.6^{+0.5}_{-1.5}$	$2.4^{+1.4}_{-0.3}$
z66-1[a]	0.2	$10.18^{+0.05}_{-0.07}$	0.15	$8.26^{+0.05}_{-0.05}$	$2.00^{+0.01}_{-0.01}$
z66-2[b]	0.005-0.2	~ 10.3	0.0-0.5	~ 8.8	~ 1.4
z70-1	0.02	< 9.1	0.10	< 7.7	$2.0^{+1.8}_{-0.8}$

Notes.
[a] best-fit SED from Ouchi et al. (2013)
[b] best-fit SED from Sobral et al. (2015)

We compare the SFRs and stellar masses of our LABs with those of main sequence SFGs at high-z, as shown in Figure 6.13. It is clear that z49-1 and z70-1 are above the main sequence, while z66-1 is nearly on the main sequence and z66-2 is under the main sequence. This suggests that our LABs have a variety of specific SFRs, and that star-burst (z49-1, z70-1) and non-star-burst (z66-2) phases exist in LABs.

6.5 Hα Emission of z49-1

The 3.6 μm image of z49-1 in Figure 4.5 shows a clear color excess that is caused by the redshifted Hα. Comparing with the best-fit SED obtained in Section 6.4, we measure the observed 3.6 μm excess that corresponds to a Hα luminosity of $(3.6 \pm 1.2) \times 10^{43}$ erg s^{-1}. Assuming the case-B recombination and no dust extinction suggested by the best-fit SED, we estimate the expected Lyα luminosity to be $(3.2 \pm 1.1) \times 10^{44}$ erg s^{-1}. The Lyα escape fraction is the observed Lyα luminosity divided by the expected Lyα

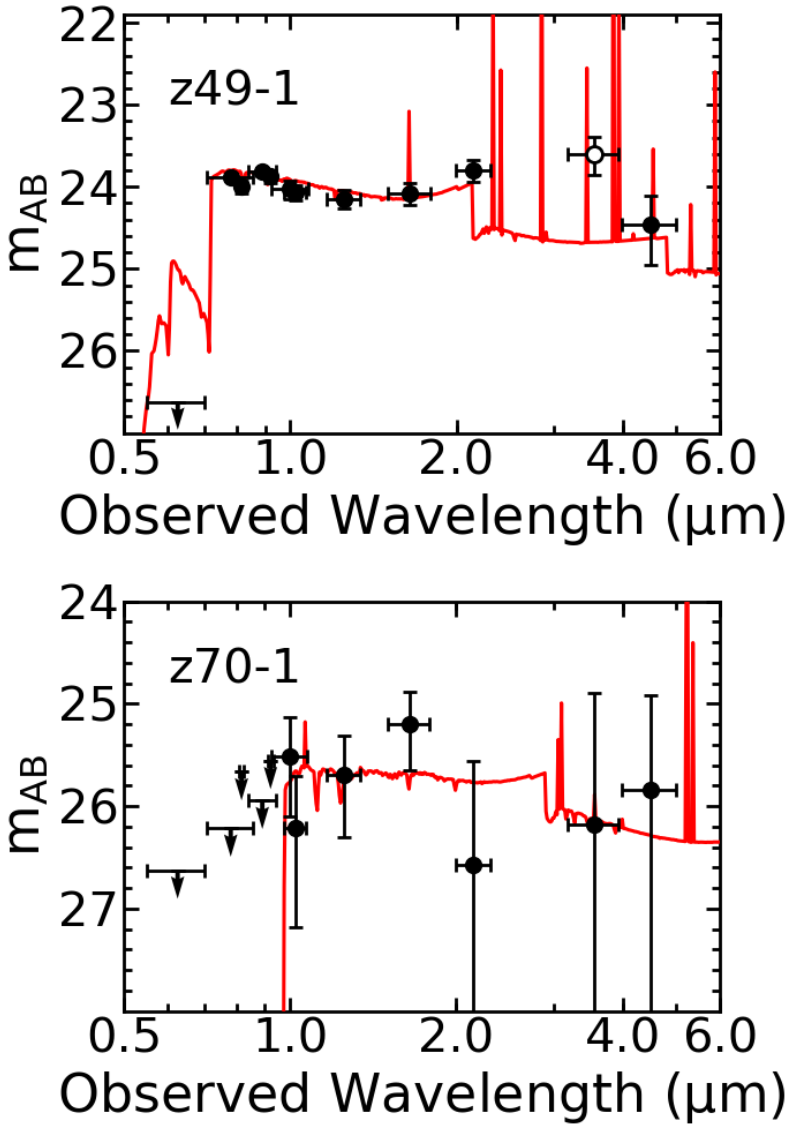

Figure 6.12 SEDs of the best-fit models of z49-1 (top) and z70-1 (bottom). The SED models are presented as the red solid curves. The black filled circles are total magnitudes measured in g, r, i, z, y, NB816, NB921, Y, J, H, K, 3.6 μm, and 4.5 μm bands. The black open circle indicates the 3.6μm band photometry that we do not use in the SED fitting of z49-1. The horizontal error bars represent the filter bandwidths. The vertical error bars show the 1σ errors in magnitude. The arrows indicate 3σ upper limits.

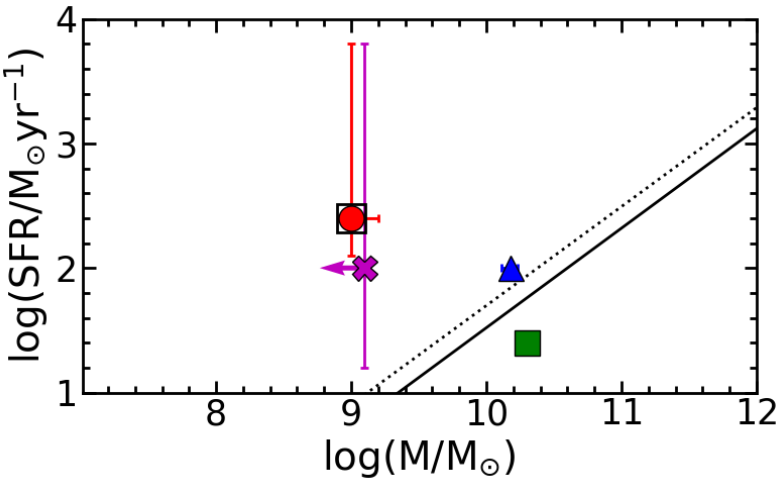

Figure 6.13 SFR as a function of stellar mass of z49-1 (red circle), z66-1 (blue triangle), z66-2 (green square), and z70-1 (magenta cross). The solid and dotted lines indicate the main sequence SFGs from Song et al. (2016) at $z \sim 5$ and 7, respectively.

luminosity, $(3.5 \times 10^{43})/(3.2 \times 10^{44})$ =0.11±0.04. It should be noted that the escape fraction of z49-1 is consistent with the fraction of ~ 0.1 found in low-z galaxies with similar stellar masses and SFRs (Hayes et al. 2014; Verhamme et al. 2017).

CHAPTER 7
DISCUSSIONS

7.1 Identification of The Most Distant LAB at $z = 7.0$

In this thesis, we have identified the most distant LAB found to date, z70-1 at $z = 7.0$. The composite pseudocolor image of z70-1 is presented in the left panel of Figure 7.1. Figure 7.2 shows the Lyα and continuum profiles of z70-1. To test whether the Lyα profile of z70-1 is more extended than the continuum profile, we fit the exponential function shown in Equation 6.3 to the Lyα and continuum profiles. In the fitting, the errors of the profiles are considered. The best-fit scale lengths of the Lyα and continuum profiles are 1.43 ± 0.18 and 0.56 ± 0.41 kpc, respectively. We estimate the statistical significance of the difference between the scale lengths of Lyα and continuum profiles assuming a normal distribution. We find that the Lyα and continuum profiles are different at the 87% confidence level. This suggests that the Lyα emission of z70-1 is more extended than the continuum. Taken together with the identification of the Lyα emission line on the spectrum, and the bright Lyα luminosity of z70-1, our result suggests that z70-1 is a real LAB at $z = 7.0$.

7.2 An Extremely Extended LAB at $z = 5.7$

The NB816 image of z57-2 suggests that z57-2 has very extended Lyα emission presenting no clear center, which is apparently different from the other 6 LABs. The composite pseudocolor image of z57-2 is shown in the right panel of Figure 7.1. Figure 7.3 displays the Lyα surface brightness profile of z57-2, together with the other 6 LABs and 2 model galaxies of Halo-11 and Halo-12 at $z \sim 6$. Halo-11 and Halo-12 are calculated by cosmological hydrodynamic and radiative transfer simulations in Yajima et al. (2017) and Arata et al. (2018) described in Section 2.4. Halo-11 and Halo-12 have halo masses of 1.6×10^{11} and 7.5×10^{11} $M_\odot$, respectively. As suggested by Behroozi et al. (2013), the halo masses of Halo-11 and Halo-12 correspond to stellar masses of $\sim 2.0 \times 10^9$ and 1.4×10^{10} $M_\odot$ at $z = 6.0$, respectively, which are consistent with the stellar masses of our LABs estimated by the SED fitting (Section 6.4). In Figure 7.3, it is clear that z57-2 has a more extended Lyα profile than the other 6 LABs. Moreover, model galaxies of Halo-11 and Halo-12 cannot explain the

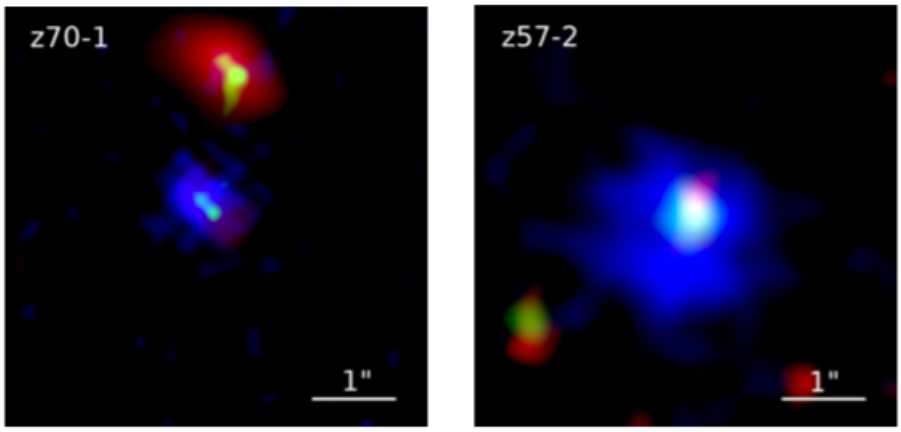

Figure 7.1 Composite pseudocolor images of z70-1 (left) and z57-2 (right). The upper object in the left panel is a foreground source. The red, green, and blue (RGB) colors of z70-1 are presented with 3.6 μm, y, and NB973 images, respectively. For z57-2, the RGB colors correspond to y, z, and NB816 images, respectively. Because z57-2 does not show a clear center in the NB816 image, we smooth the y, z, and NB816 images of z57-2 with a Gaussian kernel whose standard deviation is $0\farcs17$ before we make the pseudocolor image. The size of the images is $5'' \times 5''$. The length of $1''$ is indicated as a white bar.

extremely extended Lyα profile of z57-2.

The spectrum in Figure 5.3 shows that z57-2 has a Lyα emission line with a FWHM of $\sim$ 600 km/s that is broader than those of the other 6 LABs. It should also be noted that the Lyα line of z57-2 shows multiple peaks. These features may be caused by dynamical systems, such as multiple components or mergers. Another possibility is that z57-2 has a surrounding shell of thick HI gas that resonantly scatters Lyα photons produced at the center of this system, because the expanding shell model discussed in Section 2.3 also shows Lyα emission with broadened multiple peaks. The surrounding shell should have varying HI column densities that cause the positional dependence of the Lyα line center and line width found in Figure 5.5.

7.3 Comparisons between Our LABs and Previously Known LABs

We compare our LABs with those at $z = 2-3$ analyzed in previous studies. In Section 6.2, we show that all of our LABs are located in overdense regions with overdensities

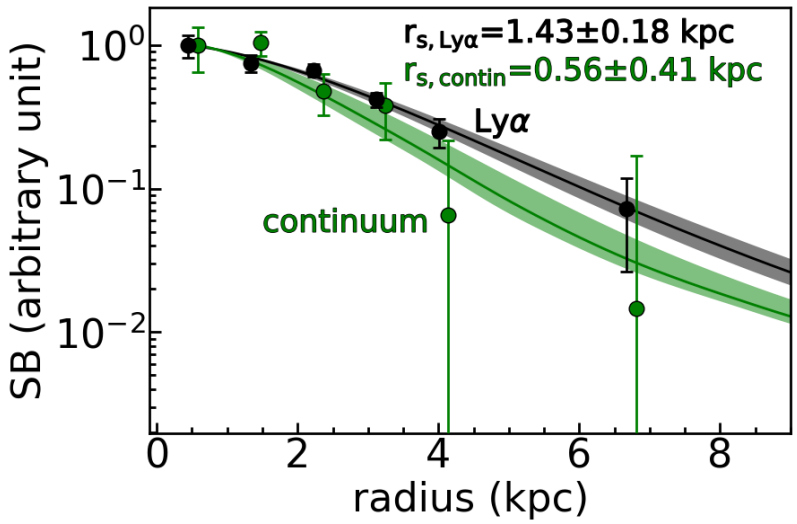

Figure 7.2 Lyα (black) and continuum (green) surface brightness profiles of z70-1. The filled circles are the profiles measured from images. The solid lines present the best-fit exponential functions. The shaded regions indicate the errors of the best-fit functions. We normalize all the profiles at the radius of ∼0.5 kpc for comparison. To avoid overlaps, the continuum profile is slightly shifted along the horizontal axis by +0.15 kpc.

above 0.3. As we introduced in Section 1.4, LABs at $z \sim 3$ also basically reside in regions with overdensities above 0.3 (Figure 1.7). This consistency suggests that LABs tend to be located in overdense regions and trace the large-scale structure regardless of redshift.

S11 perform profile fitting on LABs at $z \sim 3$ and suggest a halo scale length of $\sim$ 28 kpc that is much larger than our results ($\sim$ 7 kpc on average). Although the different profile fitting methods, LAB selection methods, and PSFs can partly explain the difference, it is likely that our LABs at $z = 5 - 7$ are less extended than LABs at $z \sim 3$. Our LABs, even for the extremely extended LAB z57-2, would show smaller isophotal areas than LABs at $z \sim 3$ if the luminosity and detection limit are the same. Our results may be explained by the picture that SFGs grow larger toward lower redshifts as expected from the hierarchical structure formation introduced in Chapter 1.

We use the 9 and 1 LAB candidates at z =4.9 and 7.0, respectively, to calculate the LAB number densities. The survey volumes are $\sim 1.5 \times 10^6$ Mpc^3 at $z = 4.9$ and $\sim 3.6 \times 10^6$ Mpc^3 at $z = 7.0$. The number densities of our LABs are $\sim 6.0 \times 10^{-6}$

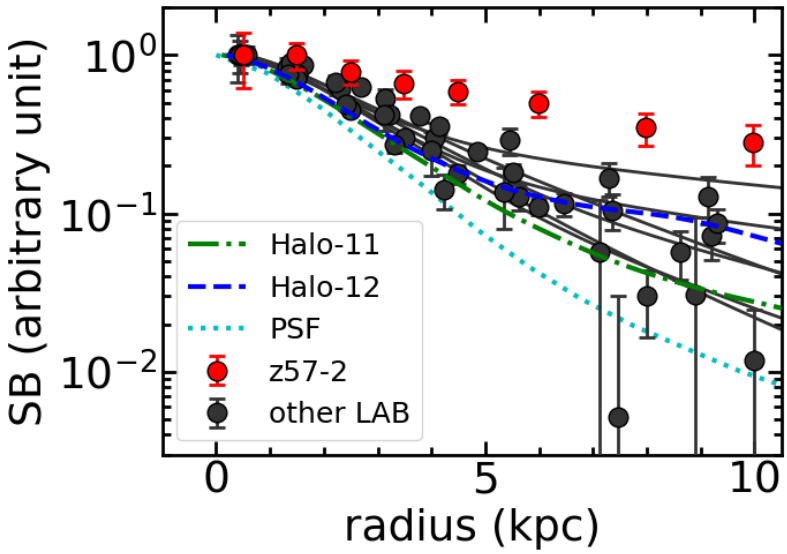

Figure 7.3 Lyα surface brightness profiles of z57-2 (red filled circles), the other 6 LABs (black filled circles), and 2 model galaxies of Halo-11 (green dash-dotted line) and Halo-12 (blue dashed line). The black solid lines are the best-fit total models of the other 6 LABs in Figures 6.3 and 6.4. The cyan dotted line represents the PSF. The profiles of Halo-11 and Halo-12 are convolved with the PSF. All the profiles are normalized at the radius of $\sim$0 kpc for comparison.

and 2.8×10^{-7} Mpc^{-3} at $z = 4.9$ and 7.0, respectively. Figure 7.4 shows the number densities of our LABs compared with those at different redshifts in the literature. We fit the number density $N(z)$ with a Madau–Lilly formula,

$$N(z) = \frac{a(1+z)^b}{1+[(1+z)/c]^d}, \tag{7.1}$$

where a, b, c, and d are free parameters (Madau, & Dickinson 2014). The best-fit parameters are $a = 6.8 \times 10^{-8}$, $b = 3.2$, $c = 5.5$, and $d = 15.2$. It should be noted that all of the results are measured nearly at a surface brightness limit of ~ 5 erg s^{-1} cm^{-2} arcsec^{-2} (Yang et al. 2010), except for the results from Matsuda et al. (2004) (~ 2 erg s^{-1} cm^{-2} arcsec^{-2}) and Shibuya et al. (2018) in the HSC deep field (~ 8 erg s^{-1} cm^{-2} arcsec^{-2}). We do not use the results from Matsuda et al. (2004) and Shibuya et al. (2018) in HSC deep field in the fitting.

In Figure 1.6, we see that the number density reaches the maximum at $z \sim 3-5$ and decreases toward low-z ($z \sim 2$) and high-z ($z \sim 7$). This redshift evolution of

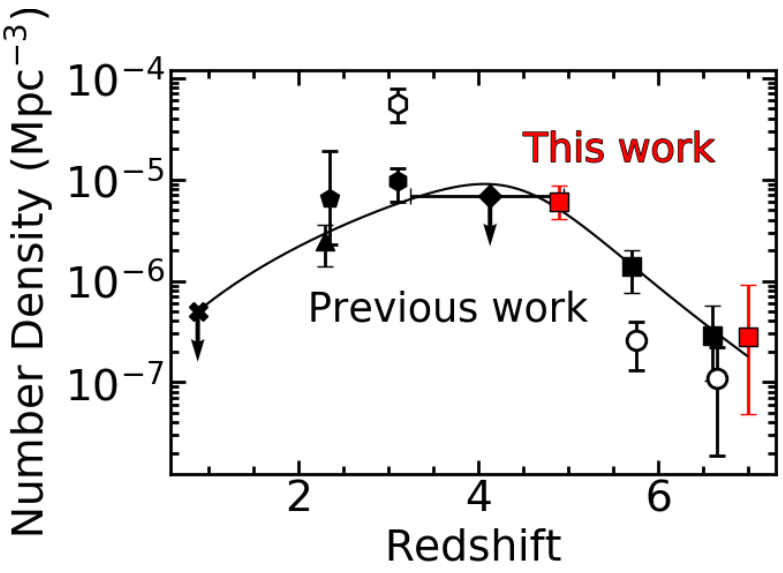

Figure 7.4 Number density of LABs as a function of redshift. The red filled squares are our LABs at $z = 4.9$ and 7.0. The red vertical error bars are calculated based on the Poisson distribution. The black symbols show results from previous studies (filled square: Shibuya et al. 2018 in the HSC ultra-deep field; open circle: Shibuya et al. 2018 in the HSC deep field; filled diamond: Saito et al. 2006; filled pentagon: Yang et al. 2010; filled triangle: Yang et al. 2009; filled cross: Keel et al. 2009). The open hexagon represent the result from Matsuda et al. (2004), while the filled hexagon is the same result but with a correction estimated by Yang et al. (2009) for the different luminosity-size limits. All the data are measured nearly at the surface brightness limit of ~ 5 erg s^{-1} cm^{-2} arcsec^{-2}, except for the open hexagon and open circles. The solid line shows the best-fit Madau−Lilly formula. We use all the data except for the open hexagon and open circles in the fitting. The filled pentagon and open circles are slightly shifted along the horizontal axis by +0.05 to avoid overlaps.

LAB number densities is consistent with the results from previous studies that suggest LABs have the highest number density at $z \sim 3$ (Yang et al. 2009, 2010; Shibuya et al. 2018). It should be noted that although LABs at $z \sim 5-7$ are selected with the same method, the selection methods of LABs at $z \sim 2-4$ are different. It is possible that the different selection methods cause an underestimation or overestimation of the LAB number density at $z \sim 2-4$ in the literature.

7.4 Comparisons between Our LABs and A Toy Model

To explain the physical origin of the extended Lyα emission around a galaxy, previous studies have discussed the possibility of Lyα resonant scattering. In the scenario of Lyα resonant scattering, the Lyα photons are emitted by star formation in the galaxy center. Although our LABs have very high Lyα luminosities, the Lyα equivalent widths are $\sim 50 - 200$ Å comparable to the Lyα equivalent width from dust-free star formation estimated in Charlot & Fall (1993). This consistency suggests that the luminous Lyα emission may be explained by resonantly scattered Lyα photons generated in the star-forming galaxy center.

We investigate the possibility of Lyα resonant scattering with a toy model suggested by S11 who apply the model to SFGs at $z \sim 3$, as we introduced in Section 2.4. We fit Equation 2.22 to the Lyα profiles of our LABs with the least-squares method. We find that $S_{\mathrm{Ly}\alpha}(b)$ is insensitive to R_{eff}, and in the fitting we fix the value of $R_{\mathrm{eff}} = 90$ kpc that is the same as S11. The fitting results are shown in Figures 7.5 and 7.6. The parameters of the best-fit models are summarized in Table 7.1. We estimate the uncertainties of the best-fit parameters with the Monte Carlo method similar to the one we discussed in Section 6.1. Clearly, each LAB has a best-fit model that is consistent with the Lyα profile within the 2σ level. This suggests that the toy model for Lyα resonant scattering may explain the extended Lyα emission around our LABs, including the extremely extended LAB z57-2. However, this does not mean that resonant scattering is the only one solution of the extended Lyα emission. It should be noted that this model is based on some assumptions: the spherical symmetry, constant outflow velocity, and covering fraction as a function of radius.

Table 7.1 Parameters of the best-fit toy models

ID	r_0 (kpc)	γ
z49-1	$1.56^{+0.03}_{-0.03}$	$1.22^{+0.08}_{-0.07}$
z57-1	$1.32^{+0.08}_{-0.08}$	$1.18^{+0.12}_{-0.08}$
z57-2	$1.50^{+0.15}_{-0.18}$	$0.59^{+0.12}_{-0.11}$
z66-1	$1.03^{+0.29}_{-0.57}$	$0.44^{+0.16}_{-0.21}$
z66-2	$1.29^{+0.05}_{-0.08}$	$1.00^{+0.08}_{-0.10}$
z66-3	$0.83^{+0.36}_{-0.66}$	$0.67^{+0.30}_{-0.29}$
z70-1	$1.41^{+0.02}_{-0.09}$	$1.43^{+0.24}_{-0.25}$

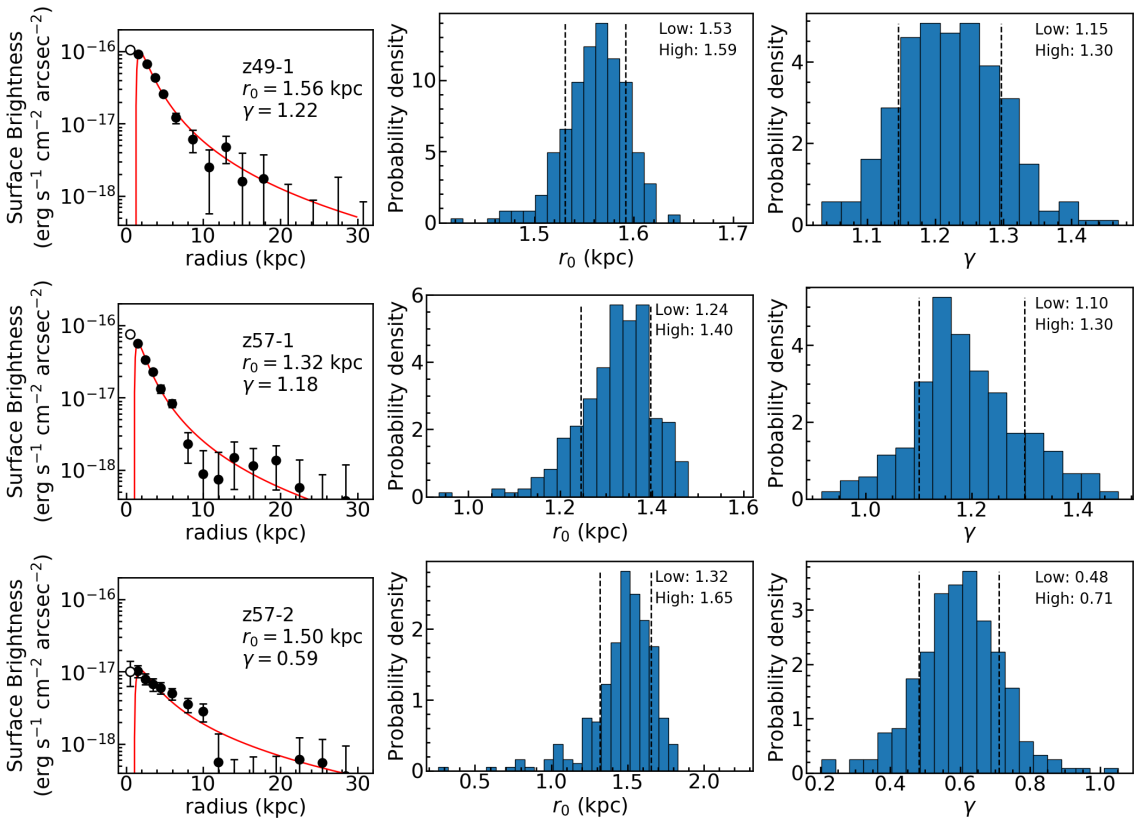

Figure 7.5 Best-fit toy models (first column), uncertainties of r_0 (second column), and uncertainties of γ (third column) for z49-1 (top), z57-1 (middle), and z57-2 (bottom). In the first column, the black filled circles show the Lyα profile. The red solid lines represent the best-fit toy models. We do not use the Lyα profile within a radius of 1 kpc (empty circle) in the fitting, because of the "hole" in the model where $f_c > 1$. In the second and third columns, the dashed lines indicate the ranges of the central 68.3% confidence levels.

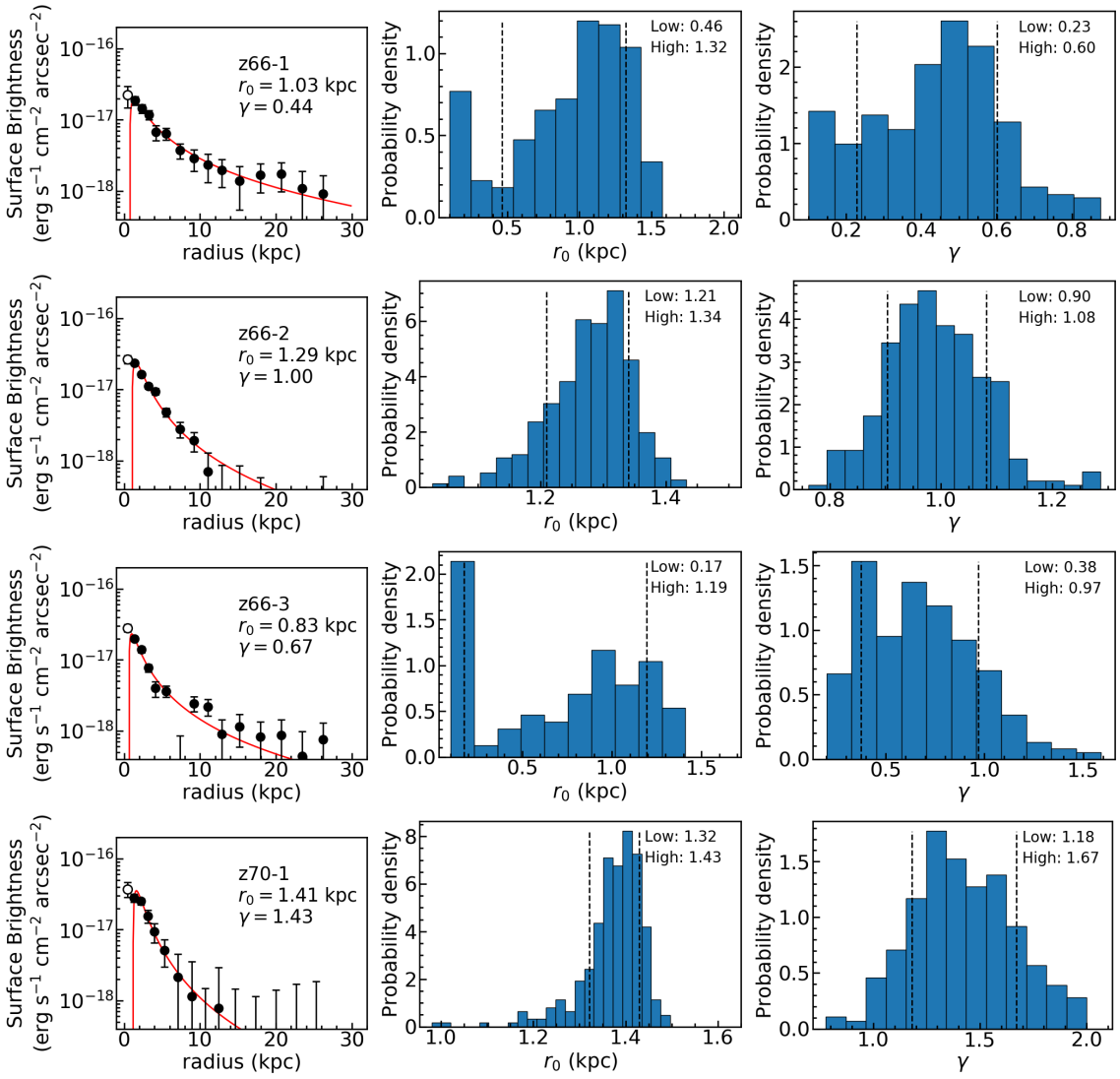

Figure 7.6 Same as Figure 7.5, but for z66-1 (first row), z66-2 (second row), z66-3 (third row), and z70-1 (last row).

The uncertainty contours of the best-fit parameters of our LABs are presented in Figure 7.7. The average r_0 and γ of our LABs are 1.2 kpc and 0.9, respectively. Clearly, the r_0 correlates with the amplitude of f_c. With a given γ, a large r_0 corresponds to a large f_c that indicates thick circumgalactic gas with large V_{out} suggested by the positive correlation between f_c and V_{out} (S10). Our LABs show smaller r_0 values than the $z \sim 3$ SFGs whose best-fit r_0 is 2.2 kpc (S11). This suggests that our LABs have thinner circumgalactic HI gas and/or smaller gas outflow velocities than the SFGs with the same γ at $z \sim 3$, if we assume that the extended Lyα profiles of LABs and SFGs are mainly caused by resonant scattering. As for the γ, the γ determines the slope of f_c, and a smaller γ corresponds to a more extended distribution of f_c. Our LABs show γ values greater than SFGs at $z \sim 3$ whose best-fit γ is 0.6 considering the 1σ error. The large γ may be explained by that the f_c distribution of HI gas around our LABs are more compact than the SFGs at $z \sim 3$.

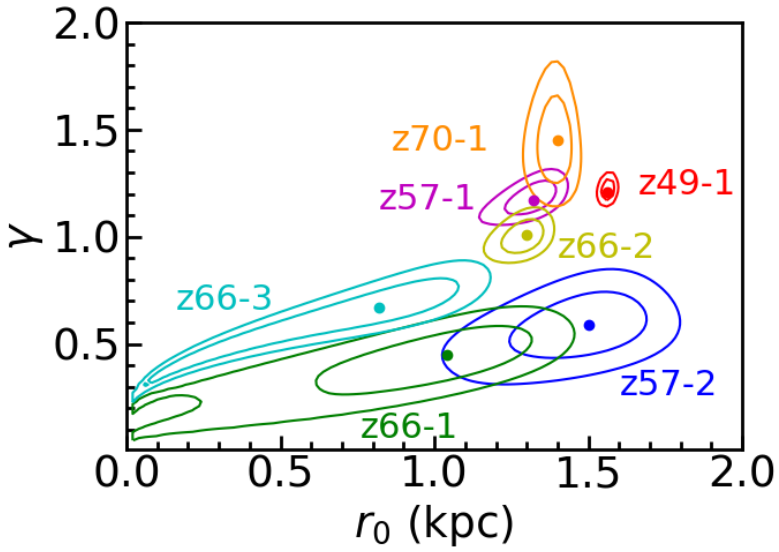

Figure 7.7 Uncertainty contours of the best-fit toy models of the 7 LABs. The contours correspond to the 68.3% and 95.5% confidence levels.

Although the toy model for resonant scattering may explain the extended Lyα profiles of our LABs, we cannot rule out the possibilities of the other scenarios including fluorescence, gravitational cooling radiation, outflows, and satellite galaxies. Similarly, with cosmological hydrodynamic and radiative transfer simulations, Zheng et al. (2011) argue that Lyα resonant scattering is likely the main contributor, but the

possibilities of other sources including fluorescence and cooling radiation cannot be ruled out (see also Verhamme et al. 2012; Dijkstra, & Kramer 2012). It is challenging to pinpoint the physical origin of the extended Lyα emission with current models. This problem may be solved by models with improved treatments of Lyα radiative transfer processes developed in the future.

CHAPTER 8
SUMMARY AND CONCLUSION

8.1 Summary of This Thesis

In this thesis, we investigate the photometric and spectroscopic properties of seven LABs; two LABs at $z = 4.888$ (z49-1) and $z = 6.965$ (z70-1) identified by us, and five previously known LABs at $z = 5.7 - 6.6$ (z57-1, z57-2, z66-1, z66-2, and z66-3). Our results are summarized below.

1. We find that z70-1 has spatially extended Lyα emission with a scale length of 1.4 ± 0.2 kpc that is about three times larger than the UV continuum. The object of z70-1 is the most distant LAB identified to date.

2. We show that z57-2 has Lyα emission that is much more extended than the other 6 LABs. The extremely extended Lyα emission of z57-2 cannot be explained by the current cosmological hydrodynamic and radiative transfer simulations.

3. We measure the core and halo scale lengths of the Lyα profiles of our LABs, and do not find strong evidences supporting that LAHs and LABs are distinct populations. We show that the relations between the scale lengths and galaxy properties ($L_{\mathrm{Ly}\alpha}$, EW_0, and M_{UV}) of our LABs are similar to those of MUSE LAHs identified by Leclercq et al. (2017). This suggests that our LABs and MUSE LAHs may have similar connections between the extended Lyα emission and host galaxies, although our LABs are more massive than typical MUSE LAHs.

4. We investigate the large scale structure around our LABs by measuring the LAE overdensity. We find that all of the 7 LABs are located in overdense regions, and 3 of the 7 LABs have large overdensities above the 1σ significance levels. Our LABs show no significant correlation between the halo scale length and LAE overdensity.

5. The 7 LABs except z49-1 exhibit no AGN signatures such as X-ray emission, N$\textsc{v}\lambda$1240, or Lyα line broadening. The object of z49-1 has a strong C$\textsc{iv}\lambda$1548 emission line that suggests an AGN. We compare the C$\textsc{iv}$ equivalent width

and CIV/HeII ratio of z49-1 with the AGN and SFG models in Nakajima et al. (2018), and find that z49-1 is an AGN candidate although the possibility of a young and low-metallicity SFG cannot be ruled out.

6. We find that the Lyα emission lines of our LABs show velocity and line-width gradients on the spectra in the small scale of 5 kpc. The gradients may be caused by dynamical systems (e.g. mergers) or a surrounding cloud of thick HI gas with varying column densities.

7. We estimate the SFRs and stellar masses of z49-1 and z70-1 with our SED fitting. Our LABs show a variety of specific SFRs, suggesting that star-burst and non-star-burst phases exist in LABs.

8. We find that the LAB number density reaches the maximum at $z \sim 3-5$, and decreases toward low-z ($z \sim 2$) and high-z ($z \sim 7$), although the LAB number densities at $z \sim 2-4$ in the literature may be overestimated or underestimated due to the different LAB selection methods.

8.2 Conclusion

In this thesis, we study the spatially extended hydrogen Lyα emission around LABs at $z = 4.9 - 7.0$. Using the imaging data obtained from our deep and wide-field survey, we have identified 2 new LABs including the most distant LAB at $z = 6.965$ found to date, which allows us to probe the earliest epoch of LAB formation. We statistically study a total of 7 high-z LABs including the 2 new LABs, and find no strong evidence supporting that our LABs and previously known LAHs are distinct populations. We investigate the large-scale structure around our LABs by calculating the LAE overdensity, and show that all of the 7 LABs are located in overdense regions. With SED fitting, we show that the LABs have a variety of specific SFRs suggesting the existence of star-burst and non-star-burst phases in LABs. Our results above suggest that our high-z LABs are typically young massive SFGs with star-burst and non-star-burst phases whose extended Lyα emission shows no distinct difference from that of high-z LAHs, and preferably reside in overdense environments.

8.3 Future Prospects

In this thesis, we have selected 9 LAB candidates at $z = 4.9$, but only the brightest one (z49-1) has been confirmed by our spectroscopy. Our next step is to carry out the follow-up spectroscopy of the other LAB candidates for confirmation and analysis. With a larger number of confirmed LABs, the statistical uncertainty of our analysis (e.g. Figure 6.10) will be smaller, and correlations such as the $r_{\rm h}$-δ relation may be revealed.

As we explained in Section 7.4, although the toy model for Lyα resonant scattering model may explain our LABs, the possibilities of the other scenarios cannot be ruled out. To solve this problem, Hα observations, which will be made available with the coming James Webb Space Telescope (JWST), will be very helpful. This is because Hα emission is non-resonant, and traces ionized hydrogen gas that is accompanied with photoionizaion but not gravitational cooling radiation. On the other hand, cosmological hydrodynamic and radiative transfer models with improved treatments of Lyα radiative transfer processes will likely be available in the future, and will help us understand the mechanism of extended Lyα emission around LABs at high-z.

CHAPTER 9
APPENDIX

Table 9.1: Photometric Properties of The $z = 4.9$ LAE candidates

ID	R.A.	Decl.	$i_{\rm tot}$ (1)	NB718$_{\rm ap}$ (2)	NB718$_{\rm tot}$ (3)	$L_{{\rm Ly}\alpha}$ (4)
HSC-z49LAE1	09:59:31.2	+01:28:30.8	26.00	24.90	24.67	5.99
HSC-z49LAE2	09:57:45.5	+01:48:21.6	24.94	24.21	23.85	11.29
HSC-z49LAE3	09:57:45.5	+01:48:21.6	25.33	24.24	24.19	8.59
HSC-z49LAE4	09:57:42.3	+01:58:18.2	25.54	24.94	24.84	3.42
HSC-z49LAE5	09:57:32.0	+02:03:22.2	26.13	24.18	24.24	10.31
HSC-z49LAE6	09:57:03.7	+02:17:38.6	26.06	24.56	24.42	8.31
HSC-z49LAE7	10:03:38.9	+02:15:40.4	25.84	24.89	25.01	3.30
HSC-z49LAE8	10:03:00.4	+01:53:36.9	25.58	24.80	24.73	4.37
HSC-z49LAE9	10:03:24.8	+02:11:08.1	>27.40	23.95	23.95	15.75
HSC-z49LAE10	10:03:35.6	+02:21:34.3	26.60	24.45	24.28	10.73
HSC-z49LAE11	10:03:02.2	+02:30:05.8	25.61	24.91	25.05	2.41
HSC-z49LAE12	10:03:17.1	+02:32:16.6	25.74	24.94	24.54	6.34
HSC-z49LAE13	10:03:14.6	+02:34:37.2	25.02	24.68	24.47	3.99
HSC-z49LAE14	10:03:02.1	+02:40:47.1	25.74	24.56	24.65	5.42
HSC-z49LAE15	10:02:30.0	+01:44:31.5	25.49	24.56	24.16	9.53
HSC-z49LAE16	10:02:32.7	+01:44:33.5	25.59	24.72	24.37	7.49
HSC-z49LAE17	10:02:50.2	+01:50:03.7	25.01	24.71	24.42	4.41
HSC-z49LAE18	10:02:44.1	+01:50:52.8	26.53	24.64	24.43	9.03
HSC-z49LAE19	10:02:12.6	+01:56:51.8	25.98	25.01	24.89	4.38
HSC-z49LAE20	10:02:28.0	+02:00:26.2	26.22	24.24	24.17	11.41
HSC-z49LAE21	10:02:33.7	+02:20:55.1	25.79	24.53	24.14	10.75
HSC-z49LAE22	10:02:08.2	+02:26:33.7	25.92	24.70	24.46	7.60
HSC-z49LAE23	10:02:33.7	+02:20:55.1	25.79	24.54	24.14	10.73
HSC-z49LAE24	10:02:39.1	+02:22:36.6	26.13	24.37	24.37	8.94
HSC-z49LAE25	10:02:14.1	+02:33:27.7	24.86	24.18	24.06	7.68
HSC-z49LAE26	10:02:09.8	+02:34:15.7	25.32	24.34	24.02	10.78

HSC-z49LAE27	10:02:30.6	+02:38:26.2	25.31	24.34	24.33	6.90
HSC-z49LAE28	10:02:44.3	+02:39:13.3	25.69	24.91	24.88	3.64
HSC-z49LAE29	10:02:14.1	+02:33:27.7	24.89	24.19	24.08	7.61
HSC-z49LAE30	10:02:09.8	+02:34:15.7	25.30	24.34	23.93	12.01
HSC-z49LAE31	10:02:51.0	+02:41:37.7	24.74	24.55	24.22	4.85
HSC-z49LAE32	10:02:07.4	+02:52:29.9	24.51	23.96	23.76	9.72
HSC-z49LAE33	10:02:36.2	+02:43:15.6	25.60	24.89	25.13	1.95
HSC-z49LAE34	10:02:29.1	+02:48:57.7	25.56	24.27	24.22	9.03
HSC-z49LAE35	10:02:07.4	+02:52:29.9	24.51	23.96	23.76	9.70
HSC-z49LAE36	10:01:52.8	+01:31:37.5	26.60	24.85	24.66	7.07
HSC-z49LAE37	10:02:05.8	+01:39:35.5	26.47	24.64	24.39	9.28
HSC-z49LAE38	10:01:24.4	+01:43:38.0	25.31	24.84	24.64	4.00
HSC-z49LAE39	10:01:38.2	+01:50:50.6	27.04	24.96	24.74	7.00
HSC-z49LAE40	10:01:56.1	+01:50:39.2	26.17	24.66	24.30	9.74
HSC-z49LAE41	10:02:03.0	+01:54:36.1	25.92	23.78	23.71	17.69
HSC-z49LAE42	10:01:53.8	+01:56:25.7	24.97	24.45	24.08	8.20
HSC-z49LAE43	10:01:50.7	+01:59:23.3	25.56	24.82	24.76	4.07
HSC-z49LAE44[a]	10:01:46.0	+02:02:44.3	23.89	22.90	22.66	36.60
HSC-z49LAE45	10:01:45.1	+01:57:12.4	24.99	24.52	24.46	3.97
HSC-z49LAE46	10:01:50.3	+01:58:50.3	26.53	25.02	24.66	7.01
HSC-z49LAE47	10:01:50.7	+01:59:23.3	25.59	24.86	24.81	3.81
HSC-z49LAE48	10:01:50.9	+01:59:35.1	26.23	24.86	24.86	5.06
HSC-z49LAE49	10:01:45.5	+02:03:14.2	25.47	24.09	23.93	12.65
HSC-z49LAE50	10:01:49.1	+02:07:09.4	25.93	24.82	24.65	5.92
HSC-z49LAE51	10:01:58.4	+02:16:33.3	26.85	24.91	24.69	7.17
HSC-z49LAE52	10:01:22.3	+02:23:05.8	26.25	24.68	24.43	8.61
HSC-z49LAE53	10:01:56.2	+02:25:22.0	24.96	23.96	23.59	16.34
HSC-z49LAE54	10:02:00.8	+02:39:31.3	26.15	24.82	24.71	5.99
HSC-z49LAE55	10:01:19.8	+01:43:32.7	>27.40	25.02	24.81	6.71
HSC-z49LAE56	10:01:19.4	+01:37:09.2	25.10	23.31	23.22	26.53
HSC-z49LAE57	10:00:57.8	+01:37:43.7	27.08	24.94	24.67	7.52
HSC-z49LAE58	10:00:58.4	+01:39:13.8	26.22	24.56	24.49	7.90
HSC-z49LAE59	10:00:52.8	+01:42:42.5	26.22	24.32	24.18	11.21
HSC-z49LAE60	10:01:19.8	+01:43:32.8	>27.40	25.05	24.83	6.63

HSC-z49LAE61	10:00:46.7	+01:45:22.3	26.27	25.01	24.56	7.40
HSC-z49LAE62	10:01:19.5	+01:50:45.6	26.12	24.57	24.52	7.45
HSC-z49LAE63	10:01:15.8	+01:50:55.9	24.66	23.78	23.38	19.30
HSC-z49LAE64	10:01:19.5	+01:50:45.6	26.13	24.57	24.53	7.42
HSC-z49LAE65	10:00:55.4	+02:13:09.2	25.95	24.05	23.98	13.37
HSC-z49LAE66	10:00:46.8	+02:18:29.6	24.82	24.07	24.07	7.38
HSC-z49LAE67	10:01:12.6	+02:10:34.8	25.81	24.98	24.54	6.52
HSC-z49LAE68	10:00:55.4	+02:13:09.2	25.96	24.05	23.98	13.37
HSC-z49LAE69	10:00:49.9	+02:13:58.4	26.72	24.93	24.69	7.00
HSC-z49LAE70	10:00:43.5	+02:18:00.1	26.19	24.99	24.81	5.31
HSC-z49LAE71	10:00:40.9	+02:18:30.7	24.51	23.82	23.46	16.11
HSC-z49LAE72	10:00:41.1	+02:26:37.3	25.52	24.48	24.48	6.18
HSC-z49LAE73	10:01:03.4	+02:21:02.7	26.03	24.86	24.65	6.23
HSC-z49LAE74	10:00:58.4	+02:31:49.2	25.35	24.71	24.59	4.60
HSC-z49LAE75	10:01:17.0	+02:40:18.2	26.19	24.38	24.34	9.39
HSC-z49LAE76	10:01:12.0	+02:46:49.6	25.68	24.49	24.26	9.03
HSC-z49LAE77	10:00:55.8	+02:50:57.2	25.88	24.52	24.32	8.94
HSC-z49LAE78	10:00:47.9	+02:44:55.0	25.90	24.75	24.70	5.46
HSC-z49LAE79	10:01:12.0	+02:46:49.6	25.75	24.50	24.32	8.54
HSC-z49LAE80	09:59:58.9	+01:34:48.6	25.99	24.63	24.35	8.81
HSC-z49LAE81	10:00:15.3	+01:36:16.4	24.83	24.30	24.18	6.01
HSC-z49LAE82	10:00:15.3	+01:36:16.4	24.85	24.30	24.20	5.82
HSC-z49LAE83	10:00:35.6	+01:38:43.3	25.13	24.56	24.37	5.58
HSC-z49LAE84	10:00:09.0	+01:42:58.9	26.20	25.07	25.04	3.94
HSC-z49LAE85	10:00:28.2	+01:52:30.1	26.87	24.68	24.48	8.97
HSC-z49LAE86	10:00:02.1	+01:58:35.0	26.25	25.06	24.66	6.57
HSC-z49LAE87	10:00:04.2	+02:08:45.7	24.95	24.39	24.29	5.40
HSC-z49LAE88	10:00:19.9	+02:11:08.5	26.89	25.05	24.79	6.44
HSC-z49LAE89	09:59:54.0	+02:14:25.3	26.20	24.97	25.00	4.15
HSC-z49LAE90	10:00:07.9	+02:18:39.8	25.76	24.96	24.95	3.46
HSC-z49LAE91	10:00:27.2	+02:25:41.2	26.50	25.06	25.13	3.95
HSC-z49LAE92	09:59:59.0	+02:39:55.2	25.98	24.72	24.56	6.81
HSC-z49LAE93	10:00:29.7	+02:40:41.7	26.27	24.96	24.88	5.00
HSC-z49LAE94	10:00:04.0	+02:44:53.4	26.29	24.80	24.50	7.96

HSC-z49LAE95	09:59:58.9	+02:44:42.5	25.20	24.46	24.59	3.94
HSC-z49LAE96	09:59:13.1	+01:33:04.7	25.95	24.91	24.89	4.30
HSC-z49LAE97	09:59:13.0	+01:32:54.7	24.71	23.27	22.92	34.23
HSC-z49LAE98	09:59:13.1	+01:33:04.7	25.96	24.91	24.90	4.29
HSC-z49LAE99	09:59:17.3	+01:33:52.4	25.80	24.78	24.43	7.52
HSC-z49LAE100	09:59:37.4	+01:50:29.6	25.49	24.56	24.65	4.63
HSC-z49LAE101	09:59:52.0	+02:07:33.0	25.38	24.62	24.44	6.02
HSC-z49LAE102	09:59:52.0	+02:07:33.0	25.45	24.62	24.48	5.93
HSC-z49LAE103	09:59:09.6	+02:13:29.2	26.41	24.73	24.41	9.07
HSC-z49LAE104	09:59:27.4	+02:17:32.8	27.12	25.02	24.81	6.52
HSC-z49LAE105	09:59:29.3	+02:29:50.1	25.42	24.87	24.71	3.89
HSC-z49LAE106	09:59:21.9	+02:23:39.3	25.75	24.79	24.55	6.34
HSC-z49LAE107	09:59:26.4	+02:23:25.1	26.06	24.49	24.44	8.11
HSC-z49LAE108	09:59:31.7	+02:24:49.5	24.69	23.67	23.49	16.79
HSC-z49LAE109	09:59:07.6	+02:41:08.4	24.66	24.25	23.86	9.37
HSC-z49LAE110	09:59:13.4	+02:30:56.7	26.31	24.55	24.55	7.57
HSC-z49LAE111	09:59:38.4	+02:39:55.0	26.06	24.76	24.52	7.33
HSC-z49LAE112	09:59:09.0	+02:40:41.7	24.82	23.51	23.42	19.36
HSC-z49LAE113	09:59:07.6	+02:41:08.4	24.71	24.25	23.90	9.07
HSC-z49LAE114	09:59:49.9	+02:41:31.0	25.61	24.27	24.17	9.87
HSC-z49LAE115	09:59:26.2	+02:42:55.1	25.29	24.59	24.46	5.50
HSC-z49LAE116	09:59:11.7	+02:43:09.2	26.77	25.04	24.85	5.93
HSC-z49LAE117	09:59:13.6	+02:51:42.2	24.89	24.08	23.75	12.78
HSC-z49LAE118	09:59:26.2	+02:42:55.1	25.39	24.60	24.54	5.15
HSC-z49LAE119	09:59:42.3	+02:51:27.3	26.12	25.00	24.85	4.96
HSC-z49LAE120	09:59:13.6	+02:51:42.2	25.38	24.09	23.97	11.71
HSC-z49LAE121	09:58:49.0	+01:42:18.6	24.45	24.12	23.68	10.73
HSC-z49LAE122	09:58:59.2	+01:46:47.4	24.77	24.60	24.28	4.41
HSC-z49LAE123	09:58:59.0	+01:57:50.9	26.29	24.53	24.23	10.72
HSC-z49LAE124	09:58:42.0	+02:15:48.5	25.90	24.27	24.09	11.72
HSC-z49LAE125	09:58:48.1	+02:27:59.1	25.93	24.72	24.32	9.04
HSC-z49LAE126	09:58:27.6	+02:27:33.5	25.25	24.74	24.71	3.20
HSC-z49LAE127	09:59:03.8	+02:27:34.2	26.04	24.95	24.90	4.41
HSC-z49LAE128	09:58:50.5	+02:48:44.5	25.22	23.79	23.78	14.17

HSC-z49LAE129	09:58:46.9	+02:48:56.4	25.52	24.75	24.45	6.44
HSC-z49LAE130	09:58:51.0	+02:51:36.6	25.22	24.73	24.85	2.03
HSC-z49LAE131	09:58:15.8	+01:46:56.3	24.87	24.15	23.70	13.70
HSC-z49LAE132	09:58:15.8	+01:46:56.3	24.93	24.15	23.74	13.17
HSC-z49LAE133	09:58:22.6	+01:51:32.3	26.29	25.07	25.02	4.20
HSC-z49LAE134	09:58:02.5	+02:18:05.0	25.85	24.21	24.07	11.77
HSC-z49LAE135	09:58:06.1	+02:09:02.5	25.37	24.28	23.98	11.46
HSC-z49LAE136	09:58:04.3	+02:13:29.3	25.53	24.70	24.64	4.84
HSC-z49LAE137	09:58:20.9	+02:16:58.6	25.41	24.07	23.90	12.98
HSC-z49LAE138	09:58:02.5	+02:18:05.0	25.84	24.23	24.07	11.79
HSC-z49LAE139	09:58:05.3	+02:20:15.4	26.40	24.78	24.51	8.05
HSC-z49LAE140	09:58:15.8	+02:23:46.5	25.62	24.76	24.87	3.47
HSC-z49LAE141	09:58:10.7	+02:34:51.1	26.16	24.90	24.54	7.42

Notes.

Column 1: total i-band magnitude in unit of mag.

Column 2: aperture NB718 magnitude in a $2''.0$ diameter in unit of mag.

Column 3: total NB718 magnitude in unit of mag.

Column 4: Lyα luminosity in unit of 10^{42} erg/s.

[a] selected as the LAB z49-1.

Table 9.2: Photometric Properties of The $z = 7.0$ LAE candidates

ID	R.A.	Decl.	$y_{\rm tot}$ (1)	NB973$_{\rm ap}$ (2)	NB973$_{\rm tot}$ (3)	$L_{{\rm Ly}\alpha}$ (4)
HSC-z7LAE1[a]	10:02:15.5	+02:40:33.4	25.09	23.52	23.40	29.81
HSC-z7LAE2	10:02:23.4	+02:05:05.1	25.63	23.92	23.68	24.12
HSC-z7LAE3	10:02:06.0	+02:06:46.2	25.04	24.09	23.77	39.32
HSC-z7LAE4	10:01:41.9	+01:40:03.6	25.59	24.51	24.10	14.86
HSC-z7LAE5	10:00:20.3	+02:20:04.2	26.40	24.31	24.11	16.94
HSC-z7LAE6	10:03:04.4	+02:17:15.1	25.69	24.38	24.12	14.81
HSC-z7LAE7	10:01:55.9	+02:50:33.6	26.38	24.32	24.20	15.33
HSC-z7LAE8	09:59:27.6	+01:41:01.3	25.37	24.46	24.25	11.46
HSC-z7LAE9	10:01:01.4	+02:33:51.2	26.16	24.46	24.28	13.68
HSC-z7LAE10	10:01:16.9	+02:21:04.2	26.28	24.52	24.29	13.75
HSC-z7LAE11	10:02:25.3	+01:59:23.2	> 26.85	24.8	24.37	13.32
HSC-z7LAE12	09:59:00.7	+02:14:18.4	> 26.85	24.54	24.39	12.99
HSC-z7LAE13	09:57:59.4	+02:36:32.4	> 26.85	24.76	24.40	12.86
HSC-z7LAE14	10:01:32.9	+02:41:55.6	26.07	24.67	24.42	11.54
HSC-z7LAE15	10:01:59.4	+02:29:30.4	26.40	24.56	24.44	12.01
HSC-z7LAE16	10:02:56.5	+02:17:22.6	> 26.85	24.62	24.44	8.33
HSC-z7LAE17	10:00:12.9	+02:30:47.1	26.02	24.72	24.46	10.81
HSC-z7LAE18	09:58:38.3	+01:47:49.6	> 26.85	24.86	24.47	12.04
HSC-z7LAE19	09:59:58.7	+01:30:33.4	26.06	24.7	24.49	10.60
HSC-z7LAE20	10:02:12.0	+02:47:40.6	25.76	24.63	24.51	9.42
HSC-z7LAE21	09:57:49.1	+02:34:36.4	> 26.85	24.84	24.52	11.39
HSC-z7LAE22	10:02:47.1	+02:10:40.1	26.84	24.80	24.52	11.35
HSC-z7LAE23	10:01:04.5	+02:12:09.2	26.51	24.85	24.53	11.09
HSC-z7LAE24	10:02:37.8	+02:13:39.2	26.50	24.79	24.56	10.64
HSC-z7LAE25	10:01:53.5	+02:04:59.6	25.74	24.96	24.75	24.55
HSC-z7LAE26	10:00:26.0	+02:31:39.0	26.56	24.77	24.62	10.08
HSC-z7LAE27	09:59:17.1	+02:47:02.5	26.10	24.95	24.62	9.12
HSC-z7LAE28	09:59:36.4	+02:06:05.5	26.78	24.91	24.68	9.63
HSC-z7LAE29	10:00:39.2	+02:04:56.9	26.02	24.93	24.68	8.36

HSC-z7LAE30	09:59:52.6	+02:40:01.8	> 26.85	24.84	24.71	9.27
HSC-z7LAE31	10:02:39.4	+02:07:12.1	26.71	24.86	24.78	8.60
HSC-z7LAE32	10:00:37.4	+02:43:14.7	> 26.85	24.94	24.85	7.97
HSC-z7LAE33	02:17:59.5	−05:14:07.4	25.47	24.26	24.00	18.00
HSC-z7LAE34	02:16:20.1	−05:07:01.2	> 26.65	24.39	24.16	16.75

Notes.

All data in this table are taken from Itoh et al. (2018).

Column 1: total y-band magnitude in unit of mag.

Column 2: aperture NB973 magnitude in a $2\farcs0$ diameter in unit of mag.

Column 3: total NB973 magnitude in unit of mag.

Column 4: Lyα luminosity in unit of 10^{42} erg/s.

[a] selected as the LAB z70-1.

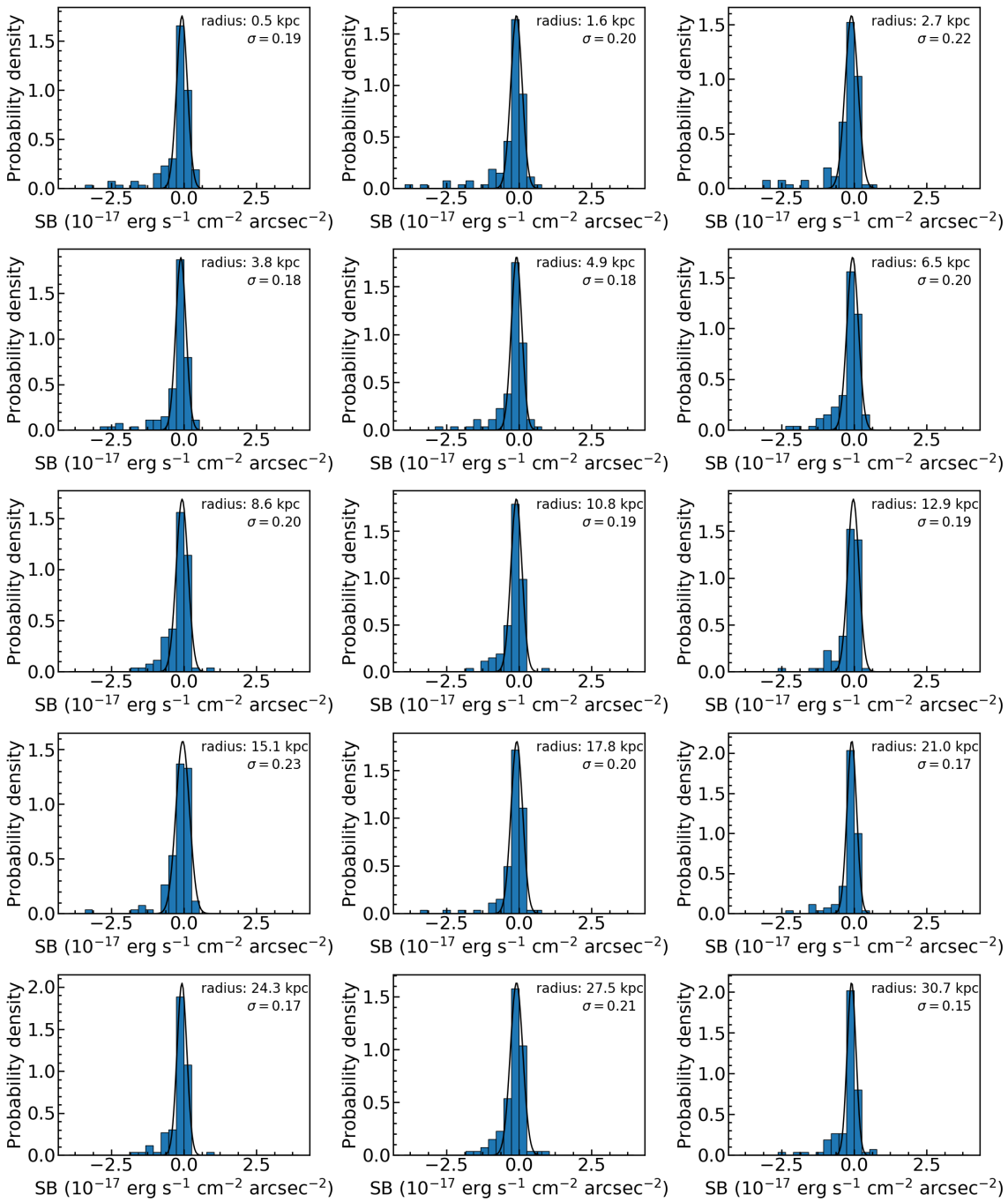

Figure 9.1 Uncertainties of the Lyα profile of z49-1 at different radii. The black solid line represents the best-fit Gaussian function. The best-fit σ is shown in each panel.

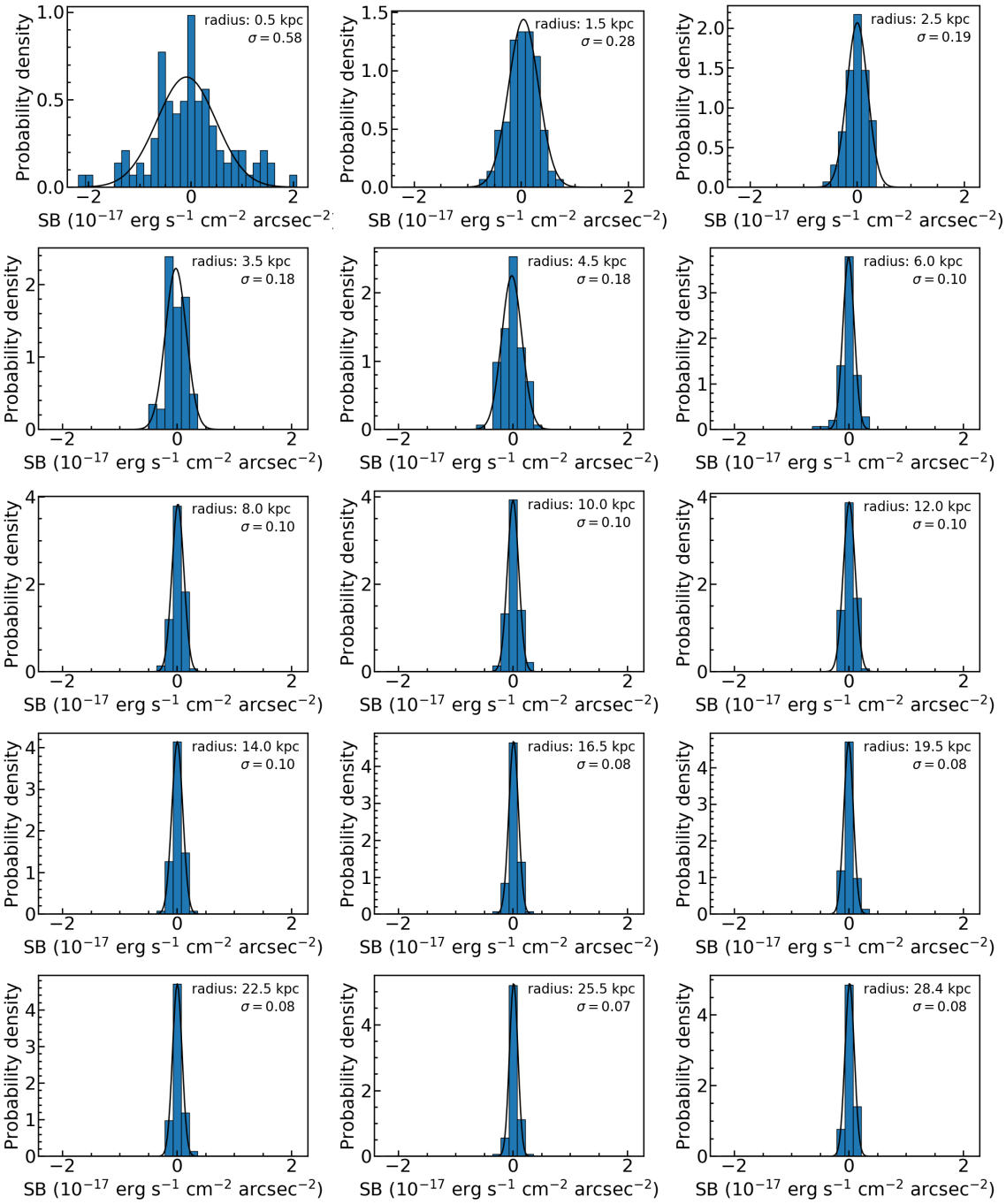

Figure 9.2 Same as Figure 9.1, but for z57-1.

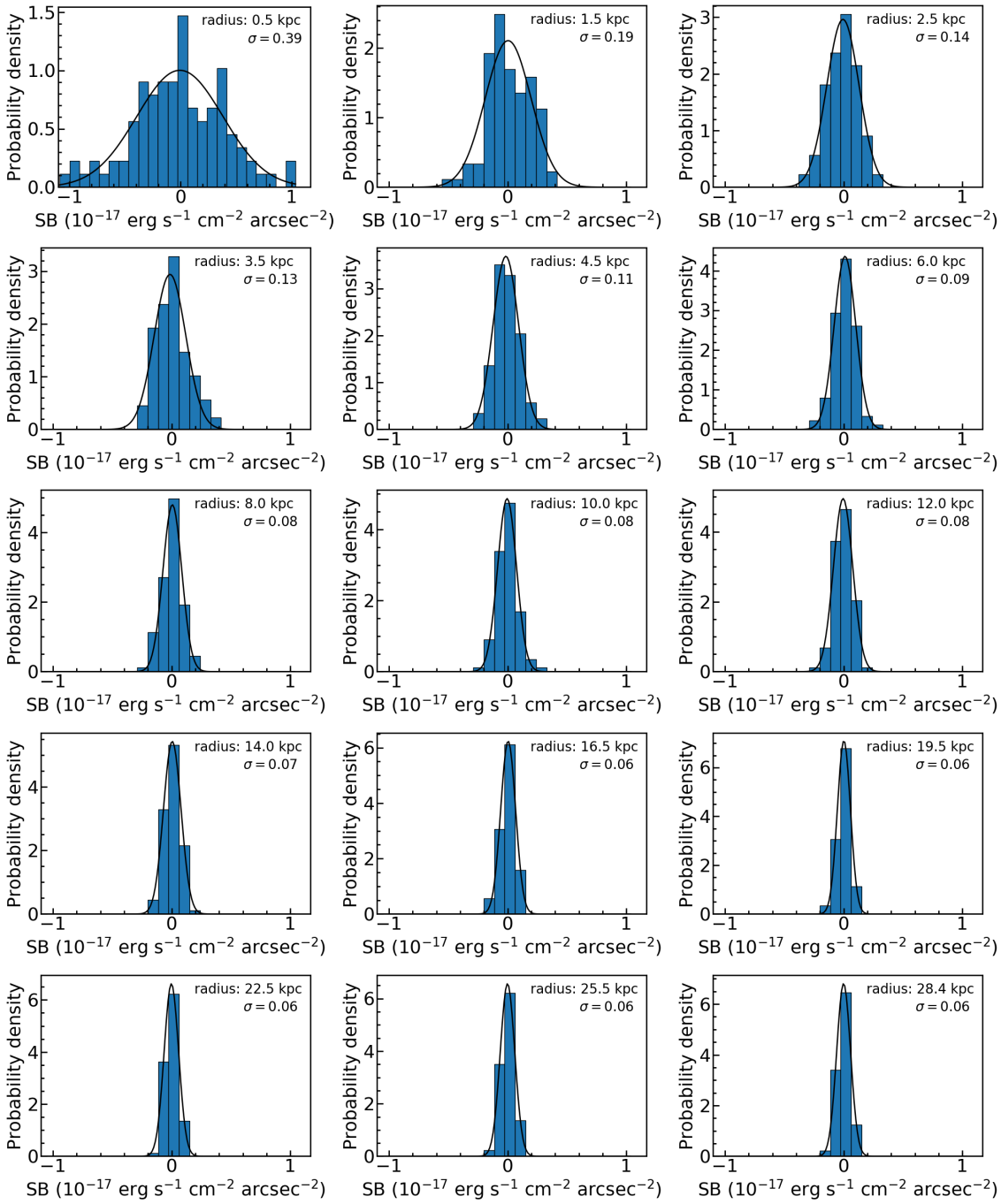

Figure 9.3 Same as Figure 9.1, but for z57-2.

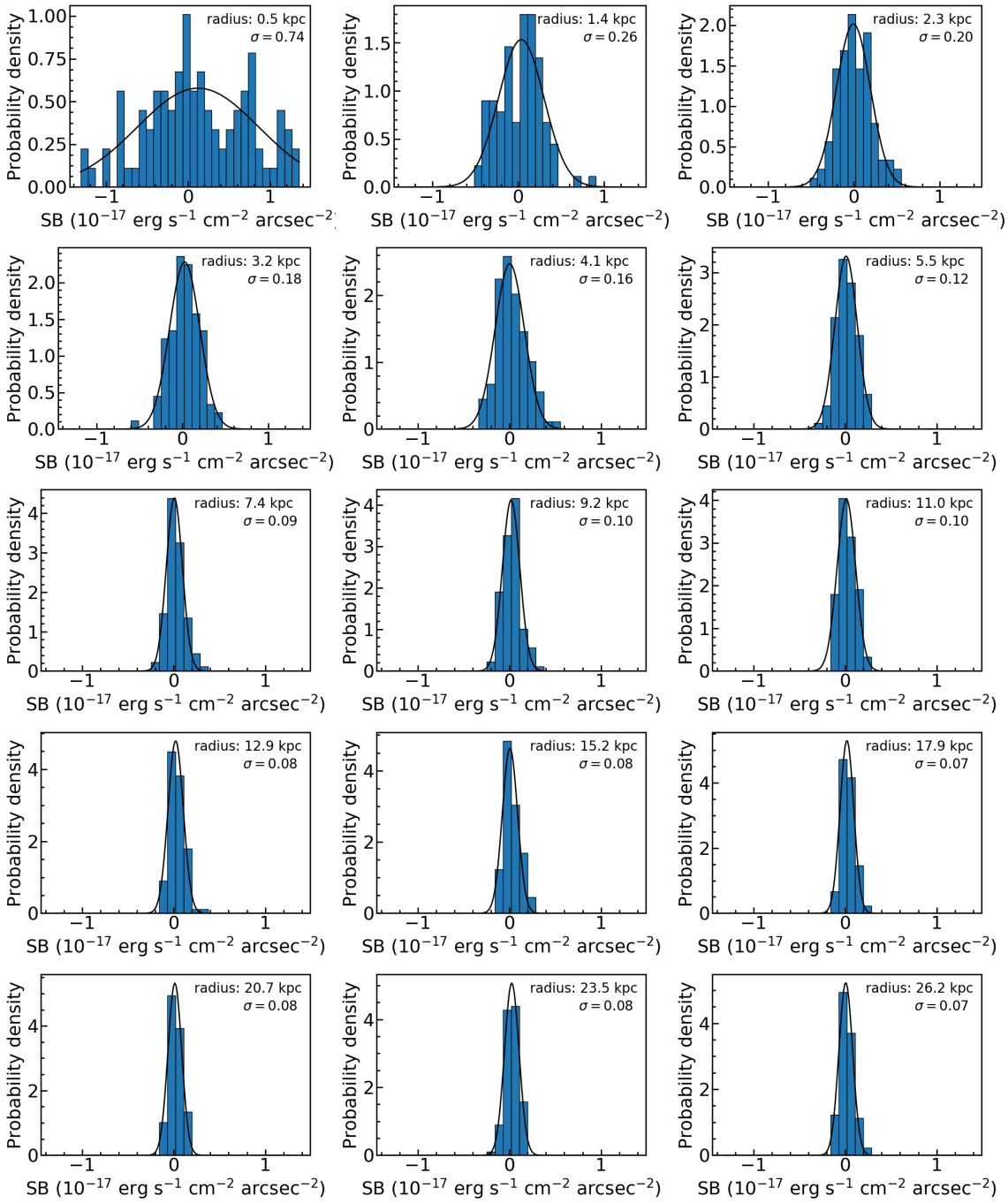

Figure 9.4 Same as Figure 9.1, but for z66-1.

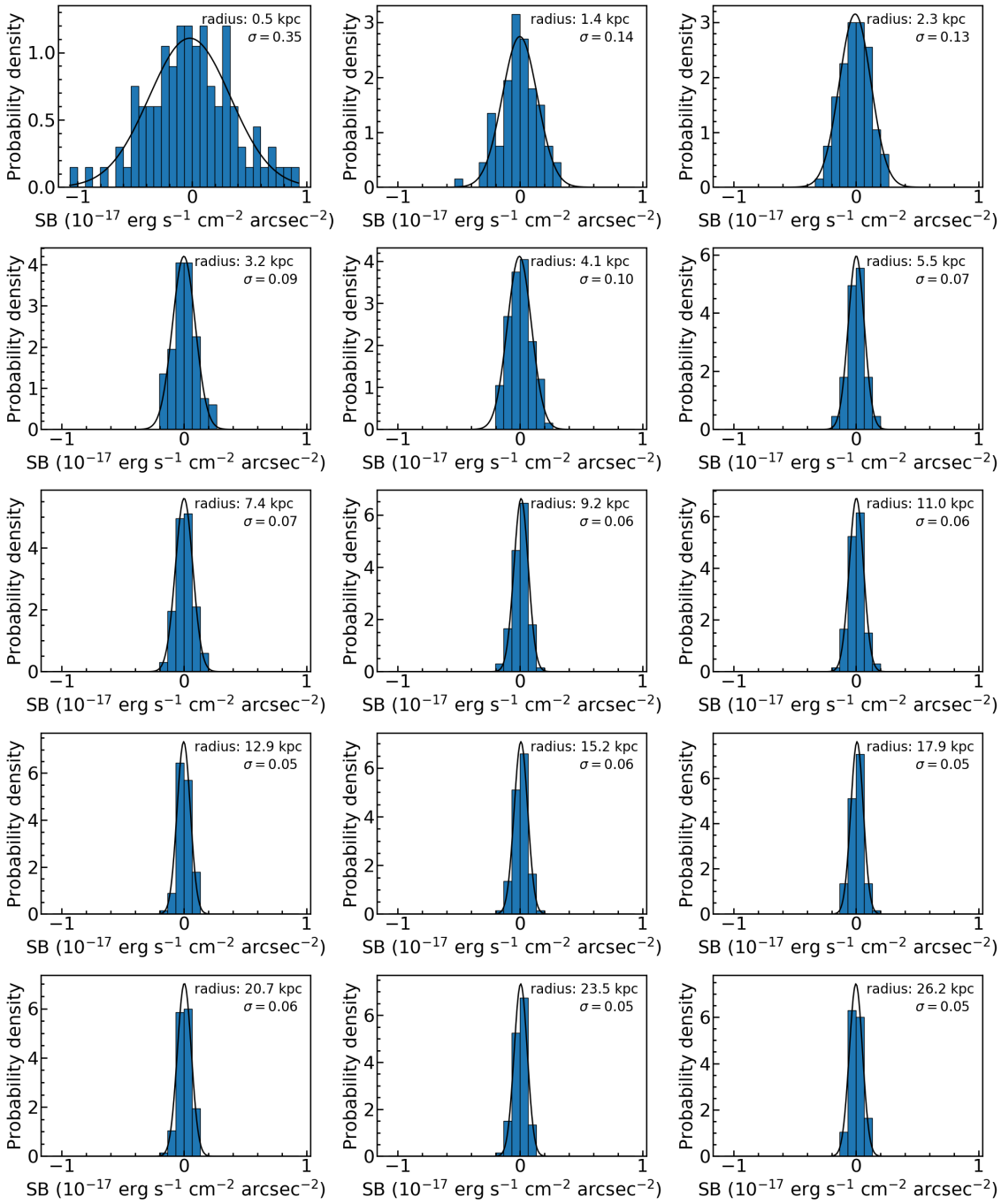

Figure 9.5 Same as Figure 9.1, but for z66-2.

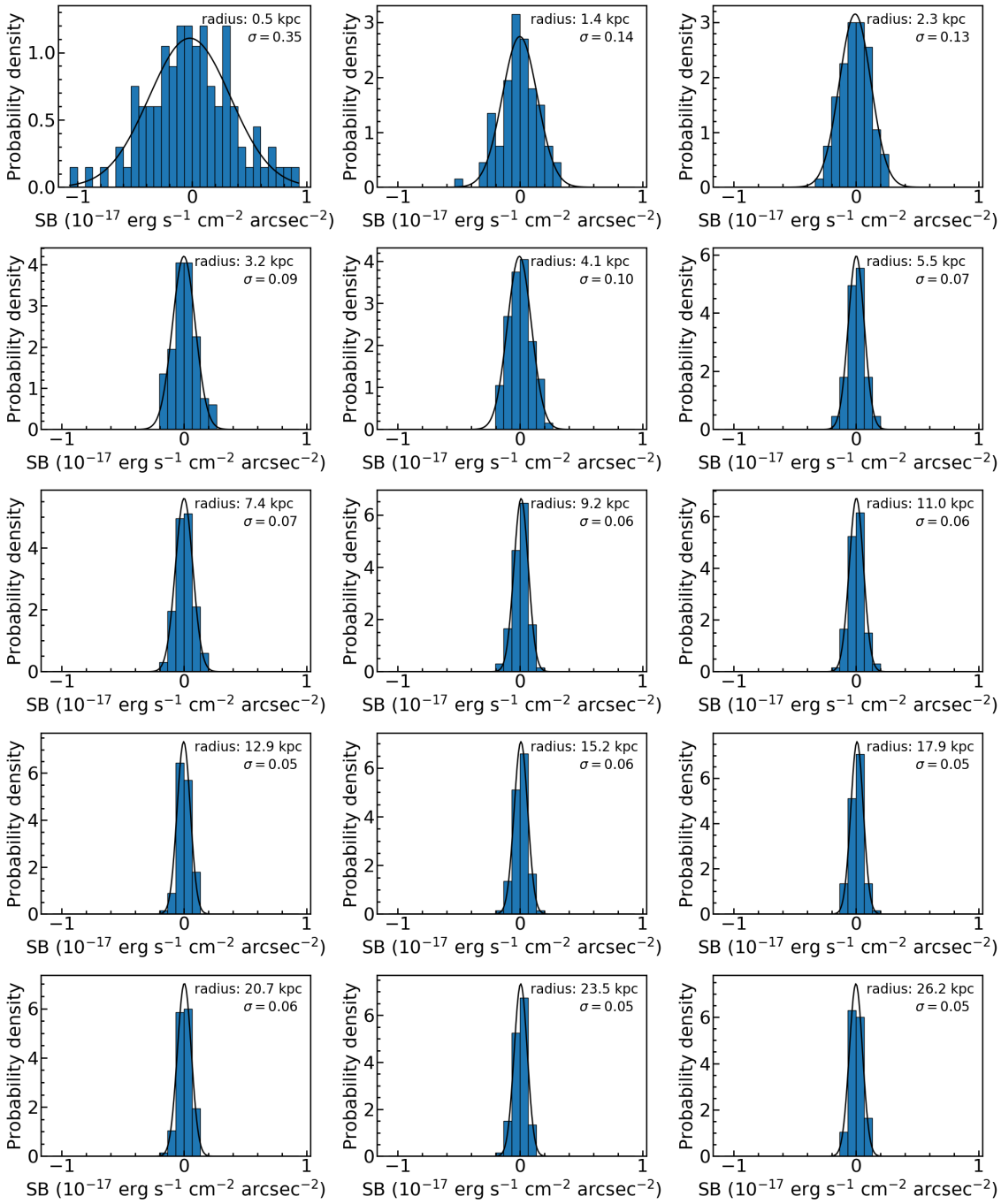

Figure 9.6 Same as Figure 9.1, but for z66-3.

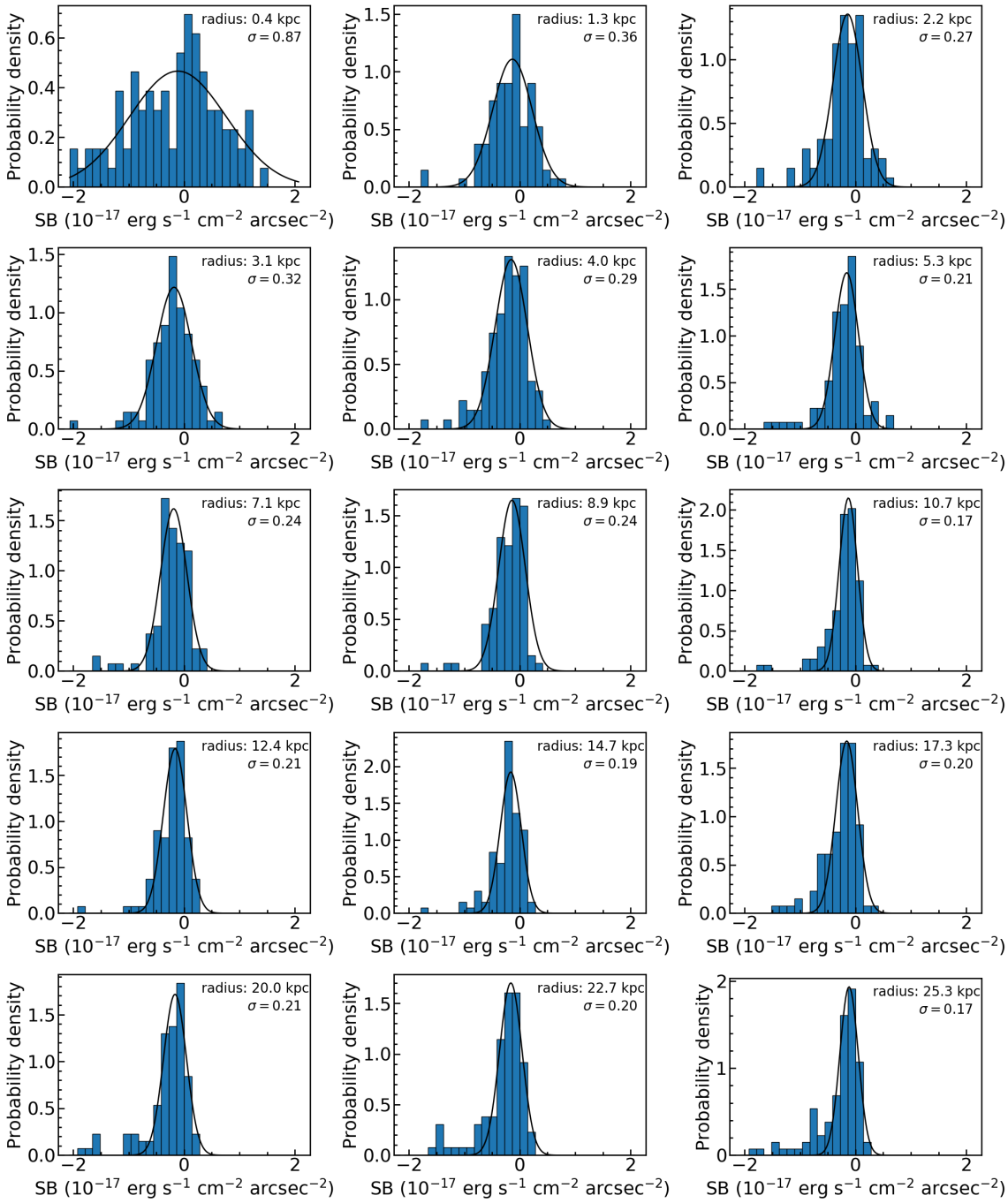

Figure 9.7 Same as Figure 9.1, but for z70-1.

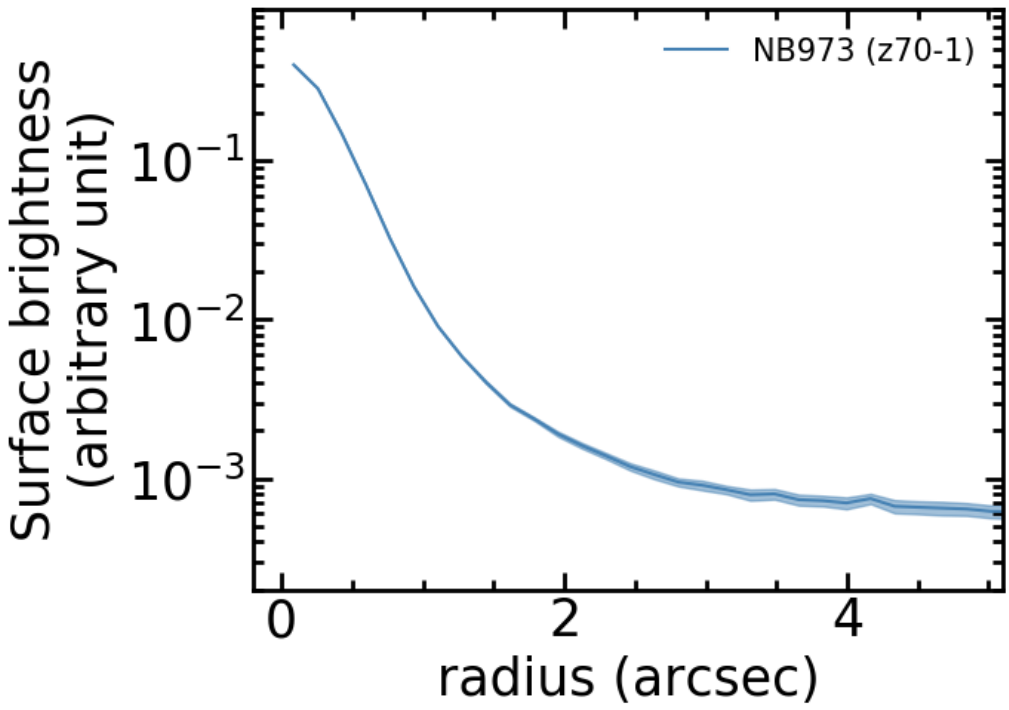

Figure 9.8 PSF of the NB973 image extracted around z70-1. The shaded region shows the uncertainty of the PSF.

REFERENCES

Aihara, H., Arimoto, N., Armstrong, R., et al. 2018, PASJ, 70, S4

Aniano, G., Draine, B. T., Gordon, K. D., & Sandstrom, K. 2011, PASP, 123, 1218

Arata, S., Yajima, H., Nagamine, K., Li, Y., & Khochfar, S. 2018, arXiv:1810.07621

Astier, P., Guy, J., Regnault, N., et al. 2006, A&A, 447, 31

Axelrod, T., Kantor, J., Lupton, R. H., & Pierfederici, F. 2010, Proc. SPIE, 7740, 774015

Bahcall, N. A., Ostriker, J. P., Perlmutter, S., et al. 1999, Science, 284, 1481

Basu-Zych, A., & Scharf, C. 2004, ApJ, 615, L85

Behroozi, P. S., Wechsler, R. H., & Conroy, C. 2013, ApJ, 770, 57

Bennett, C. L., Larson, D., Weiland, J. L., et al. 2013, ApJS, 208, 20

Bond, N. A., Gawiser, E., Guaita, L., et al. 2012, ApJ, 753, 95

Bosch, J., Armstrong, R., Bickerton, S., et al. 2018, PASJ, 70, S5

Bouwens, R. J., Illingworth, G. D., Blakeslee, J. P., et al. 2004, ApJ, 611, L1

Bruzual, G., & Charlot, S. 2003, MNRAS, 344, 1000

Cen, R., & Zheng, Z. 2013, ApJ, 775, 112

Chabrier, G. 2003, PASP, 115, 763

Charlot, S., & Fall, S. M. 1993, ApJ, 415, 580

Chiang, Y.-K., Overzier, R., & Gebhardt, K. 2013, ApJ, 779, 127

Chung, A., van Gorkom, J. H., Kenney, J. D. P., et al. 2009, AJ, 138, 1741

Civano, F., Marchesi, S., Comastri, A., et al. 2016, ApJ, 819, 62

Cole, S., Percival, W. J., Peacock, J. A., et al. 2005, MNRAS, 362, 505

Coupon, J., Czakon, N., Bosch, J., et al. 2018, PASJ, 70, S7

Dekel, A., Sari, R., & Ceverino, D. 2009, ApJ, 703, 785

Dijkstra, M., Haiman, Z., & Spaans, M. 2006, ApJ, 649, 14

Dijkstra, M., & Kramer, R. 2012, MNRAS, 424, 1672

Erb, D. K., Bogosavljević, M., & Steidel, C. C. 2011, ApJ, 740, L31

Erb, D. K., Steidel, C. C., & Chen, Y. 2018, ApJ, 862, L10

Faber, S. M., Phillips, A. C., Kibrick, R. I., et al. 2003, Proc. SPIE, 4841, 1657

Fardal, M. A., Katz, N., Gardner, J. P., et al. 2001, ApJ, 562, 605

Ferguson, H. C., Dickinson, M., Giavalisco, M., et al. 2004, ApJ, 600, L107

Feldmeier, J. J., Hagen, A., Ciardullo, R., et al. 2013, ApJ, 776, 75

Finkelstein, S. L., Papovich, C., Dickinson, M., et al. 2013, Nature, 502, 524

Francis, P. J., Woodgate, B. E., Warren, S. J., et al. 1996, ApJ, 457, 490

Francis, P. J., Williger, G. M., Collins, N. R., et al. 2001, ApJ, 554, 1001

Freedman, W. L., Madore, B. F., Gibson, B. K., et al. 2001, ApJ, 553, 47

Furlanetto, S. R., Schaye, J., Springel, V., et al. 2005, ApJ, 622, 7

Furusawa, H., Koike, M., Takata, T., et al. 2018, PASJ, 70, S3

Geach, J. E., Smail, I., Chapman, S. C., et al. 2007, ApJ, 655, L9

Geach, J. E., Alexander, D. M., Lehmer, B. D., et al. 2009, ApJ, 700, 1

Gehrels, N. 1986, ApJ, 303, 336

Goerdt, T., Dekel, A., Sternberg, A., et al. 2010, MNRAS, 407, 613

Gronwall, C., Bond, N. A., Ciardullo, R., et al. 2011, ApJ, 743, 9

Guaita, L., Melinder, J., Hayes, M., et al. 2015, A&A, 576, A51

Gunn, J. E., & Gott, J. R. 1972, ApJ, 176, 1

Hagen, A., Ciardullo, R., Gronwall, C., et al. 2014, ApJ, 786, 59

Hagen, A., Zeimann, G. R., Behrens, C., et al. 2016, ApJ, 817, 79

Haiman, Z., Spaans, M., & Quataert, E. 2000, ApJ, 537, L5

Harikane, Y., Ouchi, M., Ono, Y., et al. 2019, arXiv:1902.09555

Hasinger, G., Cappelluti, N., Brunner, H., et al. 2007, ApJS, 172, 29

Hayashino, T., Matsuda, Y., Tamura, H., et al. 2004, AJ, 128, 2073

Hayes, M., Östlin, G., Duval, F., et al. 2014, ApJ, 782, 6

Hogg, D. W. 1999, arXiv e-prints, astro-ph/9905116

Itoh, R., Ouchi, M., Zhang, H., et al. 2018, ApJ, 867, 46

Ivezić, Ž., Kahn, S. M., Tyson, J. A., et al. 2008, arXiv:0805.2366

Iye, M., Ota, K., Kashikawa, N., et al. 2006, Nature, 443, 186

Jurić, M., Kantor, J., Lim, K.-T., et al. 2015, arXiv:1512.07914

Kanekar, N., & Chengalur, J. N. 2003, A&A, 399, 857

Kawanomoto, S., Uraguchi, F., Komiyama, Y., et al. 2018, PASJ, 70, 66

Keel, W. C., Cohen, S. H., Windhorst, R. A., & Waddington, I. 1999, AJ, 118, 2547

Keel, W. C., White, R. E., Chapman, S., et al. 2009, AJ, 138, 986

Kikuta, S., Matsuda, Y., Cen, R., et al. 2019, arXiv:1904.07747

Kobayashi, M. A. R., Murata, K. L., Koekemoer, A. M., et al. 2016, ApJ, 819, 25

Komiyama, Y., Obuchi, Y., Nakaya, H., et al. 2018, PASJ, 70, S2

Konno, A., Ouchi, M., Nakajima, K., et al. 2016, ApJ, 823, 20

Lake, E., Zheng, Z., Cen, R., et al. 2015, ApJ, 806, 46

Leclercq, F., Bacon, R., Wisotzki, L., et al. 2017, A&A, 608, A8

Loeb, A., & Rybicki, G. B. 1999, ApJ, 524, 527

Madau, P., & Dickinson, M. 2014, ARA&A, 52, 415

Magnier, E. A., Schlafly, E., Finkbeiner, D., et al. 2013, The Astrophysical Journal Supplement Series, 205, 20

Malhotra, S., Rhoads, J. E., Finkelstein, S. L., et al. 2012, ApJ, 750, L36

Marchesi, S., Civano, F., Elvis, M., et al. 2016, ApJ, 817, 34

Maseda, M. V., Bacon, R., Franx, M., et al. 2018, ApJ, 865, L1

Mas-Ribas, L., & Dijkstra, M. 2016, ApJ, 822, 84

Mas-Ribas, L., Dijkstra, M., Hennawi, J. F., et al. 2017, ApJ, 841, 19

Matsuda, Y., Yamada, T., Hayashino, T., et al. 2004, AJ, 128, 569

Matsuda, Y., Iono, D., Ohta, K., et al. 2007, ApJ, 667, 667

Matsuda, Y., Nakamura, Y., Morimoto, N., et al. 2009, MNRAS, 400, L66

Matsuda, Y., Yamada, T., Hayashino, T., et al. 2011, MNRAS, 410, L13

Matsuda, Y., Yamada, T., Hayashino, T., et al. 2012, MNRAS, 425, 878

McLinden, E. M., Malhotra, S., Rhoads, J. E., et al. 2013, ApJ, 767, 48

Miralda-Escudé, J. 2003, Science, 300, 1904

Miyazaki, S., Komiyama, Y., Kawanomoto, S., et al. 2018, PASJ, 70, S1

Mo, H., van den Bosch, F. C., & White, S. 2010, Galaxy Formation and Evolution, Cambridge University Press

Momose, R., Ouchi, M., Nakajima, K., et al. 2014, MNRAS, 442, 110

Momose, R., Ouchi, M., Nakajima, K., et al. 2016, MNRAS, 457, 2318

Mori, M., Umemura, M., & Ferrara, A. 2004, ApJ, 613, L97

Nakajima, K., Ouchi, M., Shimasaku, K., et al. 2012, ApJ, 745, 12

Nakajima, K., Schaerer, D., Le Fèvre, O., et al. 2018, A&A, 612, A94

Neufeld, D. A. 1990, ApJ, 350, 216

Oesch, P. A., van Dokkum, P. G., Illingworth, G. D., et al. 2015, ApJ, 804, L30

Oesch, P. A., Brammer, G., van Dokkum, P. G., et al. 2016, ApJ, 819, 129

Ohyama, Y., Taniguchi, Y., Kawabata, K. S., et al. 2003, ApJ, 591, L9

Oke, J. B., & Gunn, J. E. 1983, ApJ, 266, 713

Ono, Y., Ouchi, M., Shimasaku, K., et al. 2010, MNRAS, 402, 1580

Ono, Y., Ouchi, M., Shimasaku, K., et al. 2010, ApJ, 724, 1524

Ono, Y., Ouchi, M., Mobasher, B., et al. 2012, ApJ, 744, 83

Ono, Y., Ouchi, M., Curtis-Lake, E., et al. 2013, ApJ, 777, 155

Ostriker, J. P., & Steinhardt, P. J. 1995, Nature, 377, 600

Orsi, A., Lacey, C. G., & Baugh, C. M. 2012, MNRAS, 425, 87

Ouchi, M., Shimasaku, K., Furusawa, H., et al. 2003, ApJ, 582, 60

Ouchi, M., Shimasaku, K., Akiyama, M., et al. 2008, ApJS, 176, 301

Ouchi, M., Ono, Y., Egami, E., et al. 2009, ApJ, 696, 1164

Ouchi, M., Ellis, R., Ono, Y., et al. 2013, ApJ, 778, 102

Overzier, R. A., Nesvadba, N. P. H., Dijkstra, M., et al. 2013, ApJ, 771, 89

Oyarzún, G. A., Blanc, G. A., González, V., et al. 2017, ApJ, 843, 133

Palunas, P., Teplitz, H. I., Francis, P. J., et al. 2004, ApJ, 602, 545

Partridge, R. B., & Peebles, P. J. E. 1967, ApJ, 147, 868

Paulino-Afonso, A., Sobral, D., Ribeiro, B., et al. 2018, MNRAS, 476, 5479

Peacock, J. A. 1999, Cosmological Physics, Cambridge University Press

Peebles, P. J. E., Schramm, D. N., Turner, E. L., et al. 1991, Nature, 352, 769

Planck Collaboration, Akrami, Y., Arroja, F., et al. 2018, arXiv e-prints, arXiv:1807.06205

Prescott, M. K. M., Kashikawa, N., Dey, A., et al. 2008, ApJ, 678, L77

Prescott, M., Dey, A., Jannuzi, B., et al. 2009, American Astronomical Society Meeting Abstracts #213 213, 334.07

Rauch, M., Haehnelt, M., Bunker, A., et al. 2008, ApJ, 681, 856

Rees, M. J., & Ostriker, J. P. 1977, MNRAS, 179, 541

Rosdahl, J., & Blaizot, J. 2012, MNRAS, 423, 344

Sadoun, R., Romano-Díaz, E., Shlosman, I., et al. 2019, MNRAS, 484, 4601

Saito, T., Shimasaku, K., Okamura, S., et al. 2006, ApJ, 648, 54

Santini, P., Fontana, A., Castellano, M., et al. 2017, ApJ, 847, 76

Salpeter, E. E. 1955, ApJ, 121, 161

Schaerer, D., & de Barros, S. 2009, A&A, 502, 423

Schlafly, E. F., Finkbeiner, D. P., Jurić, M., et al. 2012, ApJ, 756, 158

Scoville, N., Aussel, H., Brusa, M., et al. 2007, ApJS, 172, 1

Shibuya, T., Kashikawa, N., Ota, K., et al. 2012, ApJ, 752, 114

Shibuya, T., Ouchi, M., & Harikane, Y. 2015, ApJS, 219, 15

Shibuya, T., Ouchi, M., Konno, A., et al. 2018, PASJ, 70, S14

Shibuya, T., Ouchi, M., Harikane, Y., et al. 2018, PASJ, 70, S15

Shibuya, T., Ouchi, M., Harikane, Y., & Nakajima, K. 2019, ApJ, 871, 164

Smith, A., Ma, X., Bromm, V., et al. 2019, MNRAS, 484, 39

Sobral, D., Matthee, J., Darvish, B., et al. 2015, ApJ, 808, 139

Sobral, D., Matthee, J., Darvish, B., et al. 2018, MNRAS, 477, 2817

Song, M., Finkelstein, S. L., Ashby, M. L. N., et al. 2016, ApJ, 825, 5

Speagle, J. S., Steinhardt, C. L., Capak, P. L., et al. 2014, ApJS, 214, 15

Springel, V. 2005, MNRAS, 364, 1105

Steidel, C. C., Giavalisco, M., Pettini, M., et al. 1996, ApJ, 462, L17

Steidel, C. C., Adelberger, K. L., Shapley, A. E., et al. 2000, ApJ, 532, 170

Steidel, C. C., Erb, D. K., Shapley, A. E., et al. 2010, ApJ, 717, 289

Steidel, C. C., Bogosavljević, M., Shapley, A. E., et al. 2011, ApJ, 736, 160

Steidel, C. C., Rudie, G. C., Strom, A. L., et al. 2014, ApJ, 795, 165

Sutherland, R. S., & Dopita, M. A. 1993, ApJS, 88, 253

Taniguchi, Y., & Shioya, Y. 2000, ApJ, 532, L13

Taniguchi, Y., Shioya, Y., & Kakazu, Y. 2001, ApJ, 562, L15

Taniguchi, Y., Murayama, T., Scoville, N. Z., et al. 2009, ApJ, 701, 915

Tanvir, N. R., Levan, A. J., Fruchter, A. S., et al. 2012, ApJ, 754, 46

Tegmark, M., Blanton, M. R., Strauss, M. A., et al. 2004, ApJ, 606, 702

Todini, P., & Ferrara, A. 2001, MNRAS, 325, 726

Tonry, J. L., Stubbs, C. W., Lykke, K. R., et al. 2012, ApJ, 750, 99

Topping, M. W., Shapley, A. E., Steidel, C. C., et al. 2018, ApJ, 852, 134

Verhamme, A., Schaerer, D., Atek, H., et al. 2008, A&A, 491, 89

Verhamme, A., Dubois, Y., Blaizot, J., et al. 2012, A&A, 546, A111

Verhamme, A., Orlitová, I., Schaerer, D., et al. 2017, A&A, 597, A13

Watson, D., Christensen, L., Knudsen, K. K., et al. 2015, Nature, 519, 327

Wisotzki, L., Bacon, R., Blaizot, J., et al. 2016, A&A, 587, A98

Wisotzki, L., Bacon, R., Brinchmann, J., et al. 2018, Nature, 562, 229

Wright, E. L. 2006, PASP, 118, 1711

Verhamme, A., Schaerer, D., & Maselli, A. 2006, A&A, 460, 397

Yajima, H., Li, Y., Zhu, Q., et al. 2012, MNRAS, 424, 884

Yajima, H., Nagamine, K., Zhu, Q., Khochfar, S., & Dalla Vecchia, C. 2017, ApJ, 846, 30

Yang, Y., Zabludoff, A., Tremonti, C., et al. 2009, ApJ, 693, 1579

Yang, Y., Zabludoff, A., Eisenstein, D., et al. 2010, ApJ, 719, 1654

Yang, Y., Zabludoff, A., Jahnke, K., et al. 2011, ApJ, 735, 87

Zaroubi, S. 2013, The First Galaxies, 45

Zheng, Z., Cen, R., Weinberg, D., et al. 2011, ApJ, 739, 62

Zitrin, A., Labbé, I., Belli, S., et al. 2015, ApJ, 810, L12